

Award Number:
W81XWH-10-1-0707

TITLE:
Targeted Magnetic Hyperthermia for Lung Cancer

PRINCIPAL INVESTIGATOR:
Jayanth Panyam, Ph.D.

CONTRACTING ORGANIZATION:
University of Minnesota
Minneapolis, MN 55455

REPORT DATE: November 2014

TYPE OF REPORT: Annual Summary

PREPARED FOR: U.S. Army Medical Research and Materiel Command
Fort Detrick, Maryland 21702-5012

DISTRIBUTION STATEMENT: Approved for Public Release;
Distribution Unlimited

The views, opinions and/or findings contained in this report are those of the author(s) and should not be construed as an official Department of the Army position, policy or decision unless so designated by other documentation.

REPORT DOCUMENTATION PAGE				Form Approved OMB No. 0704-0188	
Public reporting burden for this collection of information is estimated to average 1 hour per response, including the time for reviewing instructions, searching existing data sources, gathering and maintaining the data needed, and completing and reviewing this collection of information. Send comments regarding this burden estimate or any other aspect of this collection of information, including suggestions for reducing this burden to Department of Defense, Washington Headquarters Services, Directorate for Information Operations and Reports (0704-0188), 1215 Jefferson Davis Highway, Suite 1204, Arlington, VA 22202-4302. Respondents should be aware that notwithstanding any other provision of law, no person shall be subject to any penalty for failing to comply with a collection of information if it does not display a currently valid OMB control number. PLEASE DO NOT RETURN YOUR FORM TO THE ABOVE ADDRESS.					
1. REPORT DATE November 2014		2. REPORT TYPE Annual Summary		3. DATES COVERED 1Sep2010 - 31Aug2014	
4. TITLE AND SUBTITLE Targeted Magnetic Hyperthermia for Lung Cancer				5a. CONTRACT NUMBER	
				5b. GRANT NUMBER W81XWH-10-1-0707	
				5c. PROGRAM ELEMENT NUMBER	
6. AUTHOR(S) Jayanth Panyam E-Mail: jpanyam@umn.edu				5d. PROJECT NUMBER	
				5e. TASK NUMBER	
				5f. WORK UNIT NUMBER	
7. PERFORMING ORGANIZATION NAME(S) AND ADDRESS(ES) University of Minnesota Minneapolis, MN 55455				8. PERFORMING ORGANIZATION REPORT NUMBER	
9. SPONSORING / MONITORING AGENCY NAME(S) AND ADDRESS(ES) U.S. Army Medical Research and Materiel Command Fort Detrick, Maryland 21702-5012				10. SPONSOR/MONITOR'S ACRONYM(S)	
				11. SPONSOR/MONITOR'S REPORT NUMBER(S)	
12. DISTRIBUTION / AVAILABILITY STATEMENT Approved for Public Release; Distribution Unlimited					
13. SUPPLEMENTARY NOTES					
14. ABSTRACT The hypothesis of this research is that inhalable SPIO nanoparticles surface-functionalized with EGFR targeting ligand, when exposed to an appropriate magnetic field, will enable highly efficient and specific tumor cell death by hyperthermia. In the final year (no-cost extension) of this research program, we have demonstrated that aggregation state of iron oxide nanoparticles significantly affects the therapeutic efficacy. Larger, micron-size aggregates induce necrosis while nano-size aggregates induce apoptosis. Further, micron-size aggregates are more effective in inhibiting tumor growth a mouse tumor model. Overall, our studies show that magnetic hyperthermia using SPIO nanoparticles is a promising strategy to treat lung cancer.					
15. SUBJECT TERMS Lung cancer; Hyperthermia; Targeting					
16. SECURITY CLASSIFICATION OF:			17. LIMITATION OF ABSTRACT	18. NUMBER OF PAGES	19a. NAME OF RESPONSIBLE PERSON
a. REPORT U	b. ABSTRACT U	c. THIS PAGE U			USAMRMC
			UU	61	19b. TELEPHONE NUMBER (include area code)

Table of Contents

	<u>Page</u>
Introduction.....	4
Body.....	4
Key Research Accomplishments.....	12
Reportable Outcomes.....	12
Conclusion.....	13
References.....	14
Appendices.....	18

INTRODUCTION

Despite significant advances in diagnostic techniques and the discovery of new molecularly targeted therapies, lung cancer (specifically, non-small cell lung cancer; NSCLC) is a leading cause of cancer-related deaths in the United States. Poor response rates and survival with current treatments clearly indicate the urgent need to develop an effective means to treat NSCLC. Magnetic hyperthermia is a novel non-invasive approach for ablation of lung tumors, and is based on heat generation by magnetic materials, such as superparamagnetic iron oxide (SPIO) nanoparticles, when subjected to an alternating magnetic field (AMF). However, inadequate delivery of magnetic nanoparticles to tumor cells can result in sub-lethal temperature change and induce resistance. Additionally, non-targeted delivery of these particles to the healthy tissues can result in toxicity. To overcome these problems, we propose to use aerosol-based, tumor-targeted SPIO nanoparticles to induce highly selective tumor cell kill. Tumor cell specificity will be achieved by targeting SPIO nanoparticles to the epidermal growth factor receptor (EGFR), whose overexpression has been observed in as many as 70% of NSCLC patients.

Hypothesis: *Inhalable SPIO nanoparticles surface-functionalized with EGFR targeting ligand, when exposed to an appropriate magnetic field, will enable highly efficient and specific tumor cell death by hyperthermia.*

Specific Aims: The specific aims of this research are: (1) to fabricate aerosol formulation of EGFR-targeted SPIO nanoparticles, (2) to characterize *in vivo* tumor specificity of inhaled EGFR-targeted SPIO nanoparticles, and (3) to determine the *in vivo* anticancer efficacy of inhaled EGFR-targeted SPIO nanoparticles.

BODY

Summary of results

EGFR-targeted SPIO nanoparticles for magnetic hyperthermia in lung cancer

In our studies, we developed EGFR-targeted, inhalable SPIO nanoparticles for magnetic hyperthermia of NSCLC. We examined the effect of EGFR targeting on accumulation and retention of inhaled SPIO nanoparticles in the tumor tissue and the effect of targeted magnetic hyperthermia therapy on tumor growth in an orthotopic lung tumor model.

SPIO nanoparticles were synthesized from iron chlorides by the addition of a strong base, followed by coating with myristic acid to prevent oxidation and then with pluronic to form a stable aqueous dispersion (1). Targeted or scrambled peptide conjugated pluronic, equivalent to 5% surface coverage of the peptide was mixed with pluronic f127 was used to generate EGFR-targeted and control non-targeted nanoparticles.

SPIO nanoparticles were composed of $74 \pm 2\%$ w/w iron oxide, coated with $10 \pm 3\%$ w/w myristic acid, and stabilized by $16 \pm 2\%$ w/w pluronic f127. The hydrodynamic diameter of unconjugated (pluronic COOH terminated) SPIO nanoparticles was 309 ± 24 nm while that of targeted peptide and scrambled peptide conjugated particles were 369 ± 34 nm and 365 ± 45 nm, respectively. The heating rate of SPIO nanoparticles was concentration-dependent, and was similar for both targeted and non-targeted SPIO nanoparticles (Fig 1g; publication #1)

Non-specific uptake of SPIO nanoparticles in A549 cells was determined as a function of time of incubation, concentration of serum in the culture medium and the incubation temperature. From these studies, an incubation time of 30 minutes and low serum concentration were found to be optimal for minimizing the non-specific uptake of SPIO nanoparticles. Using these optimized parameters, an *in vitro* study was performed to determine the effect of EGFR targeting on cellular uptake of SPIO nanoparticles. Nanoparticle uptake into cells was 4.5-fold higher for the EGFR targeted formulation than that for the non-targeted control. Conjugation of scrambled peptide did not result in enhancement of particle uptake into cells, and the presence of excess targeting ligand decreased the cellular uptake of targeted nanoparticles, showing the specific role of EGFR in tumor cell uptake of targeted nanoparticles (Fig 2a; publication #1). Some of the experimental conditions (low serum, initial 4° C, low incubation time) used in this assay are not representative of physiological conditions. However, the goal here was to demonstrate that targeted particles bind to the tumor cells to a higher extent relative to non-targeted particles. The parameters used here facilitated binding of particles to cells while minimizing non-specific uptake.

To determine the effect of EGFR targeting on the effectiveness of magnetic hyperthermia, plated A549 cells were incubated with targeted or non-targeted SPIO nanoparticles, washed and subjected to AMF. Enhanced cellular accumulation of EGFR targeted SPIO nanoparticles could be visualized under the microscope as dark spots on the cells (Fig 2e,f; publication #1). Magnetic hyperthermia with targeted nanoparticles resulted in greater number of cells taking up propidium iodide, indicating enhanced cell death with targeted SPIO nanoparticles (Fig 2b-f; publication #1).

Ultrasonic atomization of SPIO nanoparticle dispersions resulted in aerosols with a mass mean aerodynamic diameter (MMAD) of $1.1 \pm 0.1 \mu\text{m}$ and geometric standard deviation (GSD) of 1.9 ± 0.1 (Supp. Inf. 1; ; publication #1). The iron oxide output rate was determined to be $270 \pm 70 \mu\text{g/min}$. The high iron oxide output and the MMAD size range point to the possibility of a high deposition of these aerosol particles in the mouse lung even with a relatively short exposure time.

Following aerosol exposure, iron oxide concentration in the lungs at 1 hour (Fig 3a; ; publication #1) was similar for targeted and non-targeted SPIO nanoparticles in tumor bearing lungs as well as for blank SPIO particles in healthy lungs, showing that the presence of tumor did not affect the total deposition of particles. It also suggested that targeting does not affect the lung concentration immediately after the administration of particles. However, one week following inhalation, the lung concentration of non-targeted particles decreased while the level of targeted particles was almost constant, demonstrating the effectiveness of EGFR targeting in improving particle retention within tumor-bearing lungs.

Inhalation delivery resulted in a homogenous distribution of SPIO nanoparticles throughout the lung (Fig 3b,c; publication #1). One week after inhalation, a significantly higher amount of Prussian blue staining was observed in the mice that received targeted particles compared to those that received non-targeted particles. In the former, the staining was observed in and around tumor cells (Fig 3d,e; publication #1), with near complete absence of particles from the healthy parts of the lung. In contrast, the latter group did not display much staining in either the tumor or the healthy regions of the lung (not shown).

To study the effect of elevated lung dose of SPIO nanoparticles on the overall body distribution, we used tracheal instillation. Unlike inhalation delivery, which restricts the dose deposited in mouse lungs to $72.5 \pm 14.1 \mu\text{g}$ of magnetite, tracheal instillation allows for a higher dose ($386 \pm 95 \mu\text{g}$ of magnetite) to be delivered.

Following instillation, SPIO particles were mostly observed in the lungs after 1 hour, although some particles were also present in the stomach, due to the mucociliary clearance from the lung. There was no significant difference between the levels of targeted and non-targeted particles in the different organs 1 hour or 1 day after instillation. The concentration of both particles in blood and other organs (except lung) decreased 1 week after instillation compared to 1 hour or 1 day time points (Fig 4a,b; publication #1). On the contrary, while the lung concentration of non-targeted particles decreased over the period of 1 week, the level of targeted particles was fairly constant over 1 week. The final concentration of targeted particles was significantly higher (60%) than non-targeted particles one-week post instillation (Fig 4c; publication #1). In contrast to the high lung concentration, the amount iron in the other tissues was virtually unchanged throughout the duration of the study and was not considerably different from the basal level of iron in the tissues of untreated animals (Fig 4d; publication #1). This data suggested that pulmonary delivery of targeted SPIO nanoparticles can circumvent non-specific distribution into organs such as liver and spleen, which commonly receive the highest dose of intravenously administered therapeutics (2).

While both instillation and inhalation resulted in a significant increase in lung concentration of particles with EGFR targeting, the absolute amount of SPIO particles in the two cases were different. The lung iron content after instillation was 4.5 to 5-fold higher than that after inhalation (400 vs 80 μg for EGFR-targeted SPIO nanoparticles, Fig. 3 and 4; publication #1). This is likely due to the higher dose of particles delivered to the lung through instillation. However, aerosol delivery is a more convenient route of administration in humans than instillation. Additionally, inhalation resulted in a more even distribution of the SPIO nanoparticles throughout the lungs at the time of administration (Fig 3a; publication #1) compared to instillation, where most of the instilled dose resided near the major airways, with almost no particles reaching the periphery (Supp. Inf. 2; publication #1).

Magnetic hyperthermia using non-targeted SPIO particles resulted in an insignificant decrease in lung tumor bioluminescence ($p > 0.05$) relative to that in animals that received the same particles but were not exposed to AMF. Targeted SPIO nanoparticles mediated hyperthermia showed significantly lower lung tumor bioluminescence ($p < 0.05$) (Fig. 5a; publication #1). The lung weights at the end of the study agreed with the bioluminescence data; magnetic hyperthermia with targeted particles resulted in a significantly lower final lung weight compared to the other groups (Fig 5b; publication #1).

These *in vivo* results thus confirm that EGFR targeting enhances the tumor concentration of SPIO nanoparticles, which translated into more effective tumor cell kill. In addition, the treated mice showed no signs of distress over the duration of the study (30 days after magnetic hyperthermia treatment), suggesting that this procedure does not result in acute systemic toxicity or damage to healthy lung tissue. Additionally, the dose of particles that could be delivered to the tumor by inhalation was limited by the small lung volume and the obligate nose-breathing of mice (3). A similar approach can be expected to be more effective in humans, because a higher deposition can be achieved with inhalation through the oral cavity and control

Effect of magnetic hyperthermia on cancer stem cells

A number of recent studies suggest that tumors consist of a minor population of stem-like cells (cancer stem cells; CSCs) that are capable of generating and maintaining a tumor in its entirety (4). These cells have the capacity for asymmetric cell division, generating one identical daughter cell and another that is committed to a distinct differentiation pattern. The latter undergoes a series of divisions and differentiation steps that result in the generation of terminally differentiated cell populations. Cells in the intermediate states are referred to as

progenitors, transit cells or transit amplifying cells (5). All of these phenotypes, collectively termed tumor-initiating cells, have the potential to give rise to a complete tumor. CSCs are resistant to conventional chemotherapy and can initiate tumor recurrence following treatment (6). CSCs possess several defense mechanisms including overexpression of efflux pumps that can eliminate cytotoxic drugs (7), increased expression of DNA-repair proteins that can counteract DNA damage (8), elevated anti-oxidant concentrations to defend against reactive oxygen species (ROS) (9), and low rate of cell division (10). Tumors can become enriched in CSCs after conventional treatments (8, 11), which could account for frequent tumor relapse observed in many cancers. While a number of previous studies (including our results described above) have demonstrated the anticancer efficacy of magnetic hyperthermia (12-15), the effect of magnetic hyperthermia on CSCs has not been reported to date. Using various *in vitro* and *in vivo* assays, we evaluated the ability of SPIO nanoparticle-mediated magnetic hyperthermia to effectively eliminate CSCs.

The side population phenotype, characterized by overexpression of efflux transporters, is believed to be rich in CSCs (16)(17). Hoechst 33342 is a substrate of both P-glycoprotein (P-gp) and Breast Cancer Resistance Protein (BCRP), and the assay is therefore considered a direct correlate of transporter expression. The difference in the fraction of Hoechst 33342-negative cells with and without the dual efflux inhibitor tariquidar is considered the side population. Interestingly, magnetic hyperthermia resulted in a considerable decrease in the side population (~12% in magnetic hyperthermia group vs 20% in the non-hyperthermia SPIO nanoparticle control) (Fig. 2A; publication #2).

Mammospheres are clusters of mammary tumor cells growing in an anchorage-independent fashion and have been shown to be a quantitative indicator of the CSC subpopulation (18). We observed a significant reduction ($P < 0.01$ vs. untreated cells) in mammosphere formation in MDA-MB-231 cells following magnetic hyperthermia (Fig. 2B; publication #2). Untreated cells or cells subjected to conventional hyperthermia formed rigid mammospheres, whereas magnetic hyperthermia treated groups formed smaller spheres (Supp. Fig. 3; publication #2). While 5 min and 15 min of magnetic hyperthermia resulted in 63% and 90% reduction in mammosphere formation respectively, there was a complete absence of mammosphere formation after 30 min of magnetic hyperthermia.

High levels of the enzyme aldehyde dehydrogenase (ALDH) have been reported for normal and cancer precursor cells (19, 20). To determine the effect of magnetic hyperthermia on cells with differential ALDH expression, MDA-MB-231 cells were sorted based on the overall levels of the ALDH enzyme. Clonogenicity studies revealed that both ALDH_{high} and ALDH_{low} cells were equally susceptible to magnetic hyperthermia, with a complete absence of colony formation following magnetic hyperthermia in either population (Fig. 2C; publication #2). Treatment with SPIO nanoparticles also caused a smaller but significant ($p < 0.05$) reduction in clonogenicity of both ALDH_{high} and ALDH_{low} cells.

A characteristic feature of CSCs is their ability to initiate a tumor in xenotransplantation assays (21). *In vivo* tumor initiation study performed in nude mice showed a significant delay in tumor initiation with magnetic hyperthermia-treated cells compared to the corresponding controls. While most control animals developed a tumor within 15 days of cell injection, the first tumor appeared in magnetic hyperthermia-treated groups at 21 days (50,000 cell injection) or 36 days (5000 cell injection) post-injection (Fig. 3A; publication #2). Furthermore, 40% of the animals that received magnetic hyperthermia-treated tumor cells did not develop tumors even at 60 days post cell injection (Fig. 3B; publication #2).

LDH released by cells was used as a quantitative indicator of cell death (22). Magnetic hyperthermia effectively induced cell death in both A549 and MDA-MB-231 cells (Fig. 4A;

publication #2), and the efficacy of cell kill was found to increase with increasing duration of exposure to magnetic hyperthermia. Prolonged (30 min) treatment resulted in 88% and 90% cell death in A549 and MDA-MB-231 cells, respectively. Conventional hyperthermia for 30 min was much less effective in killing cancer cells compared to magnetic hyperthermia.

Induction of apoptosis after magnetic hyperthermia was determined in the cells that survived after a recovery period of 10 hrs after treatment (about 10% in 30 min treatment group). The overall percent of healthy cells decreased with increasing duration of treatment (Table 2; publication #2). The proportion of early apoptotic cells was higher for 5 and 15 min magnetic hyperthermia but was lower for 30 min treatment compared to SPIO nanoparticle-treated cells. However, there was a higher percent of late apoptotic/necrotic cells in the group exposed to 30 min of magnetic hyperthermia. Conventional hyperthermia was much less effective than magnetic hyperthermia in inducing apoptosis (2% early apoptotic cells and 6% late apoptotic cells).

Clonogenicity assay showed that magnetic hyperthermia resulted in a decrease in the proliferative ability and survival of both A549 and MDA-MB-231 cells (Fig 4B; publication #2). Notably, cells subjected to 30 min of magnetic hyperthermia did not form any colonies in either cell line.

Instantaneous 7AAD uptake was used as a measure of acute cell kill during magnetic hyperthermia. As can be seen from Fig 4c (publication #2), magnetic hyperthermia induced instantaneous 7AAD uptake in the treated cells. The 7AAD profile (30%, 47% and 73% after 5 min, 15 min and 30 min of magnetic hyperthermia, respectively) was comparable to the LDH profile (Fig. 4A; publication #2). No significant 7AAD uptake was observed in cells exposed to conventional hyperthermia.

ROS generation increased with increased duration of magnetic hyperthermia (Fig. 5A; publication #2). Conventional hyperthermia did not affect ROS levels compared to untreated cells. Following magnetic hyperthermia, ROS positive population appeared to become necrotic with time, as evidenced by the migration of ROS^{high}/PI^{low} population to ROS^{high}/PI^{high} quadrant (Fig. 5B; publication #2). Addition of N-acetyl cysteine, an antioxidant (23), inhibited ROS generation and decreased the fraction of cells becoming PI positive without affecting the initial population of cells that took up PI instantaneously (Fig. 5C; publication #2). Interestingly, though ROS production and PI uptake by cells that underwent conventional hyperthermia was comparable to that by untreated cells, cells subjected to conventional hyperthermia in the presence of SPIO nanoparticles demonstrated greater ROS production compared to those that received only SPIO nanoparticles (Supp. Fig. 4; publication #2).

CSCs are considered to play important roles in tumor drug resistance and recurrence. Our studies show that CSCs and non-CSCs are equally susceptible to cell death induced by magnetic hyperthermia. Further, magnetic hyperthermia induces both acute necrosis and a slower, ROS-mediated cell-death in treated cells. Some of the cell kill events appear to be temperature-independent, although elevated temperatures appear to amplify those effects. Overall, these results suggest the potential for effective CSC eradication by magnetic hyperthermia.

Effect of particle aggregation on mechanism of tumor cell kill

During the course of our studies, we discovered that particle size plays a key role in determining the extent and mechanism of cell death induced by SPIO nanoparticle-mediated magnetic hyperthermia. Previous studies investigating the effect of particle size have primarily focused on well-dispersed nanoparticles. However, inorganic nanoparticles (such as SPIO

nanoparticles) are prone to aggregation in biological environments. In our studies, we examined the consequence of aggregation on superparamagnetic iron oxide (SPIO) nanoparticle-induced magnetic hyperthermia.

To study the effect of aggregation on therapeutic performance, we used a synthetic technique that facilitated the aggregation of SPIO nanoparticles. The final product was fractionated into micro and nano size aggregates. Nano aggregates had an average hydrodynamic diameter of 207 ± 3 nm. Micro aggregates had an average size of 1052 ± 65 nm. The aggregates were composed of 12 ± 3 nm iron oxide cores (Figure 1a-d; publication #4), which were confirmed to be magnetite (Figure 1e; publication #4). Both nano and micro aggregates had high saturation magnetization of 72.9 and 67.7 emu/g of magnetite, respectively, with negligible remanence (1.64 and 1.44 emu/g of magnetite, respectively) and coercivity (2.73 and 2.36 Oe), verifying their superparamagnetic nature (Figure 1f; publication #4). The heating profiles for the two fractions were virtually identical (Figure 1g; publication #4). The specific loss power for the aggregates was also similar (89.6 ± 2.8 W/g and 93 ± 5.6 W/g for nano and micro aggregates, respectively). As a control, we used a commercial well-dispersed 100-nm SPIO nanoparticle formulation (Nanomag[®]; specific loss power of 68.9 ± 4.3 W/g) in our studies.

Nano aggregate-mediated hyperthermia resulted in a time-dependent decrease in cell survival. Lactate dehydrogenase (LDH) release was not significantly increased at two hours following magnetic hyperthermia treatment (Figure 2a; publication #4); however, less than 10% of the treated cells survived at 24 hours (Figure 2b; publication #4). Similar inefficient early LDH release and higher cell death at 24 hours was also observed in cells subjected to conventional hyperthermia or magnetic hyperthermia using a commercial well-dispersed 100-nm SPIO nanoparticle formulation (Nanomag[®]). This was not surprising, given that hyperthermia has been shown to induce apoptotic cell death, a slow process that takes several hours. Both Nanomag[®]-mediated magnetic hyperthermia and conventional hyperthermia resulted in PARP1 cleavage (Figure 2c; publication #4), confirming the induction of apoptosis with these treatments. However, nano aggregate-induced magnetic hyperthermia resulted in a decrease in the levels of intact 116 kDa PARP1 protein (Figure 2c, Supporting Information Figure S1a; publication #4), without a concomitant increase in levels of the cleaved PARP1 fragment (89 kDa) (Figure 2c, Supporting Information Figure S1b; publication #4), a marker for caspase-dependent apoptosis (24). The lysosomal enzyme cathepsin, which is released after lysosomal rupture such as during autophagy (25), can cleave PARP1 into fragments of different sizes (44, 55, 62 and 74 kDa) (26), and thereby decrease PARP1 levels without a detectable increase in the 89 kDa fragment. Expression of LC3B-II (Figure 2c; publication #4), an autophagy marker (27), further points to autophagy as the primary cell kill mechanism with nano aggregate-mediated magnetic hyperthermia.

Autophagy is a form of programmed cell death mediated by the lysosomal machinery and intracellular membrane rearrangement, leading to massive degradation of cellular components (28). Autophagy involves sequestration of cytoplasmic components in a membrane vesicle called autophagosome, which then fuses with the lysosome to form an autolysosome. Proteases within the autolysosome degrade the sequestered cytoplasmic components. Oxidative stress has been shown to play an important role in inducing autophagy (29, 30). We determined the level of ROS produced by cells subjected to different treatments. The ROS levels remained unchanged after conventional hyperthermia and Nanomag[®]-induced magnetic hyperthermia. However, nano aggregates resulted in elevated cellular ROS levels (Figure 2d). One of the effectors of oxidative stress is GAPDH (31), which causes an elevation of cellular glycolysis and drives autophagy (32). magnetic hyperthermia using SPIO nanoparticle formulations resulted in elevated GAPDH protein levels, and this increase was greatest in cells

subjected to nano aggregate-mediated magnetic hyperthermia (Figure 1c, Supporting Information Figure S1c; publication #4).

With micro aggregates, we observed significant LDH release from treated cells at 2 hours following magnetic hyperthermia treatment (~90% cell kill with 30 min of magnetic hyperthermia, Figure 2a; publication #4). Acute LDH release with micro aggregates indicated that the cell membrane was compromised rather quickly, pointing to a necrotic cell death mechanism (33). To further determine the mechanism of necrosis and to confirm membrane damage, cells incubated with SPIO aggregates were subjected to AMF at a low temperature (<5°C). Acute membrane damage induced by this treatment was determined by monitoring the 'instantaneous' propidium iodide (PI) uptake by treated cells (34). Only the cells treated with micro aggregates demonstrated instantaneous PI uptake in the absence of temperature elevation (Figure 3a; publication #4). Neither nano aggregates (Figure 3b; publication #4) nor Nanomag[®] (Figure 3c; publication #4) was effective in inducing instantaneous PI uptake. We further investigated the effect of size of aggregates on cytotoxicity. Interestingly, these studies suggest that the cytotoxic effect evolves into necrotic mechanism around 400 nm (Figure 3d; publication #4). In addition, we evaluated the behavior of the different formulations under varying magnetic field frequencies. Our results showed that only micro aggregates induced significant instantaneous PI uptake in the presence or absence of bulk temperature elevation at all the frequencies tested (Figure 3e-g; publication #4). Interestingly, the field frequency had a larger effect on micro aggregate-induced acute cell kill in the absence of bulk temperature elevation.

Additionally, while conventional hyperthermia and Nanomag[®] or nano aggregate-induced magnetic hyperthermia caused an elevation of heat shock protein 70 (Hsp70), micro aggregate-mediated magnetic hyperthermia showed no such increase (Supporting Information Figure S1d,e; publication #4). This further verified the role of temperature elevation as the primary mechanism of cell death with sub-micron aggregates and a temperature-independent cell death mechanism with micro aggregates. Induction of Hsp70 expression also suggests the possibility of triggering Hsp70-mediated resistance to thermotherapy (35, 36).

To further study the mechanism of membrane damage induced by micro aggregates, we determined the cellular distribution of the aggregates. Coumarin-6 (a lipophilic green fluorescent dye) was incorporated in SPIO nanoparticles to aid in the visualization of particles (37). Confocal microscopic images showed the presence of aggregates on cell surfaces and in the lysosomes (Figure 4a; publication #4). In the absence of AMF, incubation with micro aggregates did not affect the cell membrane integrity (Figure 4b; publication #4). Exposure to AMF caused blebbing of the membrane at points where the micro aggregates contacted the cell membrane (Figure 4b; publication #4). The membrane blebs were large and characteristic of necrotic blebs (38). Additionally, the blebbed cells also stained positive for PI, indicating the loss of membrane integrity in these cells (Figure 4c; publication #4). Thus, these observations support the concept of cell membrane damage by direct contact of SPIO. Others have suggested that SPIO nanoparticles induce membrane damage as a result of intense local heat generation (39, 40). However, additional studies are needed to investigate the specific mechanism of membrane damage caused by micro aggregates.

To determine whether differences in aggregate size affects *in vivo* therapeutic efficacy as well, we evaluated the anticancer efficacy of micro and nano aggregates in mice bearing subcutaneous A549 tumor xenografts. Mice received either saline or 225 µg magnetite equivalent of nano or micro aggregate suspension by intra-tumoral injection. Animals receiving the aggregates without exposure to AMF served as control groups. Tumor temperatures were monitored using infrared thermometry and the magnetic field conditions were optimized to ensure that the tumor temperature did not increase beyond 46°C. The average tumor

temperature was 43.5°C in both the micro and nano aggregate groups, with the highest temperature reached being 45.5°C and 45.7°C, respectively (Figure 5a; publication #4). Nano aggregate-mediated magnetic hyperthermia resulted in a moderate decrease in tumor growth rate ($p = 0.085$) relative to that in animals that received nano aggregates but were not exposed to AMF. Micro aggregate-mediated magnetic hyperthermia showed significant effectiveness ($p < 0.001$), with near complete inhibition of tumor growth (Figure 5b; publication #4). The results from the bioluminescence imaging reinforced this finding, with micro aggregate-mediated magnetic hyperthermia being highly effective in decreasing the tumor-associated luminescence (Figure 5c; publication #4). Histological analysis of the tumor sections revealed that micro aggregate-mediated magnetic hyperthermia resulted in the formation of “hollow” tumors, with a large central acellular core and a small outer rim of cells (Figure 6a, Supporting Information Figure S2; publication #4). Immediately after exposure to AMF, cells surrounding the SPIO aggregates (confirmed by Prussian blue staining) were characterized by altered morphology, decreased cell volume, and increased nuclear density (Figure 6c,e; publication #4). Tumor tissue sections from the control group (injected with micro aggregates but not exposed to AMF) showed no such changes in the cellular morphology around the SPIO aggregates (Figure 6b,d; publication #4). Because all the experimental parameters (dose of SPIO, duration of AMF exposure and the temperature elevation) were similar for both nano and micro aggregates, the enhanced effectiveness of micro aggregates is likely due to local membrane damage.

It was interesting to note that despite their inhomogeneous distribution within the tumor, a complete inhibition of tumor growth was observed for micro aggregate treatment. A number of studies show that treatments that induce acute necrosis in the tumors are able to stimulate anti-tumor immune response, which reinforces the anticancer effectiveness of the treatment (41, 42). Thus, the acute cell damage and necrosis induced by micro aggregates could stimulate a bystander anti-tumor immune response, which would affect the growth of the entire tumor. The animal model used here (SCID mice) precludes the generation of humoral and T-cell mediated immune responses. However, these mice have functional natural killer (NK) cells that can mount an effective anticancer immune response (43). In addition, increase in local tumor temperature (hyperthermia) would likely reinforce the anticancer benefits of acute necrosis induced by micro aggregates. While an extensive investigation into generation of anticancer immune response by micro aggregates is beyond the scope of this report, these *in vivo* results confirm that larger aggregates are more effective in killing tumor cells than smaller sub-micron size aggregates. Intravenous delivery of micro aggregates is likely not practical due to concerns of embolism (44, 45) and because the particle size is too large to take advantage of the enhanced permeation and retention effect (46). However, the particle size range of micro aggregates is particularly suitable for inhalation delivery (47, 48) to treat lung tumors (48-50). Also, a number of solid tumors (liver, kidney, prostate, lung) are treated clinically by local interventions using physical ablation techniques (microwave, radiofrequency) (51-53). Such cancers will benefit from treatment with the micro aggregates. Alternately, an *in situ* aggregation approach can also be envisioned, where sub-micron size particles injected intravenously aggregate into micron size aggregates in the tumor microenvironment.

Inorganic nanoparticles have the propensity to aggregate when introduced into a biological milieu. Our studies showed that the particle size of aggregates affects the therapeutic performance of SPIO nanoparticles. Well-dispersed SPIO nanoparticles induce apoptosis, similar to that observed with conventional hyperthermia. Nanometer size aggregates, on the other hand, induce temperature-dependent autophagy through generation of ROS. Micron size aggregates caused rapid membrane damage and acute cell kill. This novel mechanism of cell kill induced by micro aggregates translated into effective *in vivo* tumor growth inhibition. Overall this work highlights the potential for developing highly effective anticancer therapeutics through simple yet often overlooked modifications of delivery systems such as their state of aggregation.

KEY RESEARCH ACCOMPLISHMENTS (OVERALL)

- Developed and optimized an inhalable formulation of targeted SPIO nanoparticles that are suitable for magnetic hyperthermia.
- Demonstrated that SPIO nanoparticles functionalized with EGFR targeting ligand is taken up to a greater extent than non-functionalized nanoparticles by lung tumor cells that overexpress EGFR.
- Demonstrated that magnetic hyperthermia using the formulated SPIO NANOPARTICLES is highly effective in killing A549 cells.
- Demonstrated the effectiveness of EGFR targeting in enhancing the lung tumor concentration of SPIO particles in a mouse model.
- Started examining the toxicity and efficacy of targeted SPIO particle-mediated hyperthermia in a lung tumor model.
- Demonstrated effective inhibition of *in vivo* tumor growth by SPIO particle-mediated magnetic hyperthermia.
- Demonstrated the effectiveness of EGFR targeting in enhancing the therapeutic effectiveness of magnetic hyperthermia in a mouse model.
- Demonstrated the effect of particle size on mechanism and extent of tumor cell death.
- Demonstrated a novel approach to improve the effectiveness of magnetic hyperthermia.
- Demonstrated that magnetic hyperthermia can effectively eliminate cancer stem cells thus potentially reducing chances of tumor recurrence.

REPORTABLE OUTCOMES (OVERALL)

Presentations

- Magnetic hyperthermia using iron oxide nanoparticles – Pharmaceuticals Department Seminar 2010, University of Minnesota, MN (Oral presentation)
- Targeted magnetic hyperthermia for lung cancer – IPrime 2010, Minneapolis, MN (Oral presentation)
- Magnetic hyperthermia for lung cancer – Nano Drug Delivery Symposium 2010, Omaha, NE (Poster presentation)
- Magnetic hyperthermia for lung cancer – Minnesota Nanotechnology Conference 2010, Minneapolis, MN (Poster presentation)
- Magnetic hyperthermia for lung cancer – Globalization of Pharmaceuticals Education Network 2010, Chapel Hill, NC (Poster presentation)
- Are cancer-initiating cells susceptible to magnetic hyperthermia? – Pharmaceuticals Department Seminar 2011, University of Minnesota, MN (Oral presentation)
- Magnetic hyperthermia for lung cancer – Rho Chi Research Symposium 2011, Minneapolis, MN (Poster presentation)
- Magnetic hyperthermia as an effective approach to kill cancer stem cells – Masonic Cancer Center Research Symposium 2011, Minneapolis, MN (Poster presentation)
- Are cancer stem cells susceptible to magnetic hyperthermia? – IPrime 2011, Minneapolis, MN (Oral presentation)

- Magnetic hyperthermia as an effective approach to kill cancer stem cells – Pharmaceutics Graduate Student Research Meeting 2011, Madison, WI (Oral presentation)
- Magnetic hyperthermia for lung cancer
 - Rho Chi Research Symposium 2011, Minneapolis, MN (poster)
 - Pharmaceutics Department Seminar 2012, Minneapolis, MN (oral)
- Magnetic hyperthermia as an effective approach to kill cancer stem cells
 - AAPS 2011, Washington, DC (poster)
 - 7th Annual Minnesota Nanotechnology Workshop 2011, Minneapolis, MN (poster)
 - Rho Chi Research Symposium 2012, Minneapolis, MN (poster)
- Acute necrosis and reactive oxygen species generation by magnetic hyperthermia leads to effective elimination of cancer stem cells - 9th International Conference on the Scientific and Clinical Applications of Magnetic Carriers 2012, Minneapolis, MN (poster)
- Iron oxide particle size determines the anticancer effectiveness of magnetic hyperthermia - IPRIME 2012, Minneapolis, MN (oral)
- Targeted magnetic hyperthermia for lung cancer – Design of Medical Devices Conference 2013, Minneapolis, MN (Invited talk)
- Inhalable magnetic nanoparticles for targeted hyperthermia in lung cancer therapy – AAPS 2014, San Antonio, TX (Poster presentation)

Publications

1. Sadhukha T, Wiedmann TS, Panyam J. “Inhalable magnetic nanoparticles for targeted hyperthermia in lung cancer therapy.” *Biomaterials* 2013; 34(21):5163-71.
2. Sadhukha T, Niu L, Wiedmann TS, Panyam J. “Effective elimination of cancer stem cells by magnetic hyperthermia.” *Mol Pharm.* 2013; 10 (4):1432–41.
3. Wiedmann TS, Sadhukha T, Hammer BE, Panyam J. “Image-guided drug delivery in lung cancer.” *Drug Delivery and Translational Research.* 2012; 2(1):31-44.
4. Sadhukha T, Wiedmann TS, Panyam J. Enhancing therapeutic efficacy through designed aggregation of nanoparticles, *Biomaterials.* 2014 Sep;35(27):7860-9

CONCLUSION

Our studies highlight the potential of SPIO nanoparticle-induced magnetic hyperthermia for the treatment of lung cancer. Targeting the particles to EGFR enables improved retention of particles in lung tumors and enhanced efficacy. Similarly, micron-sized aggregates allow for greater tumor inhibition compared to nano-sized aggregates.

REFERENCES

1. Jain, T.K., Morales, M.A., Sahoo, S.K., Leslie-Pelecky, D.L., and Labhasetwar, V. 2005. Iron oxide nanoparticles for sustained delivery of anticancer agents. *Mol Pharm* 2:194-205.
2. Taratula, O., Garbuzenko, O.B., Chen, A.M., and Minko, T. 2011. Innovative strategy for treatment of lung cancer: targeted nanotechnology-based inhalation co-delivery of anticancer drugs and siRNA. *J Drug Target* 19:900-914.
3. Drazen, J.M., Finn, P.W., and De Sanctis, G.T. 1999. Mouse models of airway responsiveness: physiological basis of observed outcomes and analysis of selected examples using these outcome indicators. *Annu Rev Physiol* 61:593-625.
4. Chandler, J.M., and Lagasse, E. 2010. Cancerous stem cells: deviant stem cells with cancer-causing misbehavior. *Stem Cell Res Ther* 1:13.
5. Potten, C.S., and Loeffler, M. 1990. Stem cells: attributes, cycles, spirals, pitfalls and uncertainties. Lessons for and from the crypt. *Development* 110:1001-1020.
6. Li, X., Lewis, M.T., Huang, J., Gutierrez, C., Osborne, C.K., Wu, M.F., Hilsenbeck, S.G., Pavlick, A., Zhang, X., Chamness, G.C., et al. 2008. Intrinsic resistance of tumorigenic breast cancer cells to chemotherapy. *J Natl Cancer Inst* 100:672-679.
7. Moitra, K., Lou, H., and Dean, M. 2011. Multidrug efflux pumps and cancer stem cells: insights into multidrug resistance and therapeutic development. *Clin Pharmacol Ther* 89:491-502.
8. Bao, S., Wu, Q., McLendon, R.E., Hao, Y., Shi, Q., Hjelmeland, A.B., Dewhirst, M.W., Bigner, D.D., and Rich, J.N. 2006. Glioma stem cells promote radioresistance by preferential activation of the DNA damage response. *Nature* 444:756-760.
9. Diehn, M., Cho, R.W., Lobo, N.A., Kalisky, T., Dorie, M.J., Kulp, A.N., Qian, D., Lam, J.S., Ailles, L.E., Wong, M., et al. 2009. Association of reactive oxygen species levels and radioresistance in cancer stem cells. *Nature* 458:780-783.
10. Moore, N., and Lyle, S. 2011. Quiescent, slow-cycling stem cell populations in cancer: a review of the evidence and discussion of significance. *J Oncol* 2011.
11. Dylla, S.J., Beviglia, L., Park, I.K., Chartier, C., Raval, J., Ngan, L., Pickell, K., Aguilar, J., Lazetic, S., Smith-Berdan, S., et al. 2008. Colorectal cancer stem cells are enriched in xenogeneic tumors following chemotherapy. *PLoS One* 3:e2428.
12. Johannsen, M., Thiesen, B., Jordan, A., Taymoorian, K., Gneveckow, U., Waldofner, N., Scholz, R., Koch, M., Lein, M., Jung, K., et al. 2005. Magnetic fluid hyperthermia (MFH) reduces prostate cancer growth in the orthotopic Dunning R3327 rat model. *Prostate* 64:283-292.
13. Jones, S.K., Winter, J.G., and Gray, B.N. 2002. Treatment of experimental rabbit liver tumours by selectively targeted hyperthermia. *Int J Hyperthermia* 18:117-128.
14. Jordan, A., Scholz, R., Maier-Hauff, K., van Landeghem, F.K., Waldoefner, N., Teichgraeber, U., Pinkernelle, J., Bruhn, H., Neumann, F., Thiesen, B., et al. 2006. The effect of thermotherapy using magnetic nanoparticles on rat malignant glioma. *J Neurooncol* 78:7-14.
15. Balivada, S., Rachakatla, R.S., Wang, H., Samarakoon, T.N., Dani, R.K., Pyle, M., Kroh, F.O., Walker, B., Leaym, X., Koper, O.B., et al. 2010. A/C magnetic hyperthermia of melanoma mediated by iron(0)/iron oxide core/shell magnetic nanoparticles: a mouse study. *BMC Cancer* 10:119.
16. Ho, M.M., Ng, A.V., Lam, S., and Hung, J.Y. 2007. Side population in human lung cancer cell lines and tumors is enriched with stem-like cancer cells. *Cancer Res* 67:4827-4833.
17. Sung, J.-M., Cho, H.-J., Yi, H., Lee, C.-H., Kim, H.-S., Kim, D.-K., Abd El-Aty, A.M., Kim, J.-S., Landowski, C.P., Hediger, M.A., et al. 2008. Characterization of a stem cell population in lung cancer A549 cells. *Biochemical and Biophysical Research Communications* 371:163-167.

18. Iliopoulos, D., Hirsch, H.A., Wang, G., and Struhl, K. 2011. Inducible formation of breast cancer stem cells and their dynamic equilibrium with non-stem cancer cells via IL6 secretion. *Proc Natl Acad Sci U S A* 108:1397-1402.
19. Ginestier, C., Hur, M.H., Charafe-Jauffret, E., Monville, F., Dutcher, J., Brown, M., Jacquemier, J., Viens, P., Kleer, C.G., Liu, S., et al. 2007. ALDH1 is a marker of normal and malignant human mammary stem cells and a predictor of poor clinical outcome. *Cell stem cell* 1:555-567.
20. Croker, A.K., Goodale, D., Chu, J., Postenka, C., Hedley, B.D., Hess, D.A., and Allan, A.L. 2009. High aldehyde dehydrogenase and expression of cancer stem cell markers selects for breast cancer cells with enhanced malignant and metastatic ability. *J Cell Mol Med* 13:2236-2252.
21. Burke, A.R., Singh, R.N., Carroll, D.L., Wood, J.C.S., D'Agostino Jr, R.B., Ajayan, P.M., Torti, F.M., and Torti, S.V. 2012. The resistance of breast cancer stem cells to conventional hyperthermia and their sensitivity to nanoparticle-mediated photothermal therapy. *Biomaterials* 33:2961-2970.
22. Korzeniewski, C., and Callewaert, D.M. 1983. An enzyme-release assay for natural cytotoxicity. *J Immunol Methods* 64:313-320.
23. Spagnuolo, G., D'Anto, V., Cosentino, C., Schmalz, G., Schweikl, H., and Rengo, S. 2006. Effect of N-acetyl-L-cysteine on ROS production and cell death caused by HEMA in human primary gingival fibroblasts. *Biomaterials* 27:1803-1809.
24. Lazebnik, Y.A., Kaufmann, S.H., Desnoyers, S., Poirier, G.G., and Earnshaw, W.C. 1994. Cleavage of poly(ADP-ribose) polymerase by a proteinase with properties like ICE. *Nature* 371:346-347.
25. Uchiyama, Y. 2001. Autophagic cell death and its execution by lysosomal cathepsins. *Arch Histol Cytol* 64:233-246.
26. Chaitanya, G.V., Steven, A.J., and Babu, P.P. 2010. PARP-1 cleavage fragments: signatures of cell-death proteases in neurodegeneration. *Cell Commun Signal* 8:31.
27. Kabeya, Y., Mizushima, N., Ueno, T., Yamamoto, A., Kirisako, T., Noda, T., Kominami, E., Ohsumi, Y., and Yoshimori, T. 2000. LC3, a mammalian homologue of yeast Apg8p, is localized in autophagosome membranes after processing. *EMBO J* 19:5720-5728.
28. Tsujimoto, Y., and Shimizu, S. 2005. Another way to die: autophagic programmed cell death. *Cell Death Differ* 12 Suppl 2:1528-1534.
29. Zhang, H., Kong, X., Kang, J., Su, J., Li, Y., Zhong, J., and Sun, L. 2009. Oxidative stress induces parallel autophagy and mitochondria dysfunction in human glioma U251 cells. *Toxicol Sci* 110:376-388.
30. Chen, Y., McMillan-Ward, E., Kong, J., Israels, S.J., and Gibson, S.B. 2008. Oxidative stress induces autophagic cell death independent of apoptosis in transformed and cancer cells. *Cell Death Differ* 15:171-182.
31. Cerella, C., D'Alessio, M., Cristofanon, S., De Nicola, M., Radogna, F., Dicato, M., Diederich, M., and Ghibelli, L. 2009. Subapoptogenic oxidative stress strongly increases the activity of the glycolytic key enzyme glyceraldehyde 3-phosphate dehydrogenase. *Ann N Y Acad Sci* 1171:583-590.
32. Colell, A., Ricci, J.E., Tait, S., Milasta, S., Maurer, U., Bouchier-Hayes, L., Fitzgerald, P., Guio-Carrion, A., Waterhouse, N.J., Li, C.W., et al. 2007. GAPDH and autophagy preserve survival after apoptotic cytochrome c release in the absence of caspase activation. *Cell* 129:983-997.
33. Proskuryakov, S.Y., Konoplyannikov, A.G., and Gabai, V.L. 2003. Necrosis: a specific form of programmed cell death? *Exp Cell Res* 283:1-16.
34. Liu, D., Wang, L., Wang, Z., and Cuschieri, A. 2012. Magnetoporation and Magnetolysis of Cancer Cells via Carbon Nanotubes Induced by Rotating Magnetic Fields. *Nano Lett* 12:5117-5121.

35. Frossard, J.L. 1999. Heat shock protein 70 (HSP70) prolongs survival in rats exposed to hyperthermia. *Eur J Clin Invest* 29:561-562.
36. Ito, A., Shinkai, M., Honda, H., Yoshikawa, K., Saga, S., Wakabayashi, T., Yoshida, J., and Kobayashi, T. 2003. Heat shock protein 70 expression induces antitumor immunity during intracellular hyperthermia using magnetite nanoparticles. *Cancer Immunol Immunother* 52:80-88.
37. Patil, Y., Sadhukha, T., Ma, L., and Panyam, J. 2009. Nanoparticle-mediated simultaneous and targeted delivery of paclitaxel and tariquidar overcomes tumor drug resistance. *J Control Release* 136:21-29.
38. Barros, L.F., Kanaseki, T., Sabirov, R., Morishima, S., Castro, J., Bittner, C.X., Maeno, E., Ando-Akatsuka, Y., and Okada, Y. 2003. Apoptotic and necrotic blebs in epithelial cells display similar neck diameters but different kinase dependency. *Cell Death Differ* 10:687-697.
39. Huang, H., Delikanli, S., Zeng, H., Ferkey, D.M., and Pralle, A. 2010. Remote control of ion channels and neurons through magnetic-field heating of nanoparticles. *Nat Nanotechnol* 5:602-606.
40. Polo-Corrales, L., and Rinaldi, C. 2012. Monitoring iron oxide nanoparticle surface temperature in an alternating magnetic field using thermoresponsive fluorescent polymers. *Journal of Applied Physics* 111:07B334-333.
41. Gravante, G., Sconocchia, G., Ong, S.L., Dennison, A.R., and Lloyd, D.M. 2009. Immunoregulatory effects of liver ablation therapies for the treatment of primary and metastatic liver malignancies. *Liver International* 29:18-24.
42. Mroz, P., Hashmi, J.T., Huang, Y.-Y., Lange, N., and Hamblin, M.R. 2010. Stimulation of anti-tumor immunity by photodynamic therapy. *Expert Review of Clinical Immunology* 7:75-91.
43. Takehara, T., Uemura, A., Tatsumi, T., Suzuki, T., Kimura, R., Shiotani, A., Ohkawa, K., Kanto, T., Hiramatsu, N., and Hayashi, N. 2007. Natural killer cell-mediated ablation of metastatic liver tumors by hydrodynamic injection of IFN α gene to mice. *International Journal of Cancer* 120:1252-1260.
44. Carrstensen, H., Muller, R.H., and Muller, B.W. 1992. Particle size, surface hydrophobicity and interaction with serum of parenteral fat emulsions and model drug carriers as parameters related to RES uptake. *Clin Nutr* 11:289-297.
45. Mansour, H.M., Rhee, Y.S., and Wu, X. 2009. Nanomedicine in pulmonary delivery. *Int J Nanomedicine* 4:299-319.
46. Singh, S., Sharma, A., and Robertson, G.P. 2012. Realizing the clinical potential of cancer nanotechnology by minimizing toxicologic and targeted delivery concerns. *Cancer Res* 72:5663-5668.
47. Patton, J.S., and Byron, P.R. 2007. Inhaling medicines: delivering drugs to the body through the lungs. *Nat Rev Drug Discov* 6:67-74.
48. Lennon, F.E., Mirzapoiazova, T., Mambetsariev, B., Salgia, R., Moss, J., and Singleton, P.A. 2012. Overexpression of the mu-opioid receptor in human non-small cell lung cancer promotes Akt and mTOR activation, tumor growth, and metastasis. *Anesthesiology* 116:857-867.
49. Zarogoulidis, P., Chatzaki, E., Porpodis, K., Domvri, K., Hohenforst-Schmidt, W., Goldberg, E.P., Karamanos, N., and Zarogoulidis, K. 2012. Inhaled chemotherapy in lung cancer: future concept of nanomedicine. *Int J Nanomedicine* 7:1551-1572.
50. Yi, D., and Wiedmann, T.S. 2010. Inhalation adjuvant therapy for lung cancer. *J Aerosol Med Pulm Drug Deliv* 23:181-187.
51. Bomers, J.G.R., Sedelaar, J.P.M., Barentsz, J.O., and Fütterer, J.J. 2012. MRI-Guided Interventions for the Treatment of Prostate Cancer. *American Journal of Roentgenology* 199:714-720.

52. Cornelis, F., Balageas, P., Le Bras, Y., Rigou, G., Boutault, J.R., Bouzgarrou, M., and Grenier, N. 2012. Radiologically-guided thermal ablation of renal tumours. *Diagnostic and Interventional Imaging* 93:246-261.
53. Sharma, A., Abtin, F., and Shepard, J.-A.O. 2012. Image-Guided Ablative Therapies for Lung Cancer. *Radiologic Clinics of North America* 50:975-999.

APPENDICES

Copies of publications #1-4 are included as a part of the appendix.

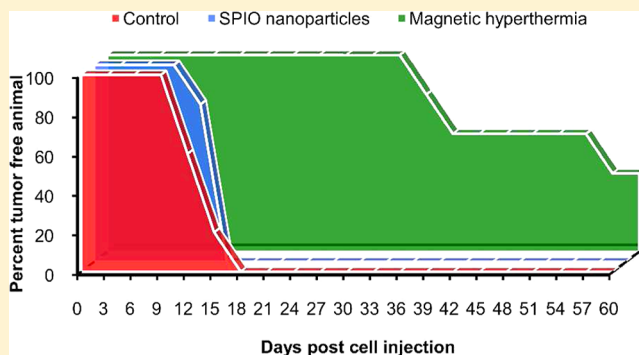
Effective Elimination of Cancer Stem Cells by Magnetic Hyperthermia

Tanmoy Sadhukha,[†] Lin Niu,[†] Timothy Scott Wiedmann,[†] and Jayanth Panyam^{*,†,‡}[†]Department of Pharmaceutics, College of Pharmacy, University of Minnesota, Minneapolis, Minnesota 55455, United States[‡]Masonic Cancer Center, University of Minnesota, Minneapolis, Minnesota 55455, United States

S Supporting Information

ABSTRACT: Cancer stem cells (CSCs) are a subpopulation of cancer cells that have stem cell-like properties and are thought to be responsible for tumor drug resistance and relapse. Therapies that can effectively eliminate CSCs will, therefore, likely inhibit tumor recurrence. The objective of our study was to determine the susceptibility of CSCs to magnetic hyperthermia, a treatment that utilizes superparamagnetic iron oxide nanoparticles placed in an alternating magnetic field to generate localized heat and achieve selective tumor cell kill. SPIO NPs having a magnetite core of 12 nm were used to induce magnetic hyperthermia in A549 and MDA-MB-231 tumor cells. Multiple assays for CSCs, including side population phenotype, aldehyde dehydrogenase expression, mammosphere formation, and *in vivo* xenotransplantation, indicated that magnetic hyperthermia reduced or, in some cases, eliminated the CSC subpopulation in treated cells. Interestingly, conventional hyperthermia, induced by subjecting cells to elevated temperature (46 °C) in a water bath, was not effective in eliminating CSCs. Our studies show that magnetic hyperthermia has pleiotropic effects, inducing acute necrosis in some cells while stimulating reactive oxygen species generation and slower cell kill in others. These results suggest the potential for lower rates of tumor recurrence after magnetic hyperthermia compared to conventional cancer therapies.

KEYWORDS: superparamagnetic iron oxide, magnetic hyperthermia, cancer stem cells, necrosis, reactive oxygen species, mammosphere, clonogenicity, tumorigenicity, aldehyde dehydrogenase



■ INTRODUCTION

A number of recent studies suggest that tumors consist of a minor population of stem-like cells (cancer stem cells; CSCs) that are capable of generating and maintaining a tumor in its entirety.¹ These cells have the capacity for asymmetric cell division, generating one identical daughter cell and another that is committed to a distinct differentiation pattern. The latter undergoes a series of divisions and differentiation steps that result in the generation of terminally differentiated cell populations. Cells in the intermediate states are referred to as progenitors, transit cells, or transit amplifying cells.² All of these phenotypes, collectively termed tumor-initiating cells, have the potential to give rise to a complete tumor. CSCs are resistant to conventional chemotherapy and can initiate tumor recurrence following treatment.³ CSCs possess several defense mechanisms including overexpression of efflux pumps that can eliminate cytotoxic drugs,⁴ increased expression of DNA-repair proteins that can counteract DNA damage,⁵ elevated antioxidant concentrations to defend against reactive oxygen species (ROS),⁶ and low rate of cell division.⁷ Tumors can become enriched in CSCs after conventional treatments,^{5,8} which could account for frequent tumor relapse observed in many cancers.

Hyperthermia, which utilizes elevated temperatures in the range of 41–46 °C to kill tumor cells,⁹ has been shown to

improve treatment response and survival when used in combination with radiotherapy, surgery, and/or chemotherapy.^{10,11} In mouse tumor models, the addition of local hyperthermia significantly increased the sensitivity of CSCs to radiotherapy.¹² Magnetic hyperthermia is a related approach that utilizes superparamagnetic iron oxide nanoparticles (SPIO NPs) placed in an alternating magnetic field to generate heat for a highly localized tumor cell kill.¹³ Magnetic hyperthermia is currently in clinical trials in Europe for glioblastoma as well as prostate and pancreatic cancers.¹⁴ While a number of previous studies have demonstrated the anticancer efficacy of magnetic hyperthermia,¹⁵ the effect of magnetic hyperthermia on CSCs has not been reported to date. Using various *in vitro* and *in vivo* assays, we evaluated the ability of SPIO NP-mediated magnetic hyperthermia to effectively eliminate CSCs.

■ EXPERIMENTAL SECTION

Materials. Ferrous chloride tetrahydrate, ferric chloride hexahydrate, myristic acid, Pluronic F127, ascorbic acid,

Received: January 9, 2013

Revised: February 11, 2013

Accepted: February 22, 2013

Published: February 22, 2013

potassium hydroxide, 1,10-phenanthroline, and sodium acetate were purchased from Sigma (St. Louis, MO). Penicillin/streptomycin, fetal bovine serum (FBS), RPMI 1640, Dulbecco's phosphate-buffered saline (DPBS), F-12K (Kaighn's modification), MEM, nonessential amino acids, sodium pyruvate, and trypsin-ethylenediaminetetraacetic acid (EDTA) solution were obtained from Invitrogen Corporation (Carlsbad, CA). Cytotox 96 nonradioactive cytotoxicity assay kit was purchased from Promega (Madison, WI).

Methods. Synthesis of Water-Dispersible SPIO NPs. A stable aqueous dispersion of SPIO NPs was prepared from iron chlorides as previously described.¹⁶ In brief, 0.82 g of ferric chloride hexahydrate and 0.33 g of ferrous chloride tetrahydrate were dissolved in 30 mL of degassed and nitrogen-purged water, and 3 mL of 5 M ammonium hydroxide was added dropwise to this solution and stirred for 30 min. Iron oxide nanoparticles formed were washed three times with nitrogen-purged water (each wash followed by magnetic separation of nanoparticles), sonicated in a water bath sonicator for 2 min, and heated to 80 °C. About 100 mg of myristic acid was added to the heated mixture and stirred for another 30 min. Particles were washed twice with acetone to remove excess myristic acid, followed by two additional washes with water to remove excess acetone. Myristic acid-coated particles were then suspended in 30 mL of water; 100 mg of pluronic F127 was added, and the mixture was stirred overnight. The final dispersion was lyophilized (Labconco, FreeZone 4.5, Kansas City, MO) to obtain SPIO NPs. Every step of the synthesis was carefully conducted to minimize exposure to atmospheric oxygen.

Characterization of SPIO NPs. Dynamic light scattering was used to determine the hydrodynamic diameter of SPIO NPs. About 0.5 mg/mL of SPIO NPs dispersed deionized water was subjected to particle size analysis using a Delsa Nano C Particle Analyzer (Beckman, Brea, CA). Transmission electron microscopy (TEM) of SPIO NPs was performed using a JEOL JEM-1210 transmission electron microscope (Peabody, MA). A drop of an aqueous dispersion of SPIO NPs was placed on a Lacey carbon-coated copper grid (300 mesh, Ted Pella Inc. Redding, CA) and allowed to air-dry before imaging. Diameters of 100 different particles were measured from different TEM images using ImageJ software. The average diameter along the horizontal axis was determined as the mean Feret's diameter. The mean crystallite size of SPIO NPs was calculated from their X-ray diffraction pattern. SPIO NPs were subjected to a Cu-K α radiation (45 kV, 40 mA) in a wide-angle powder X-ray diffractometer (D5005, Siemens, Madison, WI). The instrument was operated in the step-scan mode in increments of 0.05° 2 θ over an angular range of 10–100° 2 θ with a dwell time of 1 s for each scan step. Data analysis was performed using OriginPro 8 software (OriginLab Corporation, Northampton, MA). Five highest peaks (at 30.1°, 35.5°, 43.1°, 57.1°, and 62.7° 2 θ) were fit using the pseudo-Voigt profile function, which is a linear combination of the Gaussian and Lorentzian components of the diffraction peaks. The Scherrer equation was utilized to determine the mean particle size of SPIO NPs.¹⁷

Fourier-transformed infrared spectroscopy (FT-IR) of SPIO NPs was performed using Vertex 70 FT-IR spectrophotometer (Bruker Optics Inc., Billerica, MA). About 5 mg of SPIO NPs were added to the FT-IR stage and scanned from 4000 cm⁻¹ to 400 cm⁻¹. Each spectrum was obtained as an average of 16 interferograms at a resolution of 2 cm⁻¹ and analyzed using OPUS software (Bruker Optics Inc., Billerica, MA). Magnetic properties were determined using a vibrating sample magneto-

meter (Micromod model 3900, Princeton, NJ) operating at room temperature. Accurately weighed samples of SPIO NPs was sprinkled on a lightly greased silicon wafer and their magnetization curves were recorded in magnetic fields ranging from -1 to 1 T, at increments of 0.002 T. The saturation magnetization per gram of magnetite was calculated from the magnetization curves normalized to the weight of magnetite added. The composition of SPIO NPs was estimated using 1,10-phenanthroline-based iron assay.¹⁸ About 5 mg of SPIO NPs was dissolved in 12 N hydrochloric acid and then diluted with distilled water to obtain a final acid concentration of 0.2 N. Samples of 10 mg/mL ascorbic acid, 22.4 mg/mL potassium hydroxide, 123 mg/mL sodium acetate, and 1.2 mg/mL 1,10-phenanthroline were added to the SPIO NP solution in a volume ratio of 1:1:5:1:1. The absorbance at 490 nm was recorded using a microplate reader (ELx800 Absorbance Microplate Reader, Biotek, Winooski, VT), and the iron content was analyzed using ferric chloride (hexahydrate) solutions in 0.2 N hydrochloric acid as a standard.

Magnetic Heating Rate. SPIO NPs were dispersed in 1 mL of Hank's F-12K medium or in 1 mL of molten 3% agarose, which was then allowed to form a gel in 10 mm × 75 mm disposable borosilicate glass cell culture tubes. Magnetic heating was performed using an induction heating system (1 kW Hotshot, Ameritherm Inc., Scottsville, NY) by placing the suspension at the center of a multiturn copper coil that generated the alternating magnetic field (nominal magnetic field strength of 6 kA/m and frequency of 386 kHz). The temperature change was measured using a fluoroptic probe (Lumasense Technologies, Santa Clara, CA). Samples were thermally equilibrated to 37 °C before exposure to the field.

Cell Culture Studies. A549 (human lung adenocarcinoma) and MDA-MB-231 (human mammary adenocarcinoma) cells were used in the study. A549 cells were propagated using F-12K medium supplemented with 10% fetal bovine serum (FBS) and 1% antibiotic solution. MDA-MB-231 cells were grown in MEM supplemented with 10% FBS, 1% nonessential amino acids, 1% sodium pyruvate, and 1% antibiotic solution. Both cell lines were maintained at 37 °C and in 5% carbon dioxide.

Effect of Magnetic Hyperthermia on CSCs. a. Side Population Determination. Following magnetic hyperthermia, A549 cells were centrifuged and resuspended in prewarmed 1 mL of Dulbecco's modified Eagle's medium (DMEM) with 2% FBS and 10 mM 4-(2-hydroxyethyl)-1-piperazineethanesulfonic acid (HEPES). Hoechst 33342 dye was added at a concentration of 5 μ g/mL. In each treatment group, one sample was pretreated with 2 μ M tariquidar, an inhibitor of Hoechst efflux. Cells were then incubated at 37 °C for 90 min with occasional shaking. Cells were then washed with chilled Hank's balanced salt solution (HBSS) with 2% FBS and 10 mM HEPES buffer and resuspended in chilled buffer. 7-Aminoactinomycin-D (7AAD) was added to the sample tubes before flow cytometric analysis to gate for live cells. Flow analysis was carried out on a FACSDiva (BD Biosciences); Hoechst 33342 dye was excited at 357 nm, and the fluorescence was measured at 402–446 nm (blue) and 650–670 nm (red) wavelengths.^{19,20}

b. Mammosphere Assay. Following magnetic hyperthermia, MDA-MB-231 cells were washed and resuspended in cell culture medium. About 3000 live cells (counted by trypan blue exclusion) were plated in ultralow adhesion 6-well plates with 2 mL of mammosphere formulation (DMEM/F-12 medium supplemented with 10 ng/mL human-fibroblast growth factor, 20 ng/mL recombinant human epidermal growth factor, 0.4%

bovine serum albumin, 5 $\mu\text{g/mL}$ insulin, and 1% antibiotics). The number of mammospheres formed was counted under a light microscope 5 days after treatment.²¹

c. Aldehyde Dehydrogenase Assay. Thirty million MDA-MB-231 cells were sorted based on their levels of aldehyde dehydrogenase (ALDH) enzyme using the ALDEFLUOR kit (STEMCELL Technologies Inc., Vancouver, Canada).²² Prior to sorting, 5 μL of the activated reagent was added to each milliliter of the cell suspension (1 million cells/mL), mixed well, and 500 μL of the suspension was immediately transferred to another tube containing 5 μL of diethylaminobenzaldehyde (DEAB) reagent in 95% ethanol. The tubes were incubated for 45 min at 37 °C, following which the cells were centrifuged in cold, and redispersed in cold ALDEFLUOR assay buffer and stored on ice. Cells were then sorted using BD FACS Vantage (BD Biosciences) cell sorter. Cells incubated with DEAB reagent were used to gate for cells having low ALDH level (ALDH_{low}), and cells to the right of the gate were sorted as ALDH_{high} population. Around 3–4% of MDA-MB-231 cells were ALDH_{high}. ALDH-sorted cells were subjected to 30 min of magnetic hyperthermia. Cells incubated with or without SPIO NP and not exposed to alternating magnetic field were used as controls. Treated cells were evaluated for clonogenicity as described above.

d. Tumorigenicity Assay. The study was carried out in compliance with protocol approved by the Institutional Animal Care and Use Committee at the University of Minnesota. Female BALB/c-nude mice (C.Cg/AnNTac-Foxn1^{nu} NE9; Taconic Farms), four to six weeks of age, were used for the studies. Mice received either 5000 or 50 000 live A549 cells (viability determined through trypan blue exclusion) that were previously subjected to 30 min of magnetic hyperthermia. Animals that received similar number of untreated cells or cells treated with SPIO NPs but not exposed to alternating magnetic field served as controls. Animals were observed once every three days for the appearance of palpable tumors.¹⁹ Tumor dimensions were also measured using a digital calipers, and the tumor volume (V) was calculated using the formula $V = 0.5(L \times W^2)$, where L and W are the longest and shortest diameters, respectively. The development of 100 mm³ tumors or 60 days after cell injection (whichever came first) marked the end of the study for each animal.

Cytotoxicity Studies. **a. Cell Death after Magnetic Hyperthermia.** About 1 million cells were suspended in 500 μL of RPMI (without phenol red and with 5% FBS). 500 μL of 5 mg/mL SPIO NP dispersion in the same medium was added to the cell suspension placed in an alternating magnetic field (6 kA/m, 386 kHz) for 5, 15, or 30 min. The cell suspension temperature was carefully maintained between 43 and 46 °C (Supporting Information, Figure 1). Cells with or without SPIO NPs and not exposed to alternating magnetic field were used as controls. In addition, cells incubated in a water bath at 46 °C for 30 min, with or without SPIO NPs, served as conventional hyperthermia controls. Following treatment (after 2 h), the cells were pelleted down, and the amount of lactate dehydrogenase (LDH) released by the cells in the supernatant was analyzed. LDH released by the untreated control was used to normalize for the background cell death, and LDH released by equal number of freeze–thaw lysed cells was used to calculate 100% cell death.

To evaluate the induction of apoptosis by magnetic hyperthermia, treated cells were gently dispersed in medium containing 10% FBS and plated in 6-well plates. After another 10 h, A549 cells were examined for apoptosis/necrosis by a flow-

cytometry-based annexin-V fluorescein isothiocyanate (FITC)/propidium iodide (PI) assay. Briefly, cells were trypsinized and then centrifuged at 1000 rpm for 8 min. The cell pellets were stained with FITC-conjugated annexin-V and PI according to manufacturer's instructions (BD Pharmingen, San Jose, CA) and then immediately analyzed using a flow cytometer (BD FACSCalibur, BD Biosciences, San Jose, CA). FITC and PI fluorescence emissions were detected in FL-1 (515–545 nm) and FL-3 (670 long-pass) modes, respectively. Data from at least 10 000 cells were analyzed using Cyflogic software (Cyflo Ltd., Turku, Finland).

b. Clonogenicity. Clonogenicity was used as a measure of the proliferative potential of cells subjected to magnetic hyperthermia.²³ Following treatment, 200 live cells (identified by trypan blue exclusion assay) from each group were plated in a 10 cm culture dish and allowed to form colonies. After 2 weeks (about 12–15 cell doubling times^{24,25}), the plates were washed with DPBS and fixed with 5% formalin in DPBS for 3 min. Colonies were further washed with DPBS and then stained with 0.05% crystal violet for 30 min. Plates were then washed gently with water and air-dried, and the number of colonies formed in each treatment groups was counted. Colonies were counted prior to and after washing and staining steps to account for the loss of colonies during the processing steps.

c. Instantaneous Cell Death during Magnetic Hyperthermia. Following incubation of A549 cells with SPIO NPs, 2 mM 7AAD, a cell viability stain, was added to the cells prior to exposing them to magnetic field. Cells not exposed to alternating magnetic field, with or without SPIO NPs, and cells exposed to 30 min of conventional hyperthermia were used as controls. Following treatments, cells were immediately washed by centrifugation, resuspended in RPMI (without phenol red) and subjected to flow cytometry. 7AAD fluorescence was detected in the FL-3 channel. Data from 20 000 cells in each group were analyzed using Cyflogic software.

Reactive Oxygen Species (ROS) Generation after Magnetic Hyperthermia. Immediately prior to magnetic hyperthermia treatment, 5-(and-6)-chloromethyl-2',7'-dichlorodihydrofluorescein diacetate, acetyl ester (CM-H₂DCFDA) (7.5 μM) and PI (10 μM) were added to A549 cell suspension. Cells were subjected to magnetic hyperthermia and then to flow cytometric analysis. The deacetylated and oxidized product, 2',7'-dichlorofluorescein, formed due to ROS generation in the cells, was detected in the FL-1 channel while PI fluorescence was detected in the FL-3 channel.

To determine the role of ROS in inducing cell death, cells were pretreated with 10 mM *N*-acetyl cysteine for 1 h before adding CM-H₂DCFDA and then subjected to 5 min of magnetic hyperthermia. Cells treated with 5 mM hydrogen peroxide with and without *N*-acetyl cysteine pretreatment served as additional controls.

Statistical Analysis. Statistical analyses were performed using one-way analysis of variance (ANOVA) by the Bonferroni-Holm method for comparison between individual groups. A probability level of $P < 0.05$ was considered significant.

■ RESULTS

Characterization of SPIO NPs. The physicochemical properties of SPIO NPs used in this study are summarized in Table 1. The particles were composed of $74 \pm 2\%$ (w/w) iron oxide, coated with $10 \pm 3\%$ (w/w) myristic acid, and stabilized by $16 \pm 2\%$ (w/w) Pluronic F127. TEM studies indicated that the mean Feret's diameter of the iron oxide core was 12 ± 3 nm

Table 1. SPIO NP Characterization

Composition	
form of iron oxide	magnetite
iron oxide content	74 ± 1.6%
myristic acid coating	10 ± 2.7%
Pluronic F127 coating	16 ± 1.6%
Particle Size	
particle size (TEM)	12 ± 3 nm
crystallite size (XRD)	12 ± 1 nm
hydrodynamic diameter (DLS)	185 nm
polydispersity	0.22
Magnetic Parameters	
saturation magnetization	60.5 emu/g magnetite
remanence	1.6 emu/g magnetite
coercivity	1.37 Oersted

(Figure 1A). This result was confirmed by the mean particle size calculated from XRD data (12 ± 1 nm) (Supporting Figure 2). SPIO NPs had an average hydrodynamic diameter of 185 nm, suggesting that particles in aqueous media existed as small aggregates rather than as individual SPIO NPs. FTIR spectroscopy showed the presence of characteristic magnetite bands at 570 cm^{-1} and 400 cm^{-1} and the absence of maghemite bands at 700 cm^{-1} and $630\text{--}660\text{ cm}^{-1}$, indicating that the primary form of iron oxide in SPIO NPs was magnetite (data not shown).²⁶ SPIO NPs had a high saturation magnetization of 60.5 emu/g of magnetite, with negligible remanence and coercivity, verifying their superparamagnetic nature (Figure 1B). The heating rate of SPIO NPs was concentration-dependent and was similar in both cell culture medium and in agarose gel (Figure 1C,D). Based on the heating rates, a concentration of 2.5 mg/mL of SPIO NPs (equivalent to 1.85 mg/mL of magnetite) was found to be optimal for inducing magnetic hyperthermia *in vitro*.

Effect of Magnetic Hyperthermia on CSCs. a. Side Population in A549 Cells. The side population phenotype, characterized by overexpression of efflux transporters, is believed to be rich in CSCs.^{19,20} Hoechst 33342 is a substrate of both P-glycoprotein (P-gp) and Breast Cancer Resistance Protein (BCRP), and the assay is therefore considered a direct correlate of transporter expression. The difference in the fraction of Hoechst 33342-negative cells with and without the dual efflux inhibitor tariquidar is considered the side population. Interestingly, magnetic hyperthermia resulted in a considerable decrease in the side population ($\sim 12\%$ in magnetic hyperthermia group vs 20% in the nonhyperthermia SPIO NP control) (Figure 2A).

b. Mammosphere Assay. Mammospheres are clusters of mammary tumor cells growing in an anchorage-independent fashion and have been shown to be a quantitative indicator of the CSC subpopulation.²⁷ We observed a significant reduction ($P < 0.01$ vs untreated cells) in mammosphere formation in MDA-MB-231 cells following magnetic hyperthermia (Figure 2B). Untreated cells or cells subjected to conventional hyperthermia formed rigid mammospheres, whereas magnetic hyperthermia treated groups formed smaller spheres (Supporting Figure 3). While 5 and 15 min of magnetic hyperthermia resulted in 63% and 90% reduction in mammosphere formation, respectively, there was a complete absence of mammosphere formation after 30 min of magnetic hyperthermia.

c. ALDH Assay. High levels of ALDH have been reported for normal and cancer precursor cells.^{22,25} To determine the effect of magnetic hyperthermia on cells with differential ALDH expression, MDA-MB-231 cells were sorted based on the overall levels of the ALDH enzyme. Clonogenicity studies revealed that both ALDH_{high} and ALDH_{low} cells were equally susceptible to magnetic hyperthermia, with a complete absence of colony formation following magnetic hyperthermia in either population

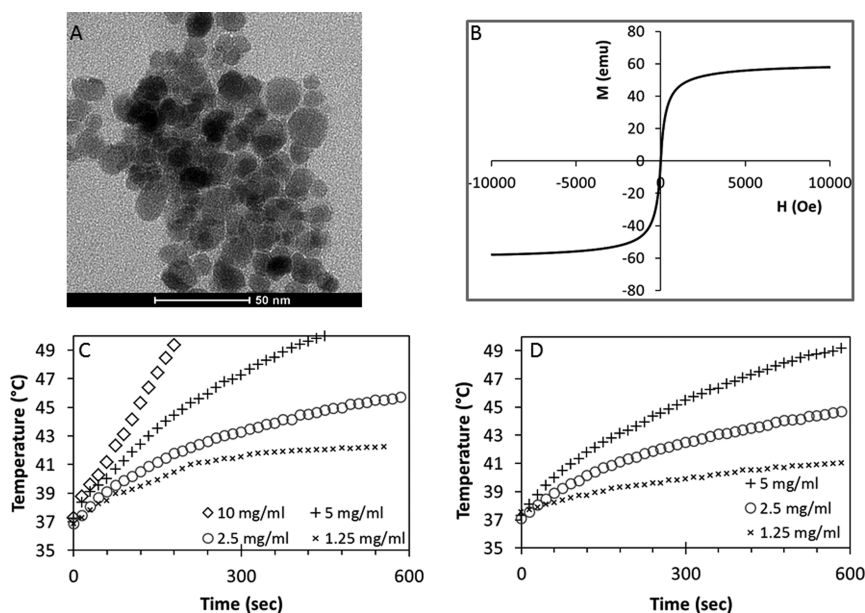


Figure 1. Characterization of SPIO NPs. (A) Representative TEM image of SPIO NPs. A drop of aqueous NP suspension was placed on a TEM grid and air-dried before observing under an electron microscope. Scale bar, 50 nm. (B) Magnetization. Magnetization curves were recorded on a vibrating sample magnetometer. The curve was normalized to the weight of magnetite added to obtain saturation magnetization per gram of magnetite. The sigmoidal curve is characteristic of superparamagnetic substances. Heating rates of SPIO NPs dispersed in (C) cell culture medium and (D) agarose gel. SPIO NP dispersions in a borosilicate glass tube were placed in an alternating magnetic field of 6 kA/m and operating at a frequency of 386 kHz. The initial temperature was equilibrated to 37°C , and the temperature of SPIO NP dispersion was sampled at 15 s intervals using a fluoroptic probe following the application of the alternating magnetic field.

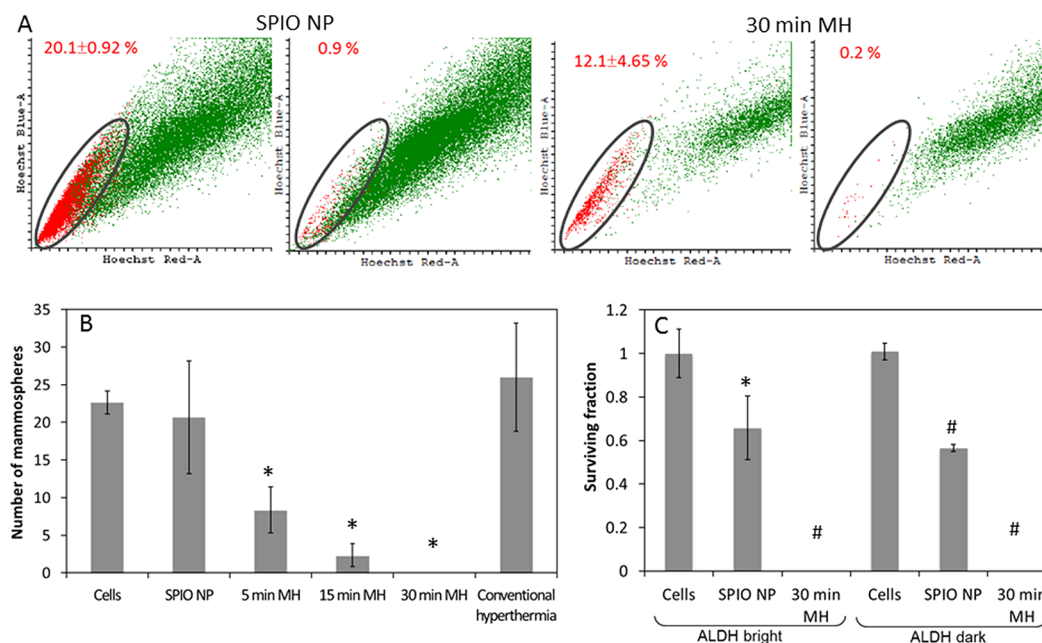


Figure 2. Effect of magnetic hyperthermia on CSCs. (A) Side population assay. Following magnetic hyperthermia, A549 cells were incubated with Hoechst 33342 dye at 37 °C for 90 min followed by flow cytometric analysis of Hoechst 33342 fluorescence in blue and red channels. Cells pretreated with tariquidar (a dual P-gp and BCRP efflux inhibitor) were used as controls. The flow images shown are representative Hoechst profiles of cells treated with SPIO NPs with (right) and without (left) heating. Side population is shown circumscribed within the oval area. The average percent (\pm S.D.) of side population is shown for each group, $n = 3$. (B) Mammosphere formation. After magnetic hyperthermia, 3000 live cells (counted by trypan blue exclusion) were plated in ultralow adhesion 6-well plates with mammosphere medium and left undisturbed at 37 °C. The number of mammospheres formed was counted using a light microscope on day 5 after treatment. Data shown is mean \pm S.D., $n = 3$. * $P < 0.01$ vs untreated cells. (C) Clonogenicity of ALDH_{high} and ALDH_{low} MDA-MB-231 cells. MDA-MB-231 cells were sorted based on ALDH enzyme levels and then subjected to 30 min of magnetic hyperthermia. Post-treatment, 200 live cells were plated for clonogenicity assessment. The graph shows the relative survival fraction compared to untreated cells. Data shown is mean \pm S.D., $n = 3$. * $P < 0.05$; # $P < 0.001$ vs untreated cells.

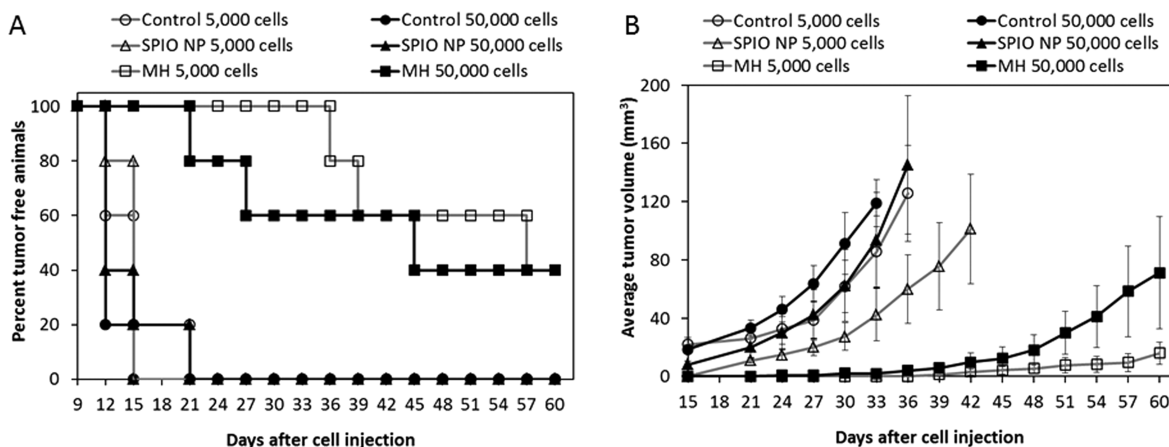


Figure 3. *In vivo* tumorigenicity of magnetic hyperthermia treated cells. A549 cells subjected to magnetic hyperthermia were injected subcutaneously into BALB-nude mice at a cell density of 5000 or 50 000 live cells per animal. Untreated cells or cells incubated with SPIO NPs but not exposed to alternating magnetic field were used as controls. A tumor size of 100 mm³ or 60 days post cell injection (whichever came first) marked the end of the study. (A) Percent tumor-free animals and (B) average tumor volumes plotted as a function of days after cell injection. Data shown is mean \pm S.D., $n = 5$.

(Figure 2C). Treatment with SPIO NP also caused a smaller but significant ($p < 0.05$) reduction in clonogenicity of both ALDH_{high} and ALDH_{low} cells.

d. Tumorigenicity Assay. A characteristic feature of CSCs is their ability to initiate a tumor in xenotransplantation assays.²⁸ *In vivo* tumor initiation study performed in nude mice showed a significant delay in tumor initiation with magnetic hyperthermia-treated cells compared to the corresponding controls. While most control animals developed a tumor within 15 days of cell injection, the first tumor appeared in magnetic hyperthermia-

treated groups at 21 days (50 000 cell injection) or 36 days (5000 cell injection) postinjection (Figure 3A). Furthermore, 40% of the animals that received magnetic hyperthermia-treated tumor cells did not develop tumors even at 60 days post cell injection (Figure 3B).

Cell Kill after Magnetic Hyperthermia. LDH released by cells was used as a quantitative indicator of cell death.²⁹ Magnetic hyperthermia effectively induced cell death in both A549 and MDA-MB-231 cells (Figure 4A), and the efficacy of cell kill was found to increase with increasing duration of exposure to

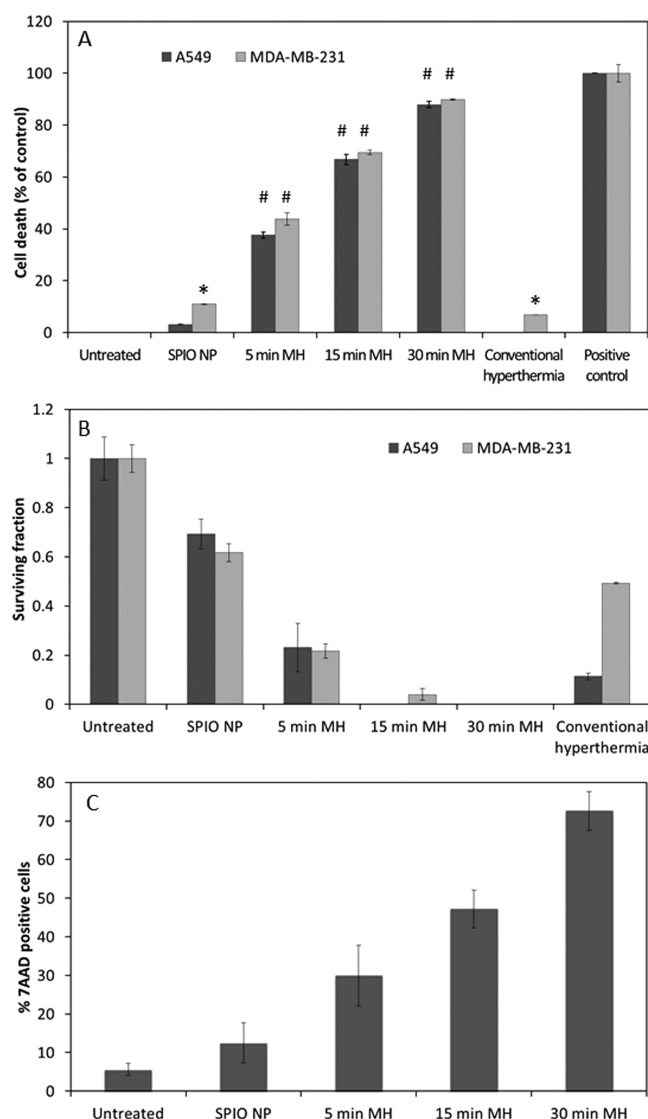


Figure 4. Effect of magnetic hyperthermia on A549 tumor cell kill. (A) LDH release. Cells were subjected to magnetic hyperthermia for 5, 15, or 30 min, following which the supernatant medium was assayed for the amount of LDH released after 2 h of treatment. SPIO NP-treated cells (without exposure to AMF) and cells subjected to 30 min of conventional hyperthermia at 46 °C were used as controls. Equal numbers of freeze–thaw lysed cells were used to determine LDH release from 100% cell death while untreated cells were used to determine background LDH release. Data shown is mean \pm S.D., $n = 3$. * $P < 0.05$; # $P < 0.01$ vs untreated cells. (B) Clonogenicity. About 200 live cells from each treatment group were plated in a 10 cm tissue culture plate and observed for colony formation. The number of colonies formed was counted 2 weeks later. Data shown is mean \pm S.D., $n = 3$. All treatments resulted in statistical significant ($P < 0.01$) decrease in surviving fraction. (C) Instantaneous 7AAD uptake. 7AAD was added to each treatment tube immediately prior to magnetic hyperthermia. After treatment, the cells were washed to eliminate excess 7AAD and subjected to flow cytometric analysis. Data shown is mean \pm S.D., $n = 3$. All hyperthermia treatments resulted in statistical significant ($P < 0.01$) increase in 7AAD uptake.

magnetic hyperthermia. Prolonged (30 min) treatment resulted in 88% and 90% cell death in A549 and MDA-MB-231 cells, respectively. Conventional hyperthermia for 30 min was much less effective in killing cancer cells compared to magnetic hyperthermia.

Induction of apoptosis after magnetic hyperthermia was determined in the cells that survived after a recovery period of 10 h after treatment (about 10% in 30 min treatment group). The overall percent of healthy cells decreased with increasing duration of treatment (Table 2). The proportion of early

Table 2. Induction of Apoptosis and Necrosis in A549 Cells Determined by Annexin-V/PI Assay

	(PI–/A–) (healthy)	(PI–/A+) (early apoptotic)	(PI+/A+) (late apoptotic)	(PI+/A–) (necrotic)
untreated cells	97	1	1	0.4
SPIO NP	97	0.6	2	0.7
5 min magnetic hyperthermia	92	2	6	0.4
15 min magnetic hyperthermia	81	3	14	2
30 min magnetic hyperthermia	62	2	33	3
conventional hyperthermia	93	2	6	0.2

apoptotic cells was higher for 5 and 15 min magnetic hyperthermia but was lower for 30 min treatment compared to SPIO NP-treated cells. However, there was a higher percent of late apoptotic/necrotic cells in the group exposed to 30 min of magnetic hyperthermia. Conventional hyperthermia was much less effective than magnetic hyperthermia in inducing apoptosis (2% early apoptotic cells and 6% late apoptotic cells).

A clonogenicity assay showed that magnetic hyperthermia resulted in a decrease in the proliferative ability and survival of both A549 and MDA-MB-231 cells (Figure 4B). Notably, cells subjected to 30 min of magnetic hyperthermia did not form any colonies in either cell line.

Instantaneous 7AAD uptake was used as a measure of acute cell kill during magnetic hyperthermia. As can be seen from Figure 4c, magnetic hyperthermia induced instantaneous 7AAD uptake in the treated cells. The 7AAD profile (30%, 47%, and 73% after 5 min, 15 min, and 30 min of magnetic hyperthermia, respectively) was comparable to the LDH profile (Figure 4A). No significant 7AAD uptake was observed in cells exposed to conventional hyperthermia.

ROS Generation during Magnetic Hyperthermia. ROS generation increased with increased duration of magnetic hyperthermia (Figure 5A). Conventional hyperthermia did not affect ROS levels compared to untreated cells. Following magnetic hyperthermia, ROS positive population appeared to become necrotic with time, as evidenced by the migration of ROS^{high}/PI^{low} population to the ROS^{high}/PI^{high} quadrant (Figure 5B). The addition of N-acetyl cysteine, an antioxidant,³⁰ inhibited ROS generation (not shown) and decreased the fraction of cells becoming PI positive without affecting the initial population of cells that took up PI instantaneously (Figure 5C). Interestingly, though ROS production and PI uptake by cells that underwent conventional hyperthermia was comparable to that by untreated cells, cells subjected to conventional hyperthermia in the presence of SPIO NPs demonstrated greater ROS production compared to those that received only SPIO NPs (Supporting Figure 4).

DISCUSSION

Magnetic hyperthermia, a technique involving the use of SPIO NPs subjected to AMF to generate heat,¹³ has been studied for treating tumors as early as 1957.³¹ The main advantage of

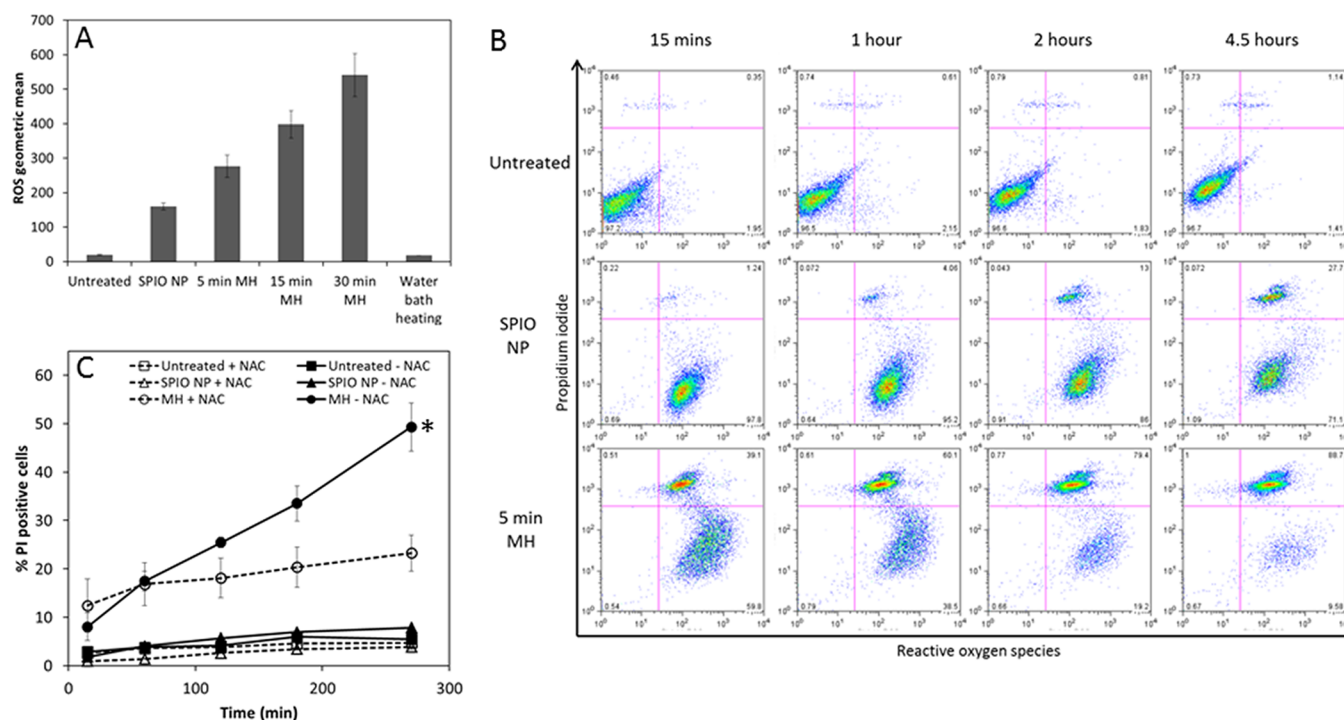


Figure 5. Effect of magnetic hyperthermia on ROS generation. (A) ROS generation immediately after treatment. CM-H₂DCFDA was added to A549 cells immediately before exposure to alternating magnetic field, followed by flow cytometric analysis to determine ROS levels. The graph shows the effect of treatments on geometric mean intensity of fluorescence, an indicator of ROS levels in the cells. Data shown is mean \pm S.D., $n = 3$. All treatments resulted in statistical significant ($P < 0.01$) increase in the geometric mean intensity of ROS fluorescence. (B) Kinetic study to monitor ROS levels and PI uptake by cells subjected to magnetic hyperthermia. Cells were first treated with CM-H₂DCFDA and PI and then subjected to 5 min of magnetic hyperthermia. Fluorescence from ROS generation and PI uptake by the cells were monitored by flow cytometry. The change in the flow profile of untreated (top), cells treated with SPIO NPs (middle), and cells treated with magnetic hyperthermia (bottom) are shown at different times after treatment. (C) Effect of ROS scavenging on PI uptake by magnetic hyperthermia treated cells. Prior to SPIO NP or CM-H₂DCFDA addition and exposure to alternating magnetic field, cells were pretreated with *N*-acetyl cysteine (NAC) to scavenge free radicals. The percent of PI positive cells at different time point are plotted for the treatment groups. Data shown is mean \pm S.D., $n = 3$. * $P < 0.001$ vs all other groups.

magnetic hyperthermia is that the heating rate can be well-controlled by adjusting particle size and shape of SPIO NPs as well as by modulating the properties of the alternating magnetic field.³² There are several magnetic materials that can be used for inducing magnetic hyperthermia. However, most studies have focused on magnetic iron oxides, Fe₃O₄ (magnetite)³³ and γ -Fe₂O₃ (maghemite),³⁴ which have been proved to be well tolerated in clinical studies.³⁵ The core size of SPIO NPs dictates the primary mechanism of heat generation—Brownian relaxation and/or Néel relaxation.^{36,37} The predominant mechanism of heat generation by 12 nm SPIO NPs used in our studies is through Néel relaxation, a mechanism of heat generation unaffected by suspending medium viscosity or by particle aggregation. This was confirmed from the similar heating rates observed for SPIO NPs in liquid and gel media. This data suggests that heat production by these particles will not likely be affected by the presence of dense extracellular matrix found in solid tumors.³⁸ Additionally, higher saturation magnetization of magnetic substances is more desirable, because this translates to higher heating rate per unit mass. SPIO NPs used in our studies were composed of magnetite, which possesses higher saturation magnetization than maghemite.³⁹ Optimum size and properties of synthesized SPIO NPs, along with their high saturation magnetization and iron content, allowed for effective induction of magnetic hyperthermia in our studies.

A number of preclinical studies have demonstrated the potential use of magnetic hyperthermia as an effective anticancer treatment modality.¹³ In addition, magnetic hyperthermia is in

clinical trials for different cancers.^{14,40} However, there are no reports on the effect of magnetic hyperthermia on CSCs, a subpopulation that is thought to be responsible for tumor drug resistance and relapse.⁴¹ Since no single assay is confirmatory with regard to the effect of treatments on CSCs, we evaluated the effect of magnetic hyperthermia on multiple biomarkers and functional properties of CSCs. Hoechst 33342 efflux¹⁹ and ALDH⁴² assays are functional assays identifying CSC-rich population, while mammosphere formation and tumorigenicity assays are based on the growth and proliferative properties unique to CSCs.⁴³ All of these assays indicated that magnetic hyperthermia reduced or, in some cases, eliminated the CSC subpopulation in treated cells.

Magnetic hyperthermia was effective in reducing CSC population in both long-term assays such as mammosphere formation as well as in short-term studies such as side population assay. The short-term effects of magnetic hyperthermia could be attributed to the induction of acute cell death, which was evident from high LDH release immediately after the treatment. The increased number of 7AAD positive cells immediately after treatment further points to the possibility of acute necrosis induced by magnetic hyperthermia. Lack of significant acute cell kill with conventional hyperthermia suggests that necrosis brought about by magnetic hyperthermia was likely temperature-independent. CSCs have been shown to be resistant to induction of apoptosis,⁴⁴ a slow programmed process of cell death. Necrosis is a more violent and acute cell death, most often mediated by mechanical damage to cell membrane and/or other

vital cellular organelles.⁴⁵ If magnetic hyperthermia indeed caused necrosis, it is unlikely that CSCs will have resistance mechanisms to tolerate this acute cell death pathway.²⁸

Exposure of cells to 30 min of magnetic hyperthermia resulted in the induction of apoptosis/necrosis in only about 35% of cells 12 h after treatment, suggesting that a majority of the cells are viable and healthy. However, these cells did not form any colonies in the clonogenicity assay. This implies that in addition to acute necrosis, there is a pronounced long-term effect of magnetic hyperthermia on CSCs. A mechanism postulated for the resistance of CSCs against DNA damage is decreased basal levels of ROS generation in CSCs.⁶ Since SPIO NPs have been reported to induce ROS,⁴⁶ we investigated ROS generation as a possible mechanism of cell kill with magnetic hyperthermia. Immediately after magnetic hyperthermia, ROS levels were higher than in controls, and this appeared to be followed by a slow increase in the number of dying cells. Inhibition of ROS generation using an antioxidant suppressed this transition. These results suggest that magnetic hyperthermia induces ROS generation, which results in additional cell death after some latency. A similar increase in ROS production and cell death was observed in cells incubated with SPIO NPs and subjected to conventional hyperthermia but not in those subjected to either conventional hyperthermia alone or SPIO NP treatment alone. Overall, our studies suggest that ROS generation by magnetic hyperthermia is mediated by the presence of SPIO NPs and is amplified by higher temperatures. One possibility is that SPIO NPs generate ROS, which would normally be scavenged efficiently by CSCs;⁴⁷ however, generation of heat could decrease the ability of CSCs to scavenge ROS and thereby increases their susceptibility to ROS.

In our studies, all of the magnetic hyperthermia treatments were performed on suspended tumor cells. The size of the induction coil used prevented studies on plated cells. It is possible that suspended and adherent cells (either grown in two-dimensional plates or as three-dimensional spheres) may have different susceptibilities to magnetic hyperthermia. The effect of growth and plating conditions on the effect of magnetic hyperthermia on CSCs will be examined in our future studies.

■ CONCLUSIONS

CSCs are considered to play important roles in tumor drug resistance and recurrence. Our studies show that CSCs and non-CSCs are equally susceptible to cell death induced by magnetic hyperthermia. Further, magnetic hyperthermia induces both acute necrosis and a slower, ROS-mediated cell-death in treated cells. Some of the cell kill events appear to be temperature-independent, although elevated temperatures appear to amplify those effects. Overall, these results suggest the potential for effective CSC eradication by magnetic hyperthermia. Future studies will investigate the effect of magnetic hyperthermia on *in vivo* tumor growth and tumor recurrence.

■ ASSOCIATED CONTENT

● Supporting Information

Temperature profile during magnetic hyperthermia, XRD pattern of SPIO NP, representative picture of mammospheres formed, and the PI positive population and geometric mean of ROS produced by the different treatment. This material is available free of charge via the Internet at <http://pubs.acs.org>.

■ AUTHOR INFORMATION

Corresponding Author

*Department of Pharmaceutics, College of Pharmacy, University of Minnesota, 308 Harvard St. SE, Minneapolis, MN 55455. Phone: 612-624-0951. Fax: 612-626-2125. E-mail: jpanyam@umn.edu.

Notes

The authors declare no competing financial interest.

■ ACKNOWLEDGMENTS

We thank the Flow Cytometry Core Facility of the Masonic Cancer Center, a comprehensive cancer center designated by the National Cancer Institute, supported in part by P30 CA77598. Parts of this work were carried out in the Characterization Facility, University of Minnesota, which receives partial support from NSF through the MRSEC program. We thank Dr. Nisha V. Shah (Flow Cytometry Core Facility, University of Minnesota) for assistance with side population studies, Dr. Robert S. Hafner (Characterization Facility, University of Minnesota) for help with TEM studies, Ying Jing (Electrical and Computer Engineering, University of Minnesota) for help with magnetization studies and Brenda Koniar (Research Animal Resources, University of Minnesota) for assistance with animal studies. Funding support from the Department of Defense (CA093453) is also acknowledged.

■ ABBREVIATIONS

7AAD, 7-aminoactinomycin D; ALDH, aldehyde dehydrogenase; CM-H₂DCFDA, 5-(and-6)-chloromethyl-2',7'-dichlorodihydrofluorescein diacetate, acetyl ester; CSC, cancer stem cells; DPBS, Dulbecco's phosphate-buffered saline; FBS, fetal bovine serum; FT-IR, Fourier-transformed infrared spectroscopy; LDH, lactate dehydrogenase; PI, propidium iodide; ROS, reactive oxygen species; SPIO NP, superparamagnetic iron oxide nanoparticles; TEM, transmission electron microscopy

■ REFERENCES

- (1) Chandler, J. M.; Lagasse, E. Cancerous stem cells: deviant stem cells with cancer-causing misbehavior. *Stem Cell Res. Ther.* **2010**, *1* (2), 13.
- (2) Potten, C. S.; Loeffler, M. Stem cells: attributes, cycles, spirals, pitfalls and uncertainties. Lessons for and from the crypt. *Development* **1990**, *110* (4), 1001–1020.
- (3) Li, X.; Lewis, M. T.; Huang, J.; Gutierrez, C.; Osborne, C. K.; Wu, M. F.; Hilsenbeck, S. G.; Pavlick, A.; Zhang, X.; Chamness, G. C.; Wong, H.; Rosen, J.; Chang, J. C. Intrinsic resistance of tumorigenic breast cancer cells to chemotherapy. *J. Natl. Cancer Inst.* **2008**, *100* (9), 672–9.
- (4) Moitra, K.; Lou, H.; Dean, M. Multidrug efflux pumps and cancer stem cells: insights into multidrug resistance and therapeutic development. *Clin. Pharmacol. Ther.* **2011**, *89* (4), 491–502.
- (5) Bao, S.; Wu, Q.; McLendon, R. E.; Hao, Y.; Shi, Q.; Hjelmeland, A. B.; Dewhirst, M. W.; Bigner, D. D.; Rich, J. N. Glioma stem cells promote radioresistance by preferential activation of the DNA damage response. *Nature* **2006**, *444* (7120), 756–760.
- (6) Diehn, M.; Cho, R. W.; Lobo, N. A.; Kalisky, T.; Dorie, M. J.; Kulp, A. N.; Qian, D.; Lam, J. S.; Ailles, L. E.; Wong, M.; Joshua, B.; Kaplan, M. J.; Wapnir, I.; Dirbas, F. M.; Somlo, G.; Garberoglio, C.; Paz, B.; Shen, J.; Lau, S. K.; Quake, S. R.; Brown, J. M.; Weissman, I. L.; Clarke, M. F. Association of reactive oxygen species levels and radioresistance in cancer stem cells. *Nature* **2009**, *458* (7239), 780–3.
- (7) Moore, N.; Lyle, S. Quiescent, slow-cycling stem cell populations in cancer: a review of the evidence and discussion of significance. *J. Oncol.* **2011**, *2011*.

- (8) Dylla, S. J.; Beviglia, L.; Park, I. K.; Chartier, C.; Raval, J.; Ngan, L.; Pickell, K.; Aguilar, J.; Lazetic, S.; Smith-Berdan, S.; Clarke, M. F.; Hoey, T.; Lewicki, J.; Gurney, A. L. Colorectal cancer stem cells are enriched in xenogeneic tumors following chemotherapy. *PLoS One* **2008**, *3* (6), e2428.
- (9) Dewhirst, M. W.; Prosnitz, L.; Thrall, D.; Prescott, D.; Clegg, S.; Charles, C.; MacFall, J.; Rosner, G.; Samulski, T.; Gillette, E.; LaRue, S. Hyperthermic treatment of malignant diseases: current status and a view toward the future. *Semin. Oncol.* **1997**, *24* (6), 616–25.
- (10) Cotte, E.; Glehen, O.; Mohamed, F.; Lamy, F.; Falandry, C.; Golfier, F.; Gilly, F. N. Cyto-reductive surgery and intraperitoneal chemo-hyperthermia for chemo-resistant and recurrent advanced epithelial ovarian cancer: prospective study of 81 patients. *World J. Surg.* **2007**, *31* (9), 1813–20.
- (11) van der Zee, J.; Gonzalez Gonzalez, D.; van Rhoon, G. C.; van Dijk, J. D.; van Putten, W. L.; Hart, A. A. Comparison of radiotherapy alone with radiotherapy plus hyperthermia in locally advanced pelvic tumours: a prospective, randomised, multicentre trial. Dutch Deep Hyperthermia Group. *Lancet* **2000**, *355* (9210), 1119–25.
- (12) Atkinson, R. L.; Zhang, M.; Diagaradjane, P.; Peddibhotla, S.; Contreras, A.; Hilsenbeck, S. G.; Woodward, W. A.; Krishnan, S.; Chang, J. C.; Rosen, J. M. Thermal enhancement with optically activated gold nanoshells sensitizes breast cancer stem cells to radiation therapy. *Sci. Transl. Med.* **2010**, *2* (55), 55ra79.
- (13) Tseng, H. Y.; Lee, G. B.; Lee, C. Y.; Shih, Y. H.; Lin, X. Z. Localised heating of tumours utilising injectable magnetic nanoparticles for hyperthermia cancer therapy. *IET Nanobiotechnol.* **2009**, *3* (2), 46–54.
- (14) Maier-Hauff, K.; Ulrich, F.; Nestler, D.; Niehoff, H.; Wust, P.; Thiesen, B.; Orawa, H.; Budach, V.; Jordan, A. Efficacy and safety of intratumoral thermotherapy using magnetic iron-oxide nanoparticles combined with external beam radiotherapy on patients with recurrent glioblastoma multiforme. *J. Neurooncol.* **2011**, *103* (2), 317–24.
- (15) (a) Johannsen, M.; Thiesen, B.; Jordan, A.; Taymoorian, K.; Gneveckow, U.; Waldofner, N.; Scholz, R.; Koch, M.; Lein, M.; Jung, K.; Loening, S. A. Magnetic fluid hyperthermia (MFH) reduces prostate cancer growth in the orthotopic Dunning R3327 rat model. *Prostate* **2005**, *64* (3), 283–92. (b) Jones, S. K.; Winter, J. G.; Gray, B. N. Treatment of experimental rabbit liver tumours by selectively targeted hyperthermia. *Int. J. Hyperthermia* **2002**, *18* (2), 117–28. (c) Jordan, A.; Scholz, R.; Maier-Hauff, K.; van Landeghem, F. K.; Waldofner, N.; Teichgraber, U.; Pinkernelle, J.; Bruhn, H.; Neumann, F.; Thiesen, B.; von Deimling, A.; Felix, R. The effect of thermotherapy using magnetic nanoparticles on rat malignant glioma. *J. Neurooncol.* **2006**, *78* (1), 7–14. (d) Balivada, S.; Rachakatla, R. S.; Wang, H.; Samarakoon, T. N.; Dani, R. K.; Pyle, M.; Kroh, F. O.; Walker, B.; Leaym, X.; Koper, O. B.; Tamura, M.; Chikan, V.; Bossmann, S. H.; Troyer, D. L. A/C magnetic hyperthermia of melanoma mediated by iron(0)/iron oxide core/shell magnetic nanoparticles: a mouse study. *BMC Cancer* **2010**, *10*, 119.
- (16) Jain, T. K.; Morales, M. A.; Sahoo, S. K.; Leslie-Pelecky, D. L.; Labhasetwar, V. Iron oxide nanoparticles for sustained delivery of anticancer agents. *Mol. Pharmaceutics* **2005**, *2* (3), 194–205.
- (17) Tae-Youb, K.; Yamazaki, Y. Determination of the magnetic compensation composition in Al-substituted Bi-DyCoIG nanoparticles with enhanced coercive-force. *IEEE Trans. Magn.* **2004**, *40* (4), 2793–2795.
- (18) Krishna Murti, G. S. R.; Moharir, A. V.; Sarma, V. A. K. Spectrophotometric determination of iron with orthophenanthroline. *Microchem. J.* **1970**, *15* (4), 585–589.
- (19) Ho, M. M.; Ng, A. V.; Lam, S.; Hung, J. Y. Side population in human lung cancer cell lines and tumors is enriched with stem-like cancer cells. *Cancer Res.* **2007**, *67* (10), 4827–33.
- (20) Sung, J.-M.; Cho, H.-J.; Yi, H.; Lee, C.-H.; Kim, H.-S.; Kim, D.-K.; Abd El-Aty, A. M.; Kim, J.-S.; Landowski, C. P.; Hediger, M. A.; Shin, H.-C. Characterization of a stem cell population in lung cancer A549 cells. *Biochem. Biophys. Res. Commun.* **2008**, *371* (1), 163–167.
- (21) Grimshaw, M.; Cooper, L.; Papazisis, K.; Coleman, J.; Bohnenkamp, H.; Chiapero-Stanke, L.; Taylor-Papadimitriou, J.; Burchell, J. Mammosphere culture of metastatic breast cancer cells enriches for tumorigenic breast cancer cells. *Breast Cancer Res.* **2008**, *10* (3), R52.
- (22) Ginestier, C.; Hur, M. H.; Charafe-Jauffret, E.; Monville, F.; Dutcher, J.; Brown, M.; Jacquemier, J.; Viens, P.; Kleer, C. G.; Liu, S.; Schott, A.; Hayes, D.; Birnbaum, D.; Wicha, M. S.; Dontu, G. ALDH1 is a marker of normal and malignant human mammary stem cells and a predictor of poor clinical outcome. *Cell Stem Cell* **2007**, *1* (5), 555–567.
- (23) Franken, N. A. P.; Rodermond, H. M.; Stap, J.; Haveman, J.; van Bree, C. Clonogenic assay of cells in vitro. *Nat. Protocols* **2006**, *1* (5), 2315–2319.
- (24) He, L.; Yang, C. P.; Horwitz, S. B. Mutations in beta-tubulin map to domains involved in regulation of microtubule stability in epothilone-resistant cell lines. *Mol. Cancer Ther.* **2001**, *1* (1), 3–10.
- (25) Croker, A. K.; Goodale, D.; Chu, J.; Postenka, C.; Hedley, B. D.; Hess, D. A.; Allan, A. L. High aldehyde dehydrogenase and expression of cancer stem cell markers selects for breast cancer cells with enhanced malignant and metastatic ability. *J. Cell. Mol. Med.* **2009**, *13* (8B), 2236–52.
- (26) Namduri, H.; Nasrazadani, S. Quantitative analysis of iron oxides using Fourier transform infrared spectrophotometry. *Corros. Sci.* **2008**, *50* (9), 2493–2497.
- (27) Iliopoulos, D.; Hirsch, H. A.; Wang, G.; Struhl, K. Inducible formation of breast cancer stem cells and their dynamic equilibrium with non-stem cancer cells via IL6 secretion. *Proc. Natl. Acad. Sci. U.S.A.* **2011**, *108* (4), 1397–402.
- (28) Burke, A. R.; Singh, R. N.; Carroll, D. L.; Wood, J. C. S.; D'Agostino, R. B., Jr.; Ajayan, P. M.; Torti, F. M.; Torti, S. V. The resistance of breast cancer stem cells to conventional hyperthermia and their sensitivity to nanoparticle-mediated photothermal therapy. *Biomaterials* **2012**, *33* (10), 2961–2970.
- (29) Korzeniewski, C.; Callewaert, D. M. An enzyme-release assay for natural cytotoxicity. *J. Immunol. Methods* **1983**, *64* (3), 313–20.
- (30) Spagnuolo, G.; D'Anto, V.; Cosentino, C.; Schmalz, G.; Schweikl, H.; Rengo, S. Effect of N-acetyl-L-cysteine on ROS production and cell death caused by HEMA in human primary gingival fibroblasts. *Biomaterials* **2006**, *27* (9), 1803–9.
- (31) Gilchrist, R. K.; Medal, R.; Shorey, W. D.; Hanselman, R. C.; Parrott, J. C.; Taylor, C. B. Selective inductive heating of lymph nodes. *Ann. Surg.* **1957**, *146* (4), 596–606.
- (32) Kalambur, V. S.; Han, B.; Hammer, B. E.; Shield, T. W.; Bischof, J. C. In vitro characterization of movement, heating and visualization of magnetic nanoparticles for biomedical application. *Nanotechnology* **2005**, *16*, 1221–33.
- (33) (a) Wada, S.; Tazawa, K.; Furuta, I.; Nagae, H. Antitumor effect of new local hyperthermia using dextran magnetite complex in hamster tongue carcinoma. *Oral Dis.* **2003**, *9* (4), 218–23. (b) Liu, J.; Sun, Z.; Deng, Y.; Zou, Y.; Li, C.; Guo, X.; Xiong, L.; Gao, Y.; Li, F.; Zhao, D. Highly water-dispersible biocompatible magnetite particles with low cytotoxicity stabilized by citrate groups. *Angew. Chem., Int. Ed. Engl.* **2009**, *48* (32), 5875–9.
- (34) (a) Schulze, K.; Koch, A.; Petri-Fink, A.; Steitz, B.; Kamau, S.; Hottiger, M.; Hilbe, M.; Vaughan, L.; Hofmann, M.; Hofmann, H.; von Rechenberg, B. Uptake and biocompatibility of functionalized poly(vinylalcohol) coated superparamagnetic maghemite nanoparticles by synovial cells in vitro. *J. Nanosci. Nanotechnol.* **2006**, *6* (9–10), 2829–40. (b) Halbreich, A.; Roger, J.; Pons, J. N.; Geldwerth, D.; Da Silva, M. F.; Roudier, M.; Bacri, J. C. Biomedical applications of maghemite ferrofluid. *Biochimie* **1998**, *80* (5–6), 379–90.
- (35) Corot, C.; Robert, P.; Idee, J. M.; Port, M. Recent advances in iron oxide nanocrystal technology for medical imaging. *Adv. Drug Delivery Rev.* **2006**, *58* (14), 1471–504.
- (36) Rosensweig, R. E. Heating magnetic fluid with alternating magnetic field. *J. Magn. Magn. Mater.* **2002**, *252* (0), 370–374.
- (37) Hergt, R.; Andra, W.; d'Ambly, C. G.; Hilger, I.; Kaiser, W. A.; Richter, U.; Schmidt, H. G. Physical limits of hyperthermia using magnetite fine particles. *IEEE Trans. Magn.* **1998**, *34* (5), 3745–3754.
- (38) Heldin, C. H.; Rubin, K.; Pietras, K.; Ostman, A. High interstitial fluid pressure—an obstacle in cancer therapy. *Nat. Rev. Cancer* **2004**, *4* (10), 806–13.

- (39) Rebodos, R. L.; Vikesland, P. J. Effects of oxidation on the magnetization of nanoparticulate magnetite. *Langmuir* **2010**, 26 (22), 16745–53.
- (40) <http://www.magforce.de/english/clinical-trials/overview.html>.
- (41) Wehner, H.; von Ardenne, A.; Kaltofen, S. Whole-body hyperthermia with water-filtered infrared radiation: technical-physical aspects and clinical experiences. *Int. J. Hyperthermia* **2001**, 17 (1), 19–30.
- (42) Issels, R. D.; Abdel-Rahman, S.; Wendtner, C.; Falk, M. H.; Kurze, V.; Sauer, H.; Aydemir, U.; Hiddemann, W. Neoadjuvant chemotherapy combined with regional hyperthermia (RHT) for locally advanced primary or recurrent high-risk adult soft-tissue sarcomas (STS) of adults: long-term results of a phase II study. *Eur. J. Cancer* **2001**, 37 (13), 1599–608.
- (43) Charafe-Jauffret, E.; Ginestier, C.; Birnbaum, D. Breast cancer stem cells: tools and models to rely on. *BMC Cancer* **2009**, 9, 202.
- (44) Krakstad, C.; Chekenya, M. Survival signalling and apoptosis resistance in glioblastomas: opportunities for targeted therapeutics. *Mol. Cancer* **2010**, 9, 135.
- (45) Festjens, N.; Vanden Berghe, T.; Vandenabeele, P. Necrosis, a well-orchestrated form of cell demise: signalling cascades, important mediators and concomitant immune response. *Biochim. Biophys. Acta* **2006**, 1757 (9–10), 1371–87.
- (46) Apopa, P. L.; Qian, Y.; Shao, R.; Guo, N. L.; Schwegler-Berry, D.; Pacurari, M.; Porter, D.; Shi, X.; Vallyathan, V.; Castranova, V.; Flynn, D. C. Iron oxide nanoparticles induce human microvascular endothelial cell permeability through reactive oxygen species production and microtubule remodeling. *Part. Fibre Toxicol.* **2009**, 6, 1.
- (47) Seton-Rogers, S. Cancer stem cells: Survival skills. *Nat. Rev. Cancer* **2009**, 9 (3), 147–147.



Inhalable magnetic nanoparticles for targeted hyperthermia in lung cancer therapy



Tanmoy Sadhukha^a, Timothy S. Wiedmann^a, Jayanth Panyam^{a,b,*}

^a Department of Pharmaceutics, College of Pharmacy, University of Minnesota, Minneapolis, MN 55455, United States

^b Masonic Cancer Center, University of Minnesota, Minneapolis, MN 55455, United States

ARTICLE INFO

Article history:

Received 4 February 2013

Accepted 20 March 2013

Available online 13 April 2013

Keywords:

Superparamagnetic iron oxide

Magnetic hyperthermia

EGFR

Inhalation delivery

Lung cancer

ABSTRACT

Lung cancer (specifically, non-small cell lung cancer; NSCLC) is the leading cause of cancer-related deaths in the United States. Poor response rates and survival with current treatments clearly indicate the urgent need for developing an effective means to treat NSCLC. Magnetic hyperthermia is a non-invasive approach for tumor ablation, and is based on heat generation by magnetic materials, such as superparamagnetic iron oxide (SPIO) nanoparticles, when subjected to an alternating magnetic field. However, inadequate delivery of magnetic nanoparticles to tumor cells can result in sub-lethal temperature change and induce resistance while non-targeted delivery of these particles to the healthy tissues can result in toxicity. In our studies, we evaluated the effectiveness of tumor-targeted SPIO nanoparticles for magnetic hyperthermia of lung cancer. EGFR-targeted, inhalable SPIO nanoparticles were synthesized and characterized for targeting lung tumor cells as well as for magnetic hyperthermia-mediated antitumor efficacy in a mouse orthotopic model of NSCLC. Our results show that EGFR targeting enhances tumor retention of SPIO nanoparticles. Further, magnetic hyperthermia treatment using targeted SPIO nanoparticles resulted in significant inhibition of *in vivo* lung tumor growth. Overall, this work demonstrates the potential for developing an effective anticancer treatment modality for the treatment of NSCLC based on targeted magnetic hyperthermia.

© 2013 Elsevier Ltd. All rights reserved.

1. Introduction

Despite earlier diagnosis and the availability of new molecularly-targeted drugs, lung cancer (specifically, non-small cell lung cancer; NSCLC) is still the leading cause of cancer-related deaths in the United States [1]. Surgical resection is the primary choice of treatment, followed by radiation and/or chemotherapy [2]. Metastatic and locally advanced disease stages are not amenable to surgical resection, and importantly, a majority of patients who undergo surgery eventually experience relapse [3–5]. Poor response rates and survival with current treatments clearly indicate the urgent need for developing an effective means to treat non-small cell lung cancer.

Magnetic hyperthermia is a novel non-invasive approach for tumor ablation and is based on heat generation by magnetic materials, such as superparamagnetic iron oxide (SPIO)

nanoparticles, when subjected to an alternating magnetic field (AMF) [6,7]. Depending on the size of SPIO nanoparticles and the frequency of AMF, heat is generated through either Néel or Brownian relaxation. The heat generated dissipates over short distances due to the high thermal conductivity of water and can, therefore, be used for highly focused heating [8,9]. However, inadequate delivery of magnetic nanoparticles to tumor cells can result in sub-lethal temperature change and induction of resistance [10]. Additionally, non-targeted delivery of these particles to the healthy tissues can result in heat damage to normal tissues.

In our studies, we developed epidermal growth factor receptor (EGFR)-targeted, inhalable SPIO nanoparticles for magnetic hyperthermia of non-small cell lung cancer (NSCLC). EGFR overexpression has been observed in as many as 70% of NSCLC patients [11–13], in whom EGFR expression is elevated in epithelial sites within tumors than in sites adjacent to and distant from tumors. We examined the effect of EGFR targeting on accumulation and retention of inhaled SPIO nanoparticles in the tumor tissue and the effect of targeted magnetic hyperthermia therapy on tumor growth in an orthotopic lung tumor model.

* Corresponding author. Department of Pharmaceutics, College of Pharmacy, University of Minnesota, Minneapolis, MN 55455, United States. Tel.: +1 612 624 0951; fax: +1 612 626 2125.

E-mail addresses: jpanyam@umn.edu, jpanyam@gmail.com (J. Panyam).

2. Materials and methods

2.1. Materials

Ferrous chloride tetrahydrate, ferric chloride hexahydrate, myristic acid, pluronic f127, ascorbic acid, potassium hydroxide, 1,10 phenanthroline and sodium acetate were purchased from Sigma (St. Louis, MO). Penicillin/streptomycin, fetal bovine serum, RPMI 1640, Dulbecco's phosphate buffered saline, F-12K (Kaighn's modification) and trypsin–EDTA solution were obtained from Invitrogen Corporation (Carlsbad, CA).

2.2. Synthesis of carboxy-terminated pluronic f127 (CTP)

The synthesis of CTP involved the use of an acid anhydride, which is highly susceptible to the presence of moisture. Hence, all the solvents used in the reaction were anhydrous and the reaction environment was maintained as dry as possible. A mass of 2 g of pluronic f127 was dissolved in 40 ml of anhydrous tetrahydrofuran. To the solution, 100 mg of 4-dimethylaminopyridine, 72 μ l of triethylamine and 800 mg of succinic anhydride were added, and the flask was sealed immediately. The mixture was stirred at room temperature for 48 h under nitrogen atmosphere. After 2 days, the volatile solvent was removed by rotary evaporation, and the dry residue was dissolved in 40 ml of carbon tetrachloride. The undissolved, unconjugated succinic anhydride was removed by filtration. The remaining polymer solution was concentrated using a rotary evaporator, and CTP was precipitated by drop-wise addition of the solution in cold, dry diethyl ether [14]. The residue was filtered, dried in a vacuum oven at 40 °C overnight and analyzed by proton NMR. The final yield of CTP was 1.74 g.

Completion of the reaction was confirmed by NMR. Around 25 mg of CTP was dissolved in 750 μ l of deuterated water and analyzed using a 400 MHz NMR. The NMR spectrum of unmodified pluronic f127 was also obtained for comparison.

2.3. Conjugation of EGFR-targeting peptide or the isotype scrambled peptide to CTP

A mass of 42 mg of CTP was dispersed in 1.8 ml deionized water. To this solution, 10 mg of *N*-(3-Dimethyl aminopropyl)-*N'*-ethylcarbodiimide hydrochloride (EDC) and 14 mg of *N*-hydroxysulfosuccinimide sodium salt (sulfo-NHS) (each dissolved in 100 μ l deionized water) were added and then stirred for 15 min at room temperature. The pH of the reaction mixture was 6–7. The excess unreacted EDC was quenched by the addition of β -mercaptoethanol at a final concentration of 130 mM. 10 mg of either the EGFR-targeted peptide (YHWYGYTPQNV) or the scrambled peptide (HWPYAHPTHPSW) [15] was dissolved in 200 μ l of deionized water and added to the reaction mixture. 245 μ l of 10 \times PBS was added to buffer the reaction and the pH was maintained around 7–8. The reaction mixture was stirred overnight at room temperature [16]. The solution was dialyzed against water for 48 h using a 3500 Da molecular weight cutoff Slide-a-lyzer[®] dialysis cassette, and the final solution was lyophilized (Labconco, FreeZone 4.5, Kansas City, MO).

Conjugation of the peptides to CTP was confirmed by NMR. Around 25 mg of the conjugate was dissolved in 750 μ l of deuterated water and analyzed by a 400 MHz NMR. NMR spectra of the free peptides were used for identification of the resonances corresponding to the peptide.

2.4. Synthesis of water-dispersible SPIO nanoparticles

SPIO nanoparticles were synthesized from iron chlorides by the addition of a strong base, followed by coating with a fatty acid to prevent oxidation and then with a surfactant to form a stable aqueous dispersion [17]. Specifically, 0.82 g of ferric chloride hexahydrate and 0.33 g of ferrous chloride tetrahydrate were dissolved in 30 ml of degassed and nitrogen-purged water, and 3 ml of 5 M ammonium hydroxide was added drop-wise to this solution, which was then stirred for 30 min. The resulting iron oxide nanoparticles were washed three times with nitrogen-purged water, sonicated in a water-bath sonicator for 2 min, and then heated to 80 °C. About 100 mg of myristic acid was added to the heated mixture and stirred for another 30 min. Excess myristic acid was removed by two washes with ethanol, followed by two additional washes with water to remove excess ethanol. Each wash was followed by magnetic separation of nanoparticles. Myristic acid coated particles were then suspended in 30 ml water using a water-bath sonicator. Targeted or scrambled peptide conjugated pluronic, equivalent to 5% surface coverage of the peptide (5.5 mg and 11.7 mg of targeted and scrambled peptides, respectively), was mixed with pluronic f127 to yield a total mass of 100 mg, which was then added to the suspension and sonicated in a bath sonicator for 1 h. Every step of the synthesis was conducted carefully to minimize exposure to atmospheric oxygen.

2.5. Characterization of SPIO nanoparticles

The average hydrodynamic diameter of SPIO nanoparticles was determined by dynamic light scattering. About 1 mg of SPIO nanoparticles was dispersed in 2 ml of deionized water by sonication and the dispersion was subjected to particle size analysis using a Delsa[™] Nano C Particle Analyzer (Beckman, Brea, CA). The measurement was performed at 25 °C and at a 165° scattering angle. Mean

hydrodynamic diameter was calculated based on size distribution by weight, assuming a lognormal distribution. Five individual size measurement runs were performed, with each run recording 150 size events.

The iron content of the SPIO nanoparticles was measured using the 1,10 phenanthroline-based iron assay [18]. SPIO nanoparticles were first dissolved in 12 N hydrochloric acid. The solution was then diluted with distilled water to obtain a final acid concentration of 0.2 N. To the acid solution of SPIO nanoparticles, 10 mg/ml ascorbic acid, 1.2 mg/ml 1,10 phenanthroline, 22.4 mg/ml potassium hydroxide and 123 mg/ml sodium acetate were added in a volume ratio of 1:1:1:1:5. Absorbance of the resultant solution was measured at 490 nm using a microplate reader (ELx800 absorbance microplate reader, Biotek, Winooski, VT). Ferric chloride (hexahydrate) solution in 0.2 N hydrochloric acid was used as a standard.

2.6. Magnetic heating rate

SPIO nanoparticles were dispersed in 1 ml of Hank's F-12K medium in 10 mm \times 75 mm disposable borosilicate glass cell culture tubes. Magnetic heating was performed using an induction heating system (1 kW Hotshot, Ameritherm Inc., Scottsville, NY) by placing the suspension at the center of a multiturn copper coil that generated AMF (nominal magnetic field strength of 6 kA/m and frequency of 386 kHz). The temperature change was measured using a fluoroptic[®] probe (Lumasense Technologies, Santa Clara, CA) at five second intervals. Samples were equilibrated to 37 °C using a water-bath before exposure to the field.

2.7. Aerosol generation and characterization

Aerosolization of SPIO nanoparticles was achieved by ultrasonic atomization [19]. A Pyrex glass baffle was constructed in-house and placed in a water-bath, directly over a 1.7 MHz ultrasonic transducer [20]. About 13 ml of SPIO nanoparticle dispersion in 40% ethanol, containing 8 mg magnetite per milliliter was loaded into the baffle. Compressed air directed into the baffle at a flow rate of 0.5 L/min (as measured by an inline flow meter) entrained the aerosol droplets containing the SPIO nanoparticle dispersion and carried the particles into a subsequent drying assembly. The iron oxide output in the aerosol was measured by collecting the aerosolized and dried SPIO particles for a predetermined period of time on Whatman quartz microfiber filters suitable for air sampling [21]. The filters were assayed using the above procedure and the iron oxide output rate was calculated as iron oxide amount collected per unit time.

The aerosol particle size distribution was determined with a Mercer style seven-stage Intox cascade impactor operating at a sample flow rate of 0.5 L/min. The aerosol generated was passed through a heated drying column before passing through the cascade impactor. Aerosol particles deposited at each stage of the cascade impactor were collected and analyzed by iron assay to obtain the particle size distribution. The mass median aerodynamic diameter (MMAD) and associated geometric standard deviation (GSD) were calculated from linear regression of an X-probability plot of the cumulative undersized mass as a function of logarithm of the impactor stage cutoff diameter using OriginPro 8 software (OriginLab Corporation, Northampton, MA) [21].

2.8. Cell culture studies

A549 (human lung adenocarcinoma) and A549-luc (luciferase-transfected A549) cells were used in the study. Both cell lines were propagated using F-12K medium supplemented with 10% fetal bovine serum (FBS) and 1% antibiotic solution and maintained at 37 °C and in 5% carbon dioxide.

2.8.1. Demonstration of role of EGFR in tumor cell uptake of functionalized nanoparticles

A549 cells were plated in a 6-well plate 4 h before the start of the study. Cells were washed with phosphate buffered saline (PBS) to remove non-adherent cells and 1 mg (magnetite equivalent) of targeted SPIO particles, scrambled peptide-conjugated particles, particles without any peptide, or targeted particles with excess free targeting peptide were added to the cells in a total volume of 2 ml of cell culture medium containing 5% FBS. The plates were incubated on ice for 30 min, washed thrice with PBS and incubated at 37 °C for an additional 45 min. At the end of the incubation, cells were lysed with 400 μ l of RIPA buffer and assayed for total cell protein content and iron content [18] (by iron assay procedure described before).

To evaluate EGFR targeting on the effectiveness of magnetic hyperthermia, plated A549 cells were incubated with targeted or non-targeted particles for 30 min at 4 °C, washed three times with PBS, incubated at 37 °C for 45 min and then subjected to AMF (6 kA/m at 386 kHz frequency). Following AMF exposure, 10 μ M propidium iodide was added to the cells and observed under a fluorescent microscope immediately and at 24 h after AMF exposure.

2.9. Orthotopic lung tumor model

All animal studies were carried out in compliance with protocol approved by the Institutional Animal Care and Use Committee at the University of Minnesota. Female

Fox Chase SCID® Beige mice (CB17.Cg-Prkd^{scid}Lysf^{bg-J}/CrI) 4–5 weeks of age, were obtained from Charles River Laboratories.

A mouse orthotopic lung tumor model [22] was used in the studies. Lung tumor cells that have been stably transfected with firefly luciferase were used to facilitate the visualization of tumor cells in live animals using bioluminescence imaging. A549-luc-C8 Bioware® Cell Line (Caliper Lifesciences) is a luciferase expressing cell line derived from A549 human lung squamous carcinoma cells by stable transfection of the North American Firefly Luciferase gene expressed from the CMV promoter. Intravenous injection of 1×10^6 A549-luc-C8 cells led to detectable increase in bioluminescence in the lungs by 2 weeks.

2.10. Lung delivery of SPIO nanoparticles

2.10.1. Tracheal instillation

The mice were anesthetized and placed on a rodent intubation stand, supported by their incisors. The tongue was rolled out using a sterile cotton swab and held between the fingers. A fiber-optic light and stylus (BioLite, BioTex, Inc., TX) connected to an endotracheal tube was used to visualize the tracheal opening and to carefully insert the attached endotracheal tube into the trachea. An inflation bulb was used to confirm the proper insertion of the endotracheal tube by monitoring the inflation of the thoracic region on gently pushing in air through the tube. Targeted or non-targeted SPIO particles (50 μ l, 10 mg/ml iron oxide equivalent) were instilled through the endotracheal tube. The mice were kept upright for a minute to prevent back-flow of the liquid and then placed on a heating pad to assist in faster recovery from anesthesia [23].

2.10.2. Inhalation

The aerosol was generated as described above, but the dried SPIO aerosols were directed through the drying assembly into an animal chamber, which comprised a 4-port double-walled chamber. The dried aerosol stream entered the top inlet into a stirred chamber. The animals were placed into each port with their nose exposed to the aerosol stream in the stirred chamber. The exhaust tube was connected to the space between the two walls, thus ensuring that the mice underwent a “nose-only” exposure for 30 min. Filter collections were made three times both before and after the exposure to measure the aerosol output. The aerosol stream was also passed through a seven-stage Intox cascade impactor before each exposure to determine the aerosol particle size distribution (MMAD and GSD) [21].

2.11. Distribution of SPIO nanoparticles following instillation and inhalation delivery

Targeted or scrambled peptide conjugated SPIO nanoparticles were administered to tumor-bearing animals ($n = 6$ per time point per group) by the two routes of administration described above. The animals were euthanized at 1 h, 1 day or 1 week after SPIO administration. The lungs, liver, spleen, kidney, heart, stomach and blood were collected to analyze the distribution of SPIO particles. Additionally, lungs of treated animals were also sectioned, stained with hematoxylin and eosin (H&E staining) and Prussian blue (for iron) [24] and imaged after the last time point to visualize the distribution of SPIO particles. Basal level of iron in each organ was determined in six healthy mice and subtracted from the assayed iron content in the treatment groups. The difference was used to determine the contribution of SPIO nanoparticle administration to tissue iron concentrations.

2.12. In vivo efficacy of targeted magnetic hyperthermia after inhalation delivery of SPIO nanoparticles

Fox Chase SCID® Beige mice were injected with A549-luc cells intravenously to facilitate the development of tumors in the lungs. Once the lung bioluminescence reached about 0.5×10^6 photons/s, animals were administered SPIO nanoparticles by inhalation. After 7 days, some of the treated animals were subjected to 30 min of magnetic hyperthermia. Untreated animals and animals receiving the particles without exposure to AMF served as controls. Lung bioluminescence was monitored three times weekly for 4 weeks. At the end of the study, animals were euthanized, and the lungs and trachea were removed and weighed. Assuming little variability between the lung weights of individual mice, the differences in lung weights were attributed to the variable mass of lung tumors.

2.13. Statistical analysis

Statistical analyses were performed using one-way ANOVA, followed by Bonferroni–Holm method for comparison between individual groups. A probability level of $P < 0.05$ was considered significant.

3. Results

3.1. Characterization of inhalable SPIO nanoparticles

Conversion of the hydroxyl end group of pluronic f127 into a carboxyl group was confirmed using NMR spectroscopy and the

conversion efficiency was almost 100% (Fig. 1a and b). Presence of targeted or scrambled peptides could be detected in the NMR spectra of the modified polymer (Fig. 1c–f). The conjugation efficiency of EGFR-targeted peptide and scrambled peptide to CTP was $90.4 \pm 10.5\%$ and $42.8 \pm 4.6\%$ respectively. SPIO nanoparticles were composed of $74 \pm 2\%$ w/w iron oxide, coated with $10 \pm 3\%$ w/w myristic acid, and stabilized by $16 \pm 2\%$ w/w pluronic f127. The hydrodynamic diameter of unconjugated (pluronic COOH terminated) SPIO nanoparticles was 309 ± 24 nm while that of targeted peptide and scrambled peptide-conjugated particles was 369 ± 34 nm and 365 ± 45 nm, respectively. The heating rate of SPIO nanoparticles was concentration-dependent, and was similar for both targeted and non-targeted SPIO nanoparticles (Fig. 1g).

3.2. In vitro cell uptake and cell kill efficiency of targeted SPIO nanoparticles

Non-specific uptake of SPIO nanoparticles in A549 cells was determined as a function of time of incubation, concentration of serum in the culture medium and the incubation temperature. From these studies, an incubation time of 30 min and low serum concentration were found to be optimal for minimizing the non-specific uptake of SPIO nanoparticles. Using these optimized parameters, an *in vitro* study was performed to determine the effect of EGFR targeting on cellular uptake of SPIO nanoparticles. Nanoparticle uptake into cells was 4.5-fold higher for the EGFR-targeted formulation than that for the non-targeted control. Conjugation of scrambled peptide did not result in enhancement of particle uptake into cells, and the presence of excess targeting ligand decreased the cellular uptake of targeted nanoparticles, showing the specific role of EGFR in tumor cell uptake of targeted nanoparticles (Fig. 2a). Some of the experimental conditions (low serum, initial 4 °C, low incubation time) used in this assay are not representative of physiological conditions. However, the goal here was to demonstrate that targeted particles bind to the tumor cells to a higher extent relative to non-targeted particles. The parameters used here facilitated binding of particles to cells while minimizing non-specific uptake.

To determine the effect of EGFR targeting on the effectiveness of magnetic hyperthermia, plated A549 cells were incubated with targeted or non-targeted SPIO nanoparticles, washed and subjected to AMF. Enhanced cellular accumulation of EGFR-targeted SPIO nanoparticles could be visualized under the microscope as dark spots on the cells (Fig. 2e and f). Magnetic hyperthermia with targeted nanoparticles resulted in greater number of cells taking up propidium iodide, indicating enhanced cell death with targeted SPIO nanoparticles (Fig. 2b–f).

3.3. In vivo lung deposition and retention after inhalation delivery

Ultrasonic atomization of SPIO nanoparticle dispersions resulted in aerosols with a MMAD of 1.1 ± 0.1 μ m and GSD of 1.9 ± 0.1 (Supp. Inf. 1). The iron oxide output rate was determined to be 270 ± 70 μ g/min. The high iron oxide output and the MMAD size range point to the possibility of a high deposition of these aerosol particles in the mouse lung even with a relatively short exposure time.

Following aerosol exposure, iron oxide concentration in the lungs at 1 h (Fig. 3a) was similar for targeted and non-targeted SPIO nanoparticles in tumor-bearing lungs as well as for blank SPIO particles in healthy lungs, showing that the presence of tumor did not affect the total deposition of particles. It also suggested that targeting does not affect the lung concentration immediately after the administration of particles. However, 1 week following inhalation, the lung concentration of non-targeted particles decreased

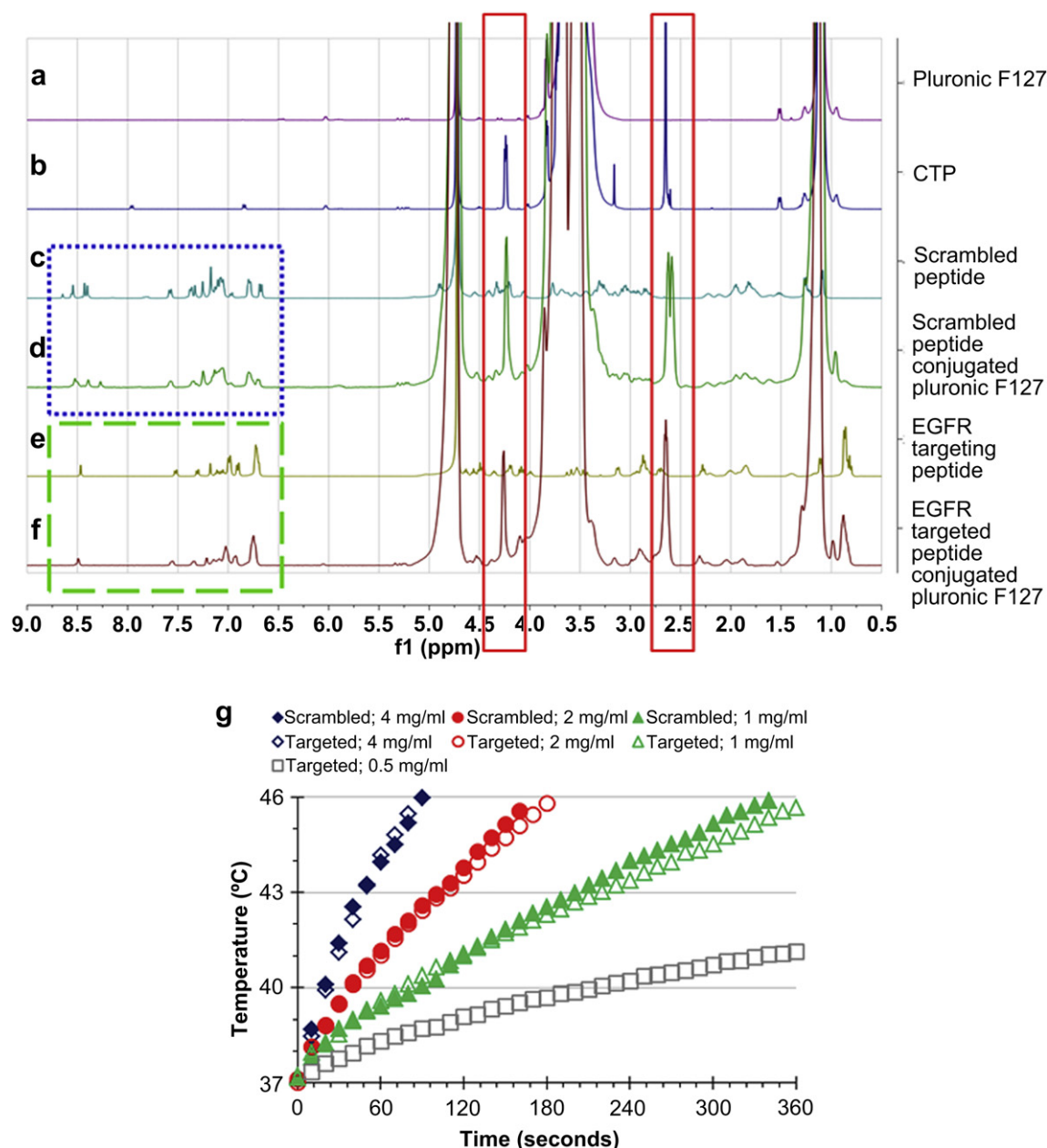


Fig. 1. SPIO NP formulation and characterization. (a–f) NMR spectra of modified pluronic f127. (a) Pluronic f127 has a characteristic NMR peak at 1.02 ppm and multiple peaks between 3 and 4 ppm. (b) Conjugation of carboxy end group can be detected by the appearance of new peaks at 2.6 and around 4.2 ppm (solid box). NMR spectrum of (e) EGFR-targeting peptide is different from (c) scrambled peptide with the most visible difference between 6 and 9 ppm. Peptide conjugation to the carboxy-terminated pluronic (CTP) can be verified from the presence of both carboxy modification peaks (solid box) and (f) EGFR-targeting peptide (dotted box) or (d) scrambled peptide (dashed box) peaks. (g) **Heating rates of targeted and non-targeted SPIO nanoparticles.** SPIO nanoparticle dispersions were placed in an alternating magnetic field of 6 kA/m and operating at a frequency of 386 kHz. The initial temperature was equilibrated to 37 $^{\circ}\text{C}$, and the temperature of SPIO NP dispersion was measured at 10 s intervals using a fluoroptic probe.

while the level of targeted particles was almost constant, demonstrating the effectiveness of EGFR targeting in improving particle retention within tumor-bearing lungs.

Inhalation delivery resulted in a homogenous distribution of SPIO nanoparticles throughout the lung (Fig. 3b and c). One week after inhalation, a significantly higher amount of Prussian blue staining was observed in the mice that received targeted particles compared to those that received non-targeted particles. In the former, the staining was observed in and around tumor cells (Fig. 3d and e), with near complete absence of particles from the healthy parts of the lung. In contrast, the latter group did not display much staining in either the tumor or the healthy regions of the lung (not shown).

3.4. Biodistribution of SPIO nanoparticles after high dose instillation into lungs

To study the effect of elevated lung dose of SPIO nanoparticles on the overall body distribution, we used tracheal instillation. Unlike inhalation delivery, which restricts the dose deposited in mouse lungs to 72.5 ± 14.1 μg of magnetite, tracheal instillation allows for a higher dose (386 ± 95 μg of magnetite) to be delivered.

Following instillation, SPIO particles were mostly observed in the lungs after 1 h, although some particles were also present in the stomach, due to the mucociliary clearance from the lung. There was no significant difference between the levels of targeted and non-targeted particles in the different organs 1 h or 1 day after

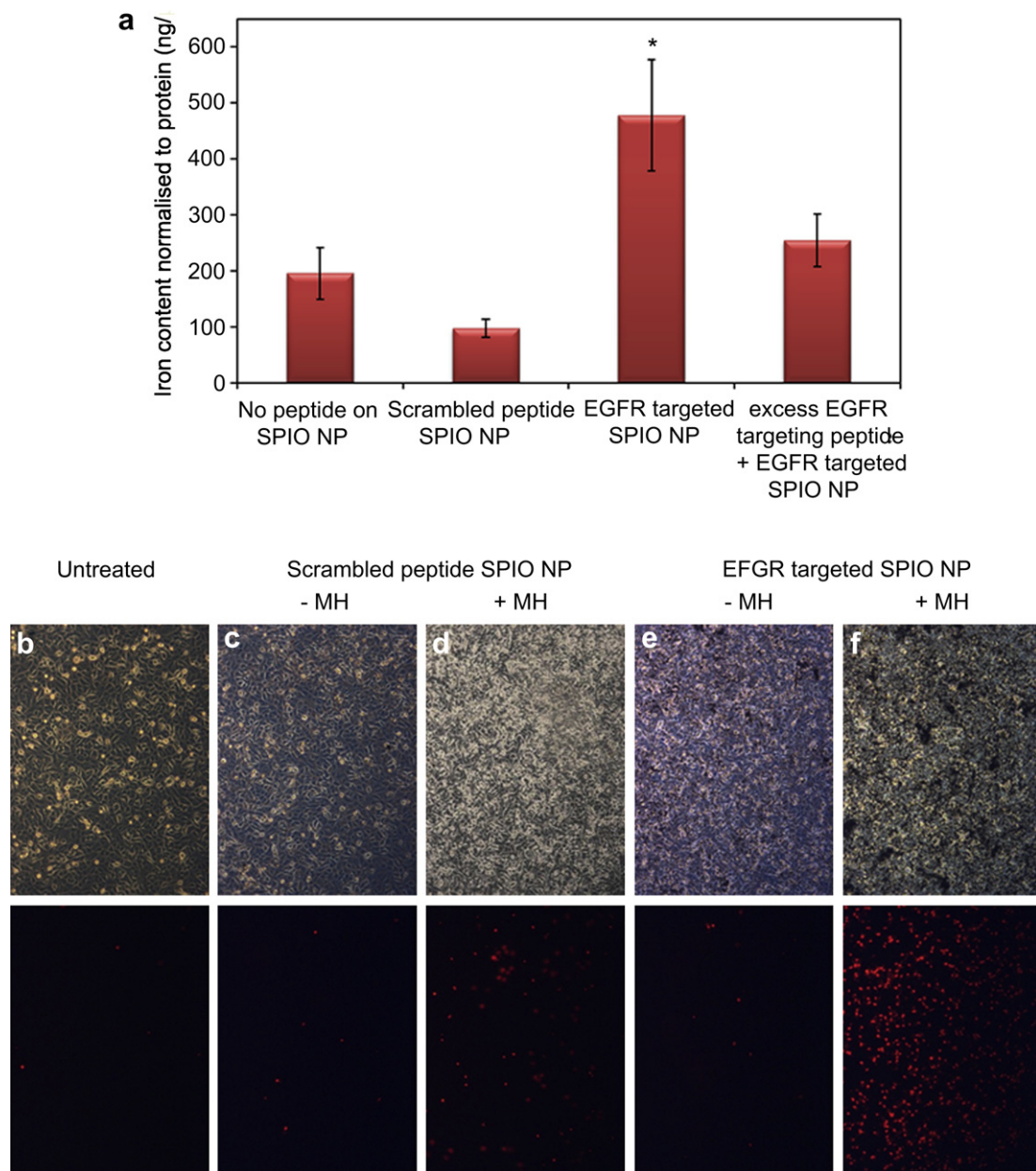


Fig. 2. *In vitro* cell uptake (a) and cell kill efficacy (b–f) of EGFR-targeted SPIO nanoparticles. (a) SPIO nanoparticles bearing EGFR-targeting peptide, scrambled peptide or no peptide on the surface were incubated with A549 cells at 4 °C for 30 min, washed with PBS and further incubated at 37 °C for 45 min. The specific role of EGFR in enhanced accumulation was determined by adding excess EGFR-targeting peptide to competitively inhibit the binding of targeted SPIO nanoparticles. Iron content of the lysed cells was used to calculate the cellular uptake of SPIO nanoparticles. $n = 3$. * $P < 0.05$ compared to other controls. (b–f) A549 cells were incubated with (b) culture medium, (c and d) non-targeted or (e and f) targeted SPIO nanoparticles and subjected to magnetic hyperthermia (MH) for 30 min (d and f). PI was added immediately before MH treatment. The top panel shows the phase contrast microscopic images, while the bottom panel shows the corresponding fluorescent microscopic images of PI positive cells.

instillation. The concentration of both particles in blood and other organs (except lung) decreased 1 week after instillation compared to 1 h or 1 day time points (Fig. 4a and b). On the contrary, while the lung concentration of non-targeted particles decreased over the period of 1 week, the level of targeted particles was fairly constant over 1 week. The final concentration of targeted particles was significantly higher (60%) than non-targeted particles 1-week post-instillation (Fig. 4c). In contrast to the high lung concentration, the amount of iron in the other tissues was virtually unchanged throughout the duration of the study and was not considerably different from the basal level of iron in the tissues of untreated animals (Fig. 4d). This data suggested that pulmonary delivery of

targeted SPIO nanoparticles can circumvent non-specific distribution into organs such as liver and spleen, which commonly receive the highest dose of intravenously administered therapeutics [25].

While both instillation and inhalation resulted in a significant increase in lung concentration of particles with EGFR targeting, the absolute amount of SPIO particles in the two cases were different. The lung iron content after instillation was 4.5–5-fold higher than that after inhalation (400 vs 80 μg for EGFR-targeted SPIO nanoparticles, Figs. 3 and 4). This is likely due to the higher dose of particles delivered to the lung through instillation. However, aerosol delivery is a more convenient route of administration in humans than instillation. Additionally, inhalation resulted in a

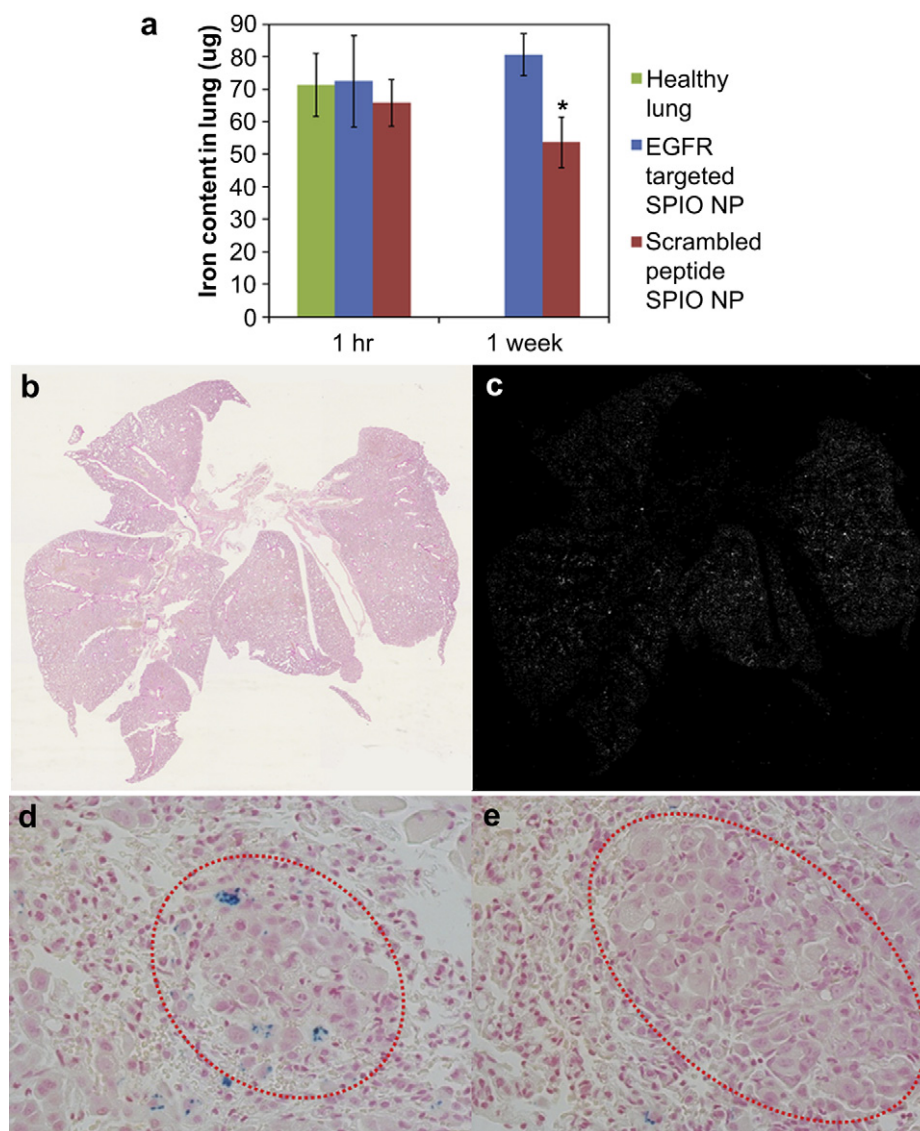


Fig. 3. (a) *In vivo* lung deposition and retention of SPIO nanoparticles after inhalation delivery. Healthy mice or those bearing orthotopic A549 tumors were allowed to inhale targeted or non-targeted SPIO nanoparticles for 30 min. Animals were euthanized 1 h or 1 week after inhalation delivery and the lungs were assayed for iron content ($n = 4$; $*P < 0.01$ compared to non-targeted group at 1 week after inhalation). (b and c) **Distribution of SPIO nanoparticles in mouse lung after inhalation.** One hour after inhalation of SPIO nanoparticles, animals were euthanized, lungs were collected, sectioned and stained with Prussian blue. Due to the difficulty in visualizing Prussian blue staining of the entire mouse lung (b), an image processing software (Image Pro Plus) was used to pseudo-color the Prussian blue stain white against a black background (c). (d and e) **Prussian blue staining of lung tumor section after SPIO nanoparticle inhalation.** One week after inhalation of targeted (d) or non-targeted SPIO nanoparticles (e), mice were euthanized, lungs were collected, sectioned and stained with Prussian blue. The sections show the presence of SPIO nanoparticles in tumor nodules (marked by red ovals) in EGFR-targeted group (100 \times magnification).

more even distribution of the SPIO nanoparticles throughout the lungs at the time of administration (Fig. 3a) compared to instillation, where most of the instilled dose resided near the major airways, with almost no particles reaching the periphery (Supp. Inf. 2).

3.5. *In vivo* efficacy after inhalation

Magnetic hyperthermia using non-targeted SPIO particles resulted in an insignificant decrease in lung tumor bioluminescence ($P > 0.05$) relative to that in animals that received the same particles but were not exposed to AMF. Targeted SPIO nanoparticles mediated hyperthermia showed significantly lower lung tumor bioluminescence ($P < 0.05$) (Fig. 5a). The lung weights at the end of the study agreed with the bioluminescence data; magnetic

hyperthermia with targeted particles resulted in a significantly lower final lung weight compared to the other groups (Fig. 5b).

These *in vivo* results thus confirm that EGFR targeting enhances the tumor concentration of SPIO nanoparticles, which translated into more effective tumor cell kill. In addition, the treated mice showed no signs of distress over the duration of the study (30 days after magnetic hyperthermia treatment), suggesting that this procedure does not result in acute systemic toxicity or damage to healthy lung tissue. Additionally, the dose of particles that could be delivered to the tumor by inhalation was limited by the small lung volume and the obligate nose-breathing of mice [26]. A similar approach can be expected to be more effective in humans, because a higher deposition can be achieved with inhalation through the oral cavity and control of the respiration.

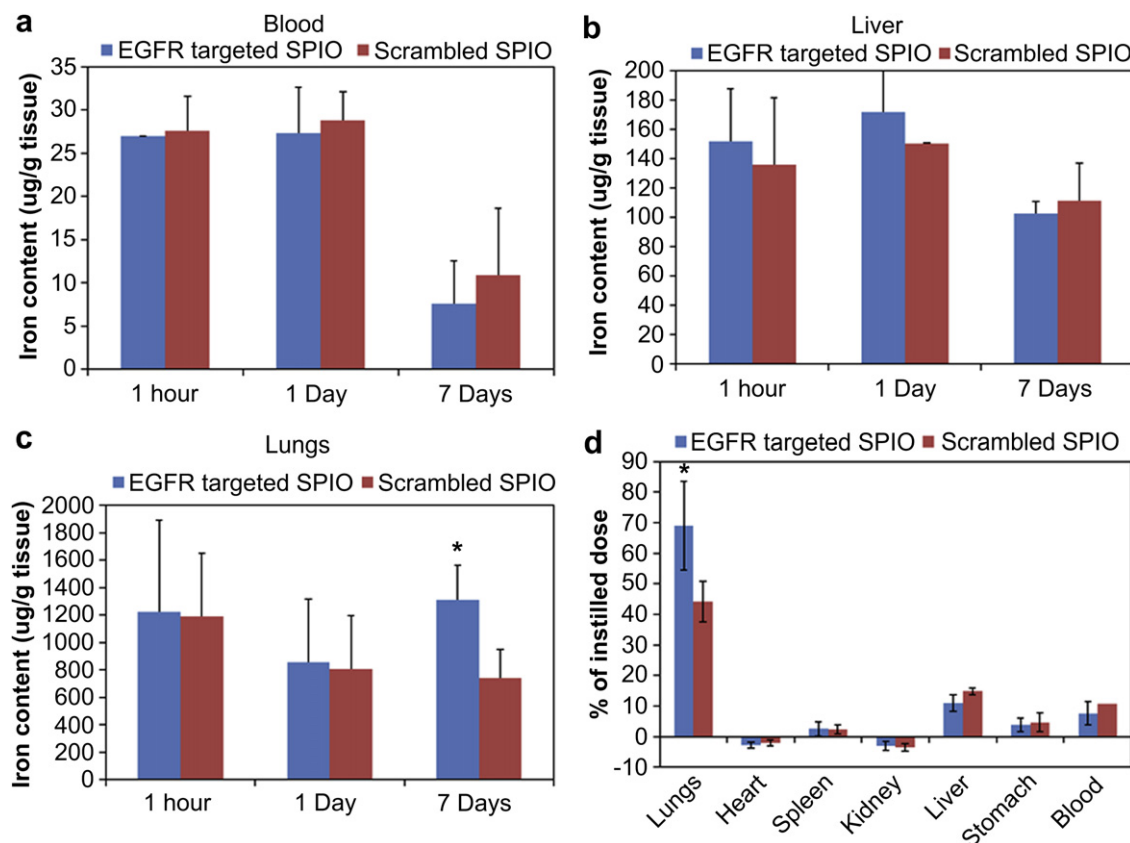


Fig. 4. (a–c) **Iron content in different tissues after SPIO nanoparticle instillation.** Iron content in (a) blood, (b) liver and (c) lung after 1 h, 1 day or 1 week after instillation of targeted or non-targeted SPIO nanoparticles. Iron concentration remained elevated in blood and liver for 24 h after instillation and decreased after a week. There was no significant effect of targeting on the iron levels in blood and liver ($n = 4$). In contrast, EGFR targeting enhanced lung retention of SPIO nanoparticles over a week ($n = 4$; $*P < 0.05$ compared to non-targeted group at 1 week after instillation). (d) **Distribution of SPIO nanoparticles 1 week post-instillation.** Iron content in lungs, heart, spleen, kidneys, liver, stomach and blood are shown as a percent of instilled dose. Overall levels of iron in the organs were low except for the lungs ($n = 4$; $*P < 0.05$ compared to non-targeted group at 1 week after instillation).

4. Discussion

Magnetic hyperthermia, which involves the use of superparamagnetic substances to generate heat through application of an external AMF, is a non-invasive approach for lung tumor ablation. The relatively inert nature of the magnetic substances in the absence of magnetic field and their efficacy in the presence of AMF make this technique highly suitable for achieving an on-demand response. Magnetic hyperthermia is particularly suitable for the treatment of lung cancer since unlike the abdomen, the thoracic region, where the external AMF can be easily focused, is only inhabited by the lungs and the heart. Additionally, lungs are filled with air, which act as a poor conductor of heat. Thus, the heat generated by the particles in the lungs is less likely to affect the surrounding organs such as the heart. Finally, studies have shown that normal, non-malignant cells are more resilient to heat damage than tumor cells [27], thereby minimizing the chances of damage to healthy lung tissue. Recent reports have suggested that magnetic hyperthermia is effective in murine subcutaneous lung tumor models [28,29]. However, in spite of the promise of a highly effective treatment option, no studies have so far assessed the effectiveness of magnetic hyperthermia in an orthotopic lung tumor model.

Although the lung is a highly perfused organ, intravenous delivery of anticancer therapeutics targeted to the lung results in broad, non-specific distribution of the therapeutic agents to normal organs, resulting in severe systemic side effects [30]. While many

solid tumors are not amenable to local delivery, lung tumors of the epithelial origin can potentially be accessed by inhalation route. This allows for maximizing the concentration of the therapeutic agent in the target organ, i.e., the lungs, while minimizing exposure to other normal organs. Lung clearance of particulates into systemic circulation is primarily attributed to the alveolar macrophages, which leads to a lower blood concentration of the therapeutics than through intravenous administration. Several reports have shown that pulmonary delivery improves retention of therapeutic agents in the lungs while limiting their concentration in the blood thereby reducing their levels in the healthy organs [25,31]. Our studies show that lung delivery through either instillation or inhalation results in therapeutically effective concentrations of SPIO nanoparticles in lungs with minimal exposure to other organs. An hour after instillation of SPIO nanoparticles, the average lung concentration of iron oxide was 1.2 mg/g of tissue. In contrast, the average liver and blood concentration were 130 $\mu\text{g/g}$ and 27 $\mu\text{g/g}$ of tissue, respectively. The other organs including spleen, kidney and heart contained less than 2% of the instilled dose. This demonstrates that inhalation delivery is an effective means to enhance local concentration of therapeutics into the lungs.

It was interesting to note that the iron concentration in blood was high at 1 h and 1 day, but then decreased at 7 days after tracheal instillation. There are two possible explanations for this observed result. First, despite careful dosing into the trachea, a part of the instilled dose could get regurgitated and swallowed by the animals. The SPIO particles in the stomach can dissolve in the

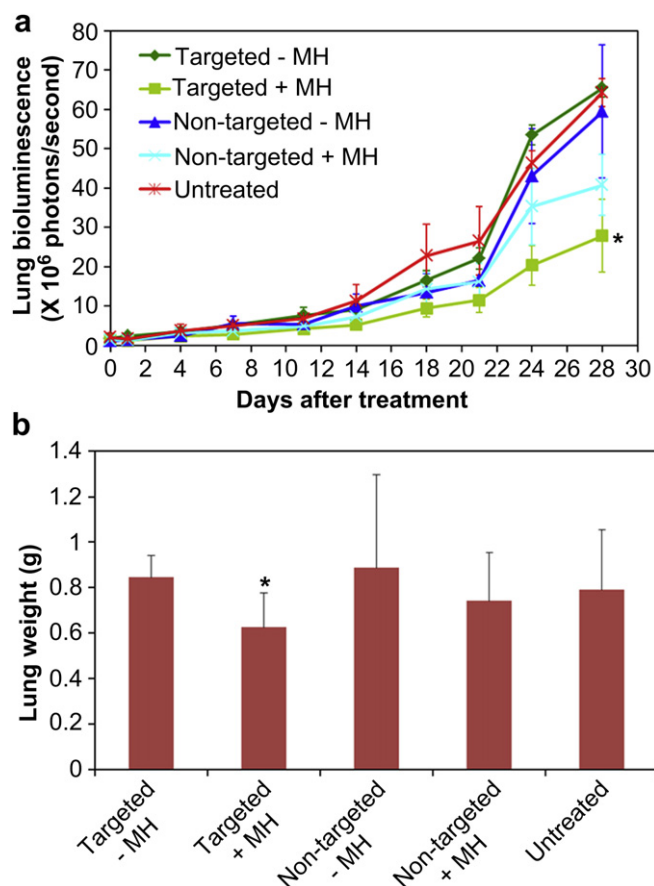


Fig. 5. Effect of targeted magnetic hyperthermia on lung tumor growth. Orthotopic lung tumor-bearing mice were allowed to inhale targeted or non-targeted SPIO nanoparticles. After 1 week, 6 animals from each group were subjected to magnetic hyperthermia (MH) for 30 min. (a) Lung tumor bioluminescence was monitored over a period of 1 month. Data shown as mean \pm SD ($n = 6$; * $P < 0.05$ compared to saline-treated and unheated controls). (b) Lungs were collected at the end of the efficacy study (1 month after magnetic hyperthermia) and weighed. Data shown as mean \pm SD ($n = 6$; * $P < 0.05$ compared to unheated control).

highly acidic gastric pH to form soluble iron salts, which are then absorbed into the blood stream. This will lead to high initial iron content in the blood. This soluble iron can be cleared from blood relatively easily, resulting in a decrease in the iron levels after a week. Second, immediately after instillation, SPIO nanoparticles in the lung are free and can be absorbed into the blood stream. However, at later time points, particles are likely internalized into the tumor cells (and/or macrophages) and hence not readily available for absorption. This would also result in high initial iron concentration in the blood, followed by a drop at later times.

Following inhalation delivery, it is expected that nanoparticles would be distributed to both the malignant and healthy regions of the lungs. The presence of targeting ligand on the surface is expected to enable nanoparticles to bind to the tumor cells, allowing for greater retention in the tumor tissue. Thus, greater retention within the tumor tissue and clearance from normal tissue are expected to eventually result in relatively higher levels of nanoparticles in the tumor. Application of AMF during this window would allow for tumor-specific induction of hyperthermia. In our studies, tumor cell specificity was achieved by targeting SPIO nanoparticles to EGFR, which is overexpressed in NSCLC tumors [11–13]. Monoclonal antibodies against EGFR (cetuximab) and EGFR tyrosine kinase inhibitors are clinically used for lung cancer. Thus, EGFR is an attractive target in lung cancer. We used a

previously reported 11-residue peptide ligand for targeting EGFR [15]. This peptide binds specifically and efficiently to EGFR (dissociation constant of ~ 20 nM), but has much lower mitogenic activity than EGF [15]. We found that EGFR targeting enhanced the *in vitro* accumulation of targeted SPIO nanoparticles into A549 cells by 450% compared to non-targeted particles. Aerosolized SPIO particles were directed to the periphery of the lung by controlling the aerodynamic size of SPIO aggregates. One hour after inhalation, the amount of the targeted or non-targeted particles was similar in tumor-bearing or healthy lungs (about 70 μ g iron oxide). However, following mucociliary clearance from the lung (1 week after inhalation delivery), the level of non-targeted SPIO nanoparticles was significantly lower than that of targeted particles. This difference could be attributed to the presence of tumor targeting ligand on the surface. Thus, by combining receptor targeting with inhalation delivery, superior tumor selectivity can be achieved.

There are several challenges in the design of an effective inhalation system, which can deposit a high dose to the peripheral regions of the lung. Mice are obligatory nose breathers, with a small inhalation volume (~ 24.5 ml/min). This restricts the rate of delivery of therapeutics into the lungs. The dose delivered can, however, be controlled by changing the concentration of the aerosol generated (mass of aerosol/volume of air) and the aerodynamic diameter of the aerosol. An MMAD of 1 μ m has been shown to result in the highest concentration of the therapeutic agents in all lobes of mouse lungs [32], yielding a deposition percent (ratio of mass deposited in the lungs to total mass inhaled) of about 10% [21,33]. In our studies, we obtained a deposition of nearly 15% with the 1.1 μ m MMAD SPIO nanoparticles. The elevated deposition fraction was probably attributed to pre-acclimatization of the mice to the inhalation chambers and the prolonged exposure (30 min), which prevented undue stress and uneven breathing pattern caused by short aerosol exposures. This fraction is amenable to further enhancement by using magnetic deposition [21] or micro-spraying technique [34], which can increase the deposition fraction of SPIO nanoparticles by several folds.

The effectiveness of targeted magnetic hyperthermia was evaluated in an orthotopic mouse lung tumor model. Intravenous injection of A549 cells led to the development of lung tumors, whose bioluminescence scaled with the size of the tumor. Lung tumors could be identified at a bioluminescence level of 1×10^5 photons/s and the tumor burden reached 90% of the lung volume at 5×10^8 photons/s. Using an optimized aerosol formulation of targeted SPIO nanoparticles, we could achieve therapeutic doses of SPIO nanoparticles in the tumors. A single magnetic hyperthermia regimen was effective in reducing the tumor growth rate over a month compared to the non-targeted or non-treated control. In addition, the treatment did not result in any toxic manifestations in the mice.

Due to their epithelial nature, lung tumors fill up the alveolar region and thus, most tumors are not exposed to the circulating airways. This poses a challenge to the success of the nanoparticle system. In spite of enhanced retention of targeted SPIO nanoparticles in the tumor, not all tumor cells possessed particles and therefore would not receive magnetic hyperthermia therapy. As a result, the treatment showed a significant delay in tumor growth but not complete eradication. However, this problem could potentially be addressed by using agents that normalize the tumor extracellular matrix and enhance the penetration of nanoparticles into the tumor [35,36]. Additionally, SPIO nanoparticle mediated magnetic hyperthermia may be highly effective as an adjuvant therapy for killing isolated tumors cells left behind after surgical resection of the lung tumors.

5. Conclusions

Inhalation delivery of EGFR-targeted SPIO nanoparticles was investigated in this study as a potential approach for lung cancer treatment. Our studies show that EGFR targeting enhances tumor retention of SPIO nanoparticles while minimizing systemic exposure. Tracheal instillation allowed for high doses of SPIO nanoparticles to be administered, however, aerosol delivery resulted in better intra-tumoral distribution. Magnetic hyperthermia using targeted SPIO nanoparticles resulted in a significant inhibition of *in vivo* tumor growth. Overall this work highlights the potential for developing magnetic hyperthermia as an effective anticancer treatment modality for the treatment of non-small cell lung cancer.

Acknowledgments

Parts of this work were carried out in the Characterization Facility, University of Minnesota, which receives partial support from NSF through the MRSEC program. We also thank the Comparative Pathology core facility for the preparation of H&E and Prussian blue stained slides.

We thank Ying Jing (Electrical and Computer Engineering, University of Minnesota) for help with magnetization studies, Paula Overn (Comparative Pathology, University of Minnesota) for the preparation of histopathology slides and Brenda Koniar (Research Animal Resources, University of Minnesota) for assistance with animal studies.

Funding support from the Department of Defense (CA093453).

Appendix. Supplementary data

Supplementary data related to this article can be found online at <http://dx.doi.org/10.1016/j.biomaterials.2013.03.061>.

References

- [1] Cancer trends progress report – 2012 update. Bethesda, MD: National Cancer Institute, NIH, DHHS; 2012.
- [2] Non-small cell lung cancer treatment (PDQ®). Available from: <http://www.cancer.gov/cancertopics/pdq/treatment/non-small-cell-lung/patient>.
- [3] Shaw EG, Brindle JS, Creagan ET, Foote RL, Trastek VF, Buskirk SJ. Locally recurrent non-small-cell lung cancer after complete surgical resection. *Mayo Clin Proc* 1992;67(12):1129–33.
- [4] Kelsey CR, Marks LB, Hollis D, Hubbs JL, Ready NE, D'Amico TA, et al. Local recurrence after surgery for early stage lung cancer: an 11-year experience with 975 patients. *Cancer* 2009;115(22):5218–27.
- [5] Thomas P, Rubinstein L. Cancer recurrence after resection: T1 N0 non-small cell lung cancer. *Lung Cancer Study Group. Ann Thorac Surg* 1990;49(2):242–6.
- [6] Hiergeist R, Andrä W, Buske N, Hergt R, Hilger I, Richter U, et al. Application of magnetite ferrofluids for hyperthermia. *J Magn Magn Mater* 1999;201(1–3):420–2.
- [7] Jordan A, Scholz R, Wust P, Föhling H, Roland F. Magnetic fluid hyperthermia (MFH): cancer treatment with AC magnetic field induced excitation of biocompatible superparamagnetic nanoparticles. *J Magn Magn Mater* 1999;201(1–3):413–9.
- [8] Tasci TO, Vargel I, Arat A, Guzel E, Korkusuz P, Atalar E. Focused RF hyperthermia using magnetic fluids. *Med Phys* 2009;36(5):1906–12.
- [9] Tseng HY, Lee GB, Lee CY, Shih YH, Lin XZ. Localised heating of tumours utilising injectable magnetic nanoparticles for hyperthermia cancer therapy. *IET Nanobiotechnol* 2009;3(2):46–54.
- [10] Jung H. Interaction of thermotolerance and thermosensitization induced in CHO cells by combined hyperthermic treatments at 40 and 43 degrees C. *Radiat Res* 1982;91(3):433–46.
- [11] Merrick DT, Kittelson J, Winterhalder R, Kotantoulas G, Ingeberg S, Keith RL, et al. Analysis of c-ErbB1/epidermal growth factor receptor and c-ErbB2/HER-2 expression in bronchial dysplasia: evaluation of potential targets for chemoprevention of lung cancer. *Clin Cancer Res* 2006;12(7 Pt 1):2281–8.
- [12] Tang X, Varella-Garcia M, Xavier AC, Massarelli E, Ozburn N, Moran C, et al. Epidermal growth factor receptor abnormalities in the pathogenesis and progression of lung adenocarcinomas. *Cancer Prev Res* 2008;1(3):192–200.
- [13] Varella-Garcia M, Mitsudomi T, Yatabe Y, Kosaka T, Nakajima E, Xavier AC, et al. EGFR and HER2 genomic gain in recurrent non-small cell lung cancer after surgery: impact on outcome to treatment with gefitinib and association with EGFR and KRAS mutations in a Japanese cohort. *J Thorac Oncol* 2009;4(3):318–25.
- [14] Chittasupho C, Xie SX, Baoum A, Yakovleva T, Siahaan TJ, Berkland CJ. ICAM-1 targeting of doxorubicin-loaded PLGA nanoparticles to lung epithelial cells. *Eur J Pharm Sci* 2009;37(2):141–50.
- [15] Li Z, Zhao R, Wu X, Sun Y, Yao M, Li J, et al. Identification and characterization of a novel peptide ligand of epidermal growth factor receptor for targeted delivery of therapeutics. *FASEB J* 2005;19(14):1978–85.
- [16] Grabarek Z, Gergely J. Zero-length crosslinking procedure with the use of active esters. *Anal Biochem* 1990;185(1):131–5.
- [17] Jain TK, Morales MA, Sahoo SK, Leslie-Pelecky DL, Labhasetwar V. Iron oxide nanoparticles for sustained delivery of anticancer agents. *Mol Pharmacol* 2005;2(3):194–205.
- [18] Krishna Murti GSR, Moharir AV, Sarma VAK. Spectrophotometric determination of iron with orthophenanthroline. *Microchem J* 1970;15(4):585–9.
- [19] Zhang G, Fandrey C, Naqwi A, Wiedmann TS. High-frequency ultrasonic atomization for drug delivery to rodent animal models – optimal particle size for lung inhalation of difluoromethyl ornithine. *Exp Lung Res* 2008;34(5):209–23.
- [20] Liao X, Liang W, Wiedmann T, Wattenberg L, Dahl A. Lung distribution of the chemopreventive agent difluoromethylornithine (DFMO) following oral and inhalation delivery. *Exp Lung Res* 2004;30(8):755–69.
- [21] Xie Y, Longest PW, Xu YH, Wang JP, Wiedmann TS. In vitro and in vivo lung deposition of coated magnetic aerosol particles. *J Pharm Sci* 2010;99(11):4658–68.
- [22] Corti C, Pratesi G, DeCesare M, Pellegrini R, Giardini R, Supino R, et al. Spontaneous lung metastases in a human lung tumor xenograft: a new experimental model. *J Cancer Res Clin Oncol* 1996;122(3):154–60.
- [23] Hastings RH, Summers-Torres D. Direct laryngoscopy in mice. *Contemp Top Lab Anim Sci* 1999;38(6):33–5.
- [24] Frank JA, Kalish H, Jordan EK, Anderson SA, Pawelczyk E, Arbab AS. Color transformation and fluorescence of Prussian blue-positive cells: implications for histologic verification of cells labeled with superparamagnetic iron oxide nanoparticles. *Mol Imaging* 2007;6(3):212–8.
- [25] Taratula O, Garbuzenko OB, Chen AM, Minko T. Innovative strategy for treatment of lung cancer: targeted nanotechnology-based inhalation co-delivery of anticancer drugs and siRNA. *J Drug Target* 2011;19(10):900–14.
- [26] Drazen JM, Finn PW, De Sanctis GT. Mouse models of airway responsiveness: physiological basis of observed outcomes and analysis of selected examples using these outcome indicators. *Annu Rev Physiol* 1999;61:593–625.
- [27] Chen C, Hayek S, Mohite V, Yuan H, Chatterjee J, Haik Y. Nanomagnetism and magnetic hyperthermia. In: Nalwa HS, Webster T, editors. *Cancer nanotechnology: nanomaterials for cancer diagnosis and therapy*. San Diego, CA: American Scientific; 2007. p. 160–91.
- [28] Hu R, Ma S, Li H, Ke X, Wang G, Wei D, et al. Effect of magnetic fluid hyperthermia on lung cancer nodules in a murine model. *Oncol Lett* 2011;2(6):1161–4.
- [29] Hu R, Zhang X, Liu X, Xu B, Yang H, Xia Q, et al. Higher temperature improves the efficacy of magnetic fluid hyperthermia for Lewis lung cancer in a mouse model. *Thorac Cancer* 2012;3(1):34–9.
- [30] Jaracz S, Chen J, Kuznetsova LV, Ojima I. Recent advances in tumor-targeting anticancer drug conjugates. *Bioorg Med Chem* 2005;13(17):5043–54.
- [31] Garbuzenko OB, Saad M, Betigeri S, Zhang M, Vetcher AA, Soldatenkov VA, et al. Intratracheal versus intravenous liposomal delivery of siRNA, antisense oligonucleotides and anticancer drug. *Pharm Res* 2009;26(2):382–94.
- [32] Yi D, Naqwi A, Panoskaltis-Mortari A, Wiedmann TS. Distribution of aerosols in mouse lobes by fluorescent imaging. *Int J Pharm* 2012;426(1–2):108–15.
- [33] Raabe OG, Al-Bayati MA, Teague SV, Rasolt A. Regional deposition of inhaled monodisperse coarse and fine aerosol particles in small laboratory animals. *Ann Occup Hyg* 1988;32:53–63.
- [34] Beck SE, Laube BL, Barberena CI, Fischer AC, Adams RJ, Chesnut K, et al. Deposition and expression of aerosolized rAAV vectors in the lungs of *Rhesus macaques*. *Mol Ther* 2002;6(4):546–54.
- [35] Brown E, McKee T, diTomasso E, Pluen A, Seed B, Boucher Y, et al. Dynamic imaging of collagen and its modulation in tumors in vivo using second-harmonic generation. *Nat Med* 2003;9(6):796–800.
- [36] Eikenes L, Bruland ØS, Brekken C, Davies CDL. Collagenase increases the transcapillary pressure gradient and improves the uptake and distribution of monoclonal antibodies in human osteosarcoma xenografts. *Cancer Res* 2004;64(14):4768–73.

Image-guided drug delivery in lung cancer

Timothy S. Wiedmann · Tanmoy Sadhukha ·
Bruce E. Hammer · Jayanth Panyam

Published online: 11 January 2012
© Controlled Release Society 2012

Abstract Lung cancer continues to be the number one cause of cancer-related deaths in the USA. Early identification of the disease, availability of more effective drugs, and improved delivery of such drugs specifically to cancer cells are needed to decrease lung cancer-associated morbidity and mortality. The concept of image-guided drug delivery (IGDD), which envisions the utilization of imaging techniques for quantitative assessments of tumor-targeted drug delivery and therapeutic response, has the potential to make a significant impact in lung cancer. While the anatomic and physiological features of the lung pose distinct problems for imaging drug delivery, several new techniques are emerging that have the potential to overcome these problems. X-ray is a routinely used technique for diagnosing lung cancer; however, positron emission tomography (PET) and magnetic resonance imaging (MRI) are complementary approaches. PET- and MRI-based techniques (such as functional MRI) offer the possibility of imaging the delivery of specific molecules to cancer tissues in the lung. This paper reviews fundamentals of imaging with an emphasis on MRI and to some extent PET, since it will be argued that these

techniques are the most promising for development in IGDD for lung cancer. Finally, key literature contributions will be highlighted, which exemplify the current successes in this area.

Keywords X-ray · Computed tomography · Magnetic resonance imaging · Positron emission tomography · Targeted drug delivery · Diagnosis

Introduction

Several imaging and drug delivery technologies are emerging that collectively have the potential to radically change the prognosis of lung cancer. These technologies pertain to the concept of image-guided drug delivery (IGDD). As described by Dr. Farahani (Cancer Imaging Program, National Cancer Institute), IGDD in cancer is a “personalized therapy where imaging techniques can be utilized in quantitative assessments of tumor-targeted therapeutic delivery, distribution, uptake, and response” [1]. Personalized therapy is an ambitious vision of the future, and the current cancer treatments represent the initial steps towards its achievement.

Personalized therapy is perhaps most important in the area of lung cancer because (1) it is the most lethal cancer in men and women, (2) little progress has been made in last five decades in improving the prognosis despite intense basic, applied, and clinical research, and (3) it embodies a diverse myriad of phenotypical and genotypical tumors that span a wide range of stages and states of progression. It may well be that the lack of appreciation for the need of a personalized approach has contributed to the dismal progress in lung cancer treatment outcomes. This is likely to happen when clinical studies inappropriately group patients into common phenotypical categories, when in fact these

T. S. Wiedmann · T. Sadhukha · J. Panyam (✉)
Department of Pharmaceutics, College of Pharmacy,
University of Minnesota,
308 Harvard Street SE,
Minneapolis, MN 55455, USA
e-mail: jpanyam@umn.edu

B. E. Hammer
Center for Magnetic Resonance Research and Department of
Radiology, Medical School, University of Minnesota,
Minneapolis, MN 55455, USA

J. Panyam
Masonic Cancer Center,
Minneapolis, MN 55455, USA

actually were genetically distinct diseases that do not have a common approach for therapeutic success.

Returning to Dr Farahani's description, IGDD is perhaps more of a drug delivery evaluation rather than drug delivery guidance. Thus, the concept of guidance in this definition suggests diagnosis and then evaluation of disease progression and/or treatment, from which the treatment approach can be modulated. Thus, guidance becomes merely a more sophisticated form of patient/disease evaluation. For example, if a tumor is shrunk, treatment was successful, but if it continues to grow, alternatives must be sought. While such information is highly valuable, there is no active or real-time guidance to localize the drug in a specific location.

The full implementation of IGDD has been suggested to require (a) drugs that can be imaged, localized, or targeted, and activated at the tumor site and (b) imaging techniques that provide anatomic and quantitative functional measures of the process at various spatial and temporal resolutions for active monitoring. The term localization suggests a purposeful directing of the drug to the site of action. In field of drug delivery, "targeting" involves attaching a ligand with affinity for a receptor ideally expressed exclusively on the cancerous cell. Thus, targeting may enhance drug accumulation at the target site, but may not result in significantly decreased drug accumulation elsewhere. It is possible to increase the drug exposure in the target tissue 5-fold (say from 1% of injected dose to 5% of injected dose), but this may only minimally reduce the drug exposure in non-target tissues (99% to only 95% of the injected dose, in this case). In the military parlance, the above approach would be similar to using a targeted missile system that would blanket an entire country with explosives, with the target sites suffering more damage than others. Extending the analogy to IGDD, a missile guidance system would not actually direct the armament to the desired site but would merely provide images of the wide swaths of destruction wrought on intended and unintended areas. Unlike targeted missile systems, truly specific targeted delivery systems are, unfortunately, not available yet.

Nevertheless, despite this inherent shortcoming, image guidance could play an important role in improving lung cancer outcomes. For this purpose, the imaging system must minimally provide information pertaining to the anatomical structures as well as to the drug delivery system. For the anatomical structures, the imaging technique must discriminate between normal and diseased areas. Ideally, this should be done at the levels of organ, tissue, cell, organelle, and ultimately to the molecular level, since the latter is needed to evaluate drug interaction at the active site. There is a corresponding requirement for detection of the drug at these same levels. It is noteworthy that the active chemical entity must be followed and not the surrogate components of delivery system that carries the label.

In the following section, background information pertaining to lung cancer is provided. This is the sine qua non of choosing and adopting sophisticated imaging and therapeutic approaches. The subsequent section will review fundamentals of imaging with an emphasis on MRI and to some extent PET, since it will be argued that these techniques are the most promising for development in IGDD for lung cancer. Finally, key literature contributions will be highlighted, which exemplify the current successes in this area.

Characteristics of lung cancer

Lung cancer is the number one cause of cancer-related deaths in both men and women in the USA and in many countries worldwide. The American Cancer Society provides alarming statistics for the year 2011, in which there were 221,130 new cases and 156,940 estimated deaths [2, 3]. Future incidence/death may be reliably predicted based on current smoking rates due to the well-established correlation between cigarette smoking and lung cancer [4]. Although smoking rates are declining in most Western countries, the incidence is steady or even rising in other areas of the world. In China, for example, it is estimated that nearly 60% of the adult male population smoke [5]. Thus, the epidemic of lung cancer deaths will likely continue.

The major types of lung cancer are based on the morphological code of the International Classification of Diseases for Oncology and the Systematized Nomenclature of Medicine [6]. The World Health Organization (WHO) created a standard nomenclature for lung cancer: In the category of malignant epithelial carcinoma, there is squamous cell carcinoma, small cell carcinoma, adenocarcinoma, large cell carcinoma, adenosquamous carcinoma, sarcomatoid carcinoma, carcinoid tumor, and salivary gland tumors [7].

In the interest of localization of therapy, it is significant that there is a correlation between the type of cancer and the area of the lung it is found. In the alveoli region, adenocarcinoma is the most frequent and represents about 30% of the primary lung malignancies. Bronchiolalveolar carcinoma and atypical adenomatous hyperplasia are also largely found in the terminal bronchioles and lung periphery. Tumors that occur primarily in the central bronchi include squamous carcinoma (29% of all lower respiratory tract cancer), large cell carcinoma (9%), and small cell lung carcinoma (10–15%). For the purposes of treatment, lung cancer is characterized as being either small cell lung cancer (SCLC) or non-small cell lung cancer (NSCLC) [8]. The severity of NSCLC is determined by the TNM system based on the tumor size (T), lymph node involvement (N), and presence of metastasis (M) [7]. In contrast, SCLC is characterized as being either a limited or extensive disease.

For diagnosis, X-ray is the standard imaging methodology for detecting and characterizing tumors in the lung. For treatment, the current Revised Response Evaluation Criteria in Solid Tumors guideline relies on objective disease progression (tumor shrinkage determined using X-ray [9]. Because X-ray imaging arises from differences in electron density, diagnosis of the type of cancer requires microscopic evaluation of a tissue sample. It should be noted that X-ray imaging carries a high false positive rate, since many individuals have X-ray opaque structures in their lungs that are not malignant. For radiographs identified as suspicious for cancer in the National Cancer Institute studies, the positive predictive value ranged from 41% to 60% [10]. A previous review provides extensive data on false positive rates associated with chest radiography and how this compares with more advanced diagnostic techniques [11]. It is noted that most abnormalities on chest radiography are resolved, or screening results are found to be false positive when evaluated by CT [12]. A recent retrospective study of 11,766 MRI scans revealed that 559 (4.8%) had suspicious lung nodules, but only 49 (0.4%) had primary lung cancer diagnoses [13]. For identification of the type, classification, and location of the cancer, the current decision-tree for therapeutic intervention is available through the National Comprehensive Cancer Network [8].

Presently, large or singular tumor masses are surgically removed whenever possible, which may involve removal of an entire lung (pneumonectomy), one or more lobes (lobectomy), or parts of a lobe (wedge and segment resection) if affected with very small tumors. Macroscopically, surgery is a true form of image-guided therapy, where obviously cancerous cells are removed and healthy tissue is preserved. It also can provide a gateway to IGDD with drug administration at the site by a spray device or implant [14]. It is likely that surgery will remain the treatment of choice for all operable tumors, which present as a large, discrete mass that can be safely removed without damaging critical blood vessels or nerves. Chemotherapy, even as IGDD, will remain relegated to a secondary option. Nevertheless, surgical oncologists will likely be the first to concede the limitations and relatively poor long-term outcome of surgery for lung cancer patients. Specifically, the 5-year survival is at 41% and 23% for stage I and II NSCLC, respectively [7, 15]. The survival for stage III is much lower.

In addition to poor prognosis, lung cancer patients have a number of attributes that further press the need for directed/guided therapy. The first factor is that patients with lung cancer tend to be elderly with a median age of first diagnosis near 70 years [16, 17]. Patients that develop lung cancer typically have had a long history of cigarette smoking and are generally not in good health. Life expectancy may not be long under normal conditions and is even shorter for those individuals in poor health. Non-specific chemotherapy,

which carries the high risk of debilitating side effects, is a poor choice. Another factor is that surgery may not remove all cancerous cells [7, 18]. For this reason, chemotherapy and radiation are often used in conjunction with surgery. In fact, adjuvant therapy (chemotherapy following surgery) is the standard of care for those patients with stage II and III NSCLC [15, 19]. Neoadjuvant therapy (chemotherapy before surgery) is also being actively studied.

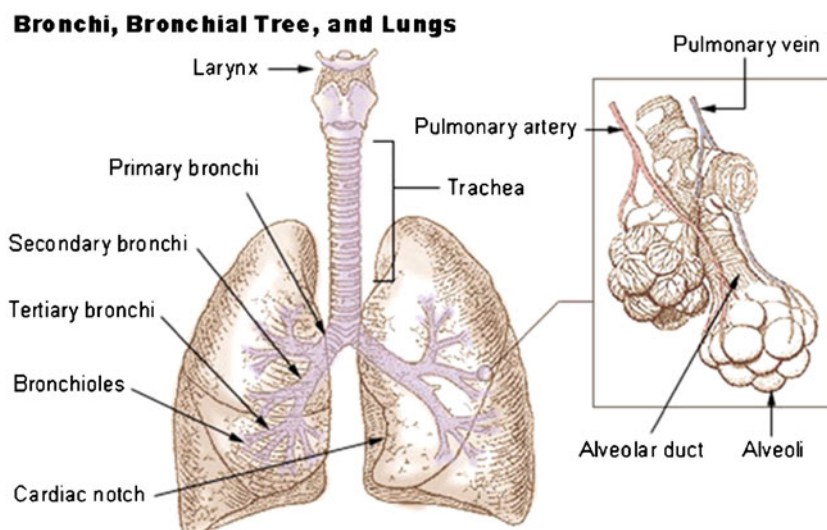
Related to the second factor is that the remaining lung cells, while apparently normal based on phenotype, may not be genetically normal. If cancer entails a cascade failure of multiple protective mechanisms that are present to prevent uncontrolled cell division and propagation [6, 18, 20], then it could be expected that many of the phenotypically normal cells (around the lesion) possess genetic defects. The premise can be conceptualized with the simplistic idea that cancer development requires an initiation and a propagation step. Thus, while patients with lung cancer have had regions of the lung undergo these development steps resulting in cancer, the remaining apparently normal cells may be poised to undergo a propagation step, which if it occurs, would be interpreted as a recurrence of lung cancer. This is well recognized and is referred to as the field effect, where an area of cancer is composed of cells spanning a range of genetic expression and phenotypes [21, 22].

Finally, because lung cancer often develops largely asymptotically, the majority of patients are first diagnosed in stage III or IV, which involves invasion of the cancer into surrounding tissues or metastasis. Thus, the quoted 5-year survival rate is near 15% for all lung cancer patients. As such, there is benefit of using imaging methodology to not only detect the common occurrence of metastasis but also provide for guidance of the effectiveness of drug therapy.

Lung biology relevant to imaging

Before introducing techniques for imaging and delineating the strengths and weaknesses as applied to the lung, it is important to have an appreciation of the respiratory tract. The respiratory tract is considered to have two anatomical regions (upper and lower). The lower respiratory tract includes the trachea, bronchi, bronchioles, and alveoli. The trachea and bronchi make up the conducting airways, which, as the names implies, primarily function as a passageway from the external environment to the site of gas exchange. In these conduits, particulate matter is efficiently removed, and the cross-sectional area geometrically increases. The small bronchioles and alveoli make up the pulmonary region of the respiratory tract, which provide the site for gas exchange (Fig. 1).

Fig. 1 Schematic of the lungs showing the branching pattern of conducting airways, which end in alveoli. Reproduced under the terms of the GNU Free Documentation License from Wikibooks (http://en.wikibooks.org/wiki/Human_Physiology/The_respiratory_system)



The trachea follows the larynx as air moves into the lung. After the trachea, the bronchi are encountered. There is a right and a left bronchi resulting from a division; the first is within the lung, which is repeated until the alveolar ducts are reached. This gives rise to a complex branching pattern. Coupled with this geometry is the need to package the lung within a minimum volume. Although there are five distinct lobes in the human lungs, larger diameter airways may be physically quite close to alveoli. Thus, except for the very periphery of the lung, all two-dimensional projections of the lung will contain both large and small airways.

At the microscopic level, the surface of the conducting airways is lined with the mucociliary system from the nasal cavity throughout the entire conducting region of the lung. This system is a consequence of the activity of primarily two cell types: the goblet cells, which secrete mucus, and the ciliated pseudostratified columnar cells, which transport the mucus towards the trachea. Mucus is a hydrated, glycoprotein network with significant cross-linking among the mucin chains. In the pulmonary region of the lung, the terminal bronchioles lead to the alveolar ducts that have attached alveolar sacs. The alveolar sacs are about 0.03 cm in diameter, and at their air/liquid interface, there exists a mixture of lipids with several associated proteins that is known as lung surfactant. The type II cell is largely responsible for secretion and recycling of lung surfactant, but the type I epithelial cell is more prevalent. Although only four cell types have been mentioned here, it should be appreciated that the lung contains over 40 different cell types. Thus, there is complexity at the macroscopic level as well as at the level of the cell and cell lining within the lung.

At the molecular level, great effort is being expended to characterize the expression of surface receptors on different cell types. It can be anticipated that as with the variety of cells, surface receptor expression will be equally, if not more, complex. In addition, the asymmetry of the cells must

not be forgotten. That is, many of the cells within the lung have an apical surface exposed to air or fluid in the alveoli as well as a basolateral surface that is in contact with interstitial fluid. This is in contrast to most lung tumors that are present as nodules, which may or may not be vascularized but usually have a minimal surface exposed to air.

As an organ, the dispersion of air-filled alveoli with a diameter not much larger than the limit of human vision, separated by tissue sheets that are much thinner than discerned by eye, represents a profound challenge for all imaging techniques. That is, the tissue is highly heterogeneous, but yet near microscopic limit is needed for visual resolution. Because of the presence of air, the weight of the lungs is quite small, representing perhaps only 2% of the body weight, yet the low-density organ represents a large volume, which is the significant measure for a visual image. Finally, the lungs are contained within the protective bony/cartilaginous structure of the ribs/sternum. A uniform shell encasing the lungs would present a more convenient obstacle than the irregular shaped ribs that vary with respect to length, diameter, and density.

Another major complication arising with the lung is that it must remain active during image acquisition. Lungs undergo cyclic changes of expansion and contraction during respiration. The cyclic change would be less of a challenge if it were not for the irregularity of the physical displacement especially in the context of required spatial resolution. Thus, if there is interest in distinguishing two adjacent alveoli by imaging, the lung must be repositioned to within 0.03 cm, or alternatively, the image acquisition must be sufficiently rapid to take place during a realistic breath-holding period. This latter point will be valid for lung structures that presumably remain constant, but becomes invalid in assessing the time dependent distribution of drug delivery systems.

Finally, the lung is well perfused with blood, essentially receiving the entire cardiac output. From the perspective of

treating lung cancer, blood contained within blood vessels should be distinguished from lung tissue and lung fluids. The heart's rhythmic beating, along with arterial oscillations, induces movement that is propagated throughout the lungs. Again, problems of resolution become a significant issue.

Imaging and lung cancer

Many imaging techniques are available for providing information about the lung, normal and diseased, as well as the drug delivery system. As noted before, diagnosis of lung cancer critically depends on combined methodologies, and such multiple techniques are also used to evaluate treatment. In all considerations of imaging, contrast, sensitivity, and dynamic range are key issues along with the question of spatial and temporal resolution [23]. For each method, the final image is presented as a two-dimensional picture composed of pixels, each of which can be assigned a numeric value corresponding to the signal strength. The two-dimensional images can be assembled in a stack (often called a z-stack) to reconstruct a three-dimensional image. Historically, the eye served as the qualitative interpreter of the signal strength, but with the explosive advance in computational methods, the numeric value can provide quantitative information. For quantification, the value assigned to a given pixel is derived from the underlying physics of the imaging technique, which is the primary determinant of the contrast. Each image, which is composed of pixels with a range of intensities, is shaped by transparency/opacity of specific structures to the applied form of energy. In principle and almost practically, the entire electromagnetic spectrum can be used for imaging, including the oldest method, visible light, as well as UV, IR, X-rays, and radio frequency. Neutrons, positrons, and gamma and beta particles may also be used. Finally, energy in the form of mechanical waves is used as in ultrasound. For all approaches that do not use visible light, the energy detected from the specimen must be converted to the visible spectrum.

X-ray [chest radiography and computed tomography (CT)], gamma scintigraphy (single photon emission CT), positron emission tomography (PET), magnetic resonance imaging (MRI) and its complement, magnetic resonance spectroscopy (MRS) are the principle techniques available for lung imaging. While not dismissing other imaging techniques, e.g., electrical impedance tomography, microwave imaging, etc., as impossible, there are significant theoretical and/or technical problems that preclude their use.

With human lung cancer, conventional chest X-ray radiography is the most common method of screening for tumors within the lung. Tumor presence can be ascertained by direct visualization of a mass within the air cavity or

inferred by chest wall expansion or bone degradation of adjacent ribs or vertebrae. X-ray CT is the standard modality for staging lung cancer. CT can non-invasively determine the resectability of a lesion depending on tumor location, size, and proximity to critical blood vessels or the mediastinum. Gamma scintigraphy represents the standard for characterizing the delivery of labeled drug to the lung. PET is exquisitely sensitive for quantitative molecular imaging and staging of tumors within the lung. In principle, MRI can provide anatomical and chemical information, but the technique is inherently more complicated, and as such, the development has lagged. While anatomical alterations are extremely important for diagnostic purposes, there is much greater interest currently in developing imaging methodology that reflects function [24].

The development of X-ray imaging for lung cancer, now in its current form of computed tomography, which provides reconstructed three-dimensional images, is an obvious consequence of the contrast between a normally low electron dense tissue/air space and a high electron dense tumor. The obstructions arising from bones can be cleverly circumvented. This is also true for gamma scintigraphy that relies on the presence of gamma emitting molecules (commonly ^{99m}Tc) from an essentially negligible background. For both of these techniques, the inherent contrast and sensitivity is high, which in turn allows for either rapid signal acquisition (for high temporal resolution) or long-term signal accumulation (for high spatial resolution). The high contrast and the direct collection of the X-ray or gamma rays also lead to a direct path for quantification. The drawback for these techniques is the requirement of ionizing radiation and the associated concerns of adverse health effects, especially with repeated use.

PET imaging yields spatial metabolic information but does not show anatomical detail. To acquire a PET image, a ligand that seeks a specific cellular target must be labeled with a positron-emitting isotope such as ^{18}F , ^{11}C , ^{15}O , or ^{13}N . For example, when ^{18}F -fluorodeoxy glucose (FDG) is injected into a subject, ^{18}F -FDG will concentrate in tissues that have the greatest metabolic activity, such as brain and heart, and will eventually label the bladder as the isotope is cleared from the body. When rapidly dividing cells are present, such as in cancerous tissue, the uptake of ^{18}F -FDG is typically far greater than that of surrounding tissue. Production of positron emitters requires a cyclotron that bombards a target with a high-energy proton beam that can be up to 20 MeV. These isotopes have a short half-life and thus utilize special radiochemical methodologies to rapidly and appropriately label a ligand. The half-life of ^{18}F is 110 min, ^{11}C is 20 min, ^{15}O is 2 min, and ^{13}N is 10 min. Utilizing isotopes other than ^{18}F requires a cyclotron to be physically close to the scanner. PET scanners that exclusively utilize ^{18}F -labeled ligands have a 12–18-h window to

receive these compounds; thus, a cyclotron can be far from the scanner—assuming the compound can be shipped quickly to the clinic.

When imaging a ligand with a positron label, one detects gamma rays, as a consequence of positron annihilation, rather than the positron itself. When a positron-emitting radionuclide decays, the positron travels several millimeters through tissue before it encounters an electron. The positron and electron form a metastable positronium atom before they annihilate each other, creating a pair of 511 KeV photons that travel 180° from each other. A positron scanner has a ring of thousands of 10×10×10 mm cerium-doped lutetium oxyorthosilicate or bismuth germinate scintillation crystals, interfaced to photomultiplier tubes that surround a patient. When an annihilation event occurs, two detectors, 180° apart, will detect the event within a timing window of several hundred nanoseconds. Thus, it is known that an annihilation occurred somewhere along the line of sight between the two detectors. The PET scanner takes this information from thousands of detectors and events to produce an image of radioisotope distribution within the scanner (Fig. 2).

¹⁸F-FDG is the most routinely used radiolabeled compound for PET imaging [25, 26]. Cells experiencing high glycolytic activities phosphorylate FDG. Once phosphorylated, FDG cannot be metabolized any further, thus effectively trapping the radioisotope in the cell. After ¹⁸F-FDG decays via positron emission, the 2'-fluorine is converted to ¹⁸O, which becomes protonated by hydronium ions in the cytoplasm and is normally metabolized via the glycolytic pathway. Another common radiolabeled compound used is ¹⁸F-FHBG (9-4-[¹⁸F]fluoro-3-(hydroxymethyl)butyl]guanine, which is a reporter probe that images the expression of the herpes simplex virus type-1 thymidine kinase (HSV1-tk) gene in gene transfer therapy. HSV1-tk and HSV1-tk-metabolized ¹⁸F-FHBG co-localize, allowing PET-based localization of HSV1-tk

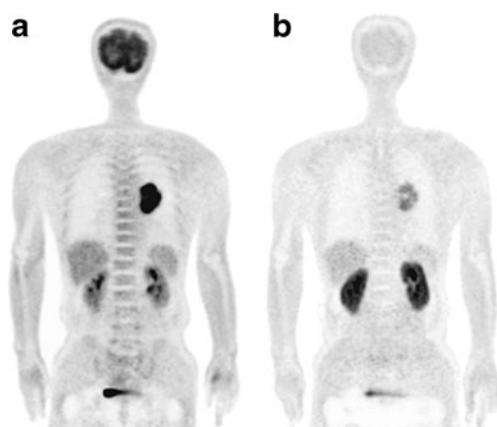


Fig. 2 PET images of 62-year-old man with adenocarcinoma of left lung (p-T2N0M0). Both ¹⁸F-FDG (a) and ¹⁸F-FMT (b) showed increased uptake in primary tumor. Reproduced from [57]

gene-transfected tissue and the assessment of gene transfer efficiency [27]. Another ligand that acts as a PET reporter molecule is fluorothymidine (¹⁸F-FLT). FLT is a pyrimidine analogue and is incorporated in tumors having a rapid DNA synthesis and cell proliferation [28–30].

Despite its slow development, MRI has been shown to provide equivalent information as X-ray and PET in select applications (Fig. 3) [31]. It was recently suggested that “MRI is well established as the single most useful imaging modality available in radiological practice, especially for the detection and characterization of soft tissue pathologies, such as solid tumors in cancer” [24]. However, it is the inherent potential of the technique that gives rise to optimistic view of its future use, particularly in the area of lung cancer.

With MRI, there is no direct detection of a particle; rather it is the relative concentration of magnetic nuclei and their respective relaxation behavior that give rise to the signal and, thereby, the contrast. Only nuclei that have a net magnetic moment, i.e., nuclear spin, are able to align in a magnetic field, setting the stage for signal detection. Magnetic resonance is inherently quantum-mechanical-based phenomena; however, the interaction of spins with a magnetic field and their subsequent detection is aptly described through classical physics [32]. When a nucleus of spin 1/2, such as ¹H of water or fat molecules, is placed in a time invariant magnetic field (B_0), the z-component of the nuclear magnetic moment can align parallel or antiparallel to B_0 . A slight excess of spins orient parallel to the magnetic field and thus creates a net magnetization within the sample. The

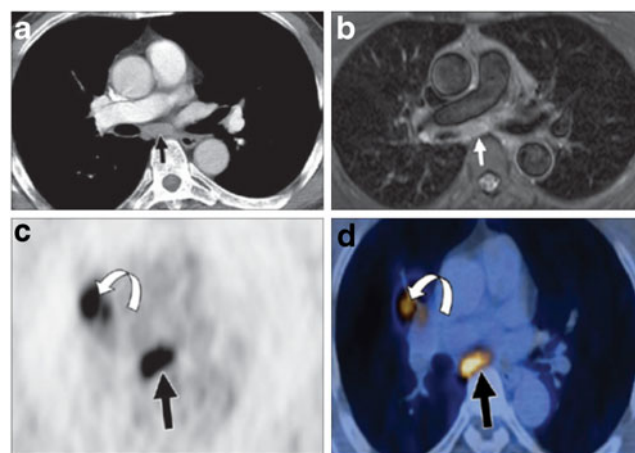


Fig. 3 X-ray CT of stage T₂ adenocarcinoma at level of bronchus intermedius. Arrow shows tumor location. Slice thickness=5 mm. **b** T₂-weighted MR image at same location as X-ray CT image. Arrow shows tumor location. **c** ¹⁸F-FDG PET image of same anatomical location. Tumors (colored black) stand out because of higher uptake of ¹⁸F-FDG. Note the lack of anatomical information. **d** PET image superimposed on CT image showing anatomical landmarks. Reproduced from [31]

exact number of spins “parallel” or “anti-parallel” to the external magnetic field can be calculated from the Boltzmann equation. Because nuclear spins have angular momentum and are oriented at an angle with respect to the applied magnetic field, they precess about B_0 at the Larmor frequency, which ranges from 2 kHz at earth’s magnetic field to 64 MHz for a typical 1.5 T clinical scanner. An MR signal is generated when the spins are tipped from their equilibrium position into the transverse plane by radiofrequency (RF) excitation that is perpendicular to B_0 . The RF is typically engaged for microseconds to milliseconds, at the Larmor frequency. Once spins are in the transverse plane, a time-varying voltage is typically sensed by the same coil that tipped the net magnetization into the transverse plane. Spins in the transverse plane gradually lose phase coherence leading to an observed exponential decay of the magnetization, known as spin–spin (T_2) relaxation. This coherent motion is lost with time at a rate proportional to $1/T_2$. Simultaneously, spins return to their equilibrium position by a process known as spin–lattice (T_1) relaxation.

T_1 relaxation behavior is perhaps conceptually easier to grasp. Placement of nuclei in a magnetic field will induce a preferential alignment of the magnetic moments in the direction of the applied field. This distribution can be perturbed by the application of a secondary field, provided the energy can be absorbed by the nuclei according to the quantum mechanical selection rules, often just stated as being in resonance or at the Larmor precessional frequency. With absorption of the energy, the equilibrium distribution is altered. Following removal of the field, the distribution of nuclei will return to the original, equilibrium state provided the energy can be released to the environment (i.e., lattice). The rate at which this energy is returned to the environment is proportional to $1/T_1$, which may be relatively long, milliseconds to seconds, since the energy loss must again follow selection rules. It is T_1 and T_2 spin relaxation that imparts tissue contrast in MR images.

The abundance of protons (^1H) and their relatively large magnetic moment has led to extensive use of MRI based on the detection of these nuclei. With unlimited sensitivity, detection of structure at levels of organ, tissue, cell, and molecule can be obtained. Moreover, this structure may pertain to anatomy as indicated, but is equally appropriate to drugs and delivery systems. There are, of course, other magnetic nuclei (^2H , ^{13}C , ^{15}N , ^{19}F , ^{17}O , ^{31}P , and ^{23}Na), which can be exploited for detection. However, because of low molar abundance and small magnetic moments, the sensitivity is too low for many imaging applications.

The spatial resolution arises from the sensitivity of the relaxation behavior to the magnetic field strength and the ability to impose magnetic fields, whose strength varies with distance, that is, a magnetic field gradient. In other words, the applied magnetic field varies with respect to the

coordinate position, which in turn affects the relaxation behavior, and thereby allows images to be acquired in a series of two-dimensional planes or a three-dimensional volume that provides the spatial selectivity.

In its simplest form, contrast between two regions of space can be achieved if the protons in one region collectively lose magnetization or coherence more rapidly than those in the other region. It can also be appreciated that the contrast may be modulated if there is a greater difference between the T_1 relaxation (i.e., T_1 weighted) or T_2 relaxation (T_2 weighted) of these two regions of space. Finally, the addition of molecules that increase the rate of relaxation of one region of space (e.g., MRI contrast agents) can be used to enhance the difference of the observed signal. Contrast agents are typically paramagnetic ions, e.g., gadolinium salts, and ferromagnetic ions such as Fe_3O_4 , or Fe_2O_3 , which increase the rate of relaxation but also introduce another path for the loss of magnetization and/or coherence [33].

The well-known effect of paramagnetic ions on proton relaxation has now opened the door to the field of functional MRI (fMRI). As an example, hemoglobin can carry either oxygen or carbon dioxide, but the oxygenated form is much more effective in accelerating relaxation of surrounding protons [24]. Thus, it becomes possible to differentiate between oxygen-rich blood in arteries and oxygen-poor blood in veins. Moreover, brain function/activity as it relates to oxygen consumption can be ascribed to specific areas in a brain image. There is a difference in relaxation behavior based on the oxygen consumption, primarily explored to identify areas of the brain that are active during specific stimuli [24].

In describing the spatial localization, it was noted that a magnetic field gradient is applied, which allowed protons within a geometrically defined voxel to be imaged. However, if, in the time frame of the measurement, the proton should move to the adjacent voxel, its signal would be lost. It then follows that with greater movement of protons, a proportionately larger signal will be lost. It has long been appreciated that diffusion affects the spin–spin relaxation rate (T_2^*), from which analytical methods were developed to measure diffusion coefficients in NMR spectrometers [24]. More recently, the difference in diffusivity, or more generally physical displacement, has been combined with MRI, which now provides another means to achieve a functional contrast in a specimen based on either flow rate or diffusion.

Another type of functional imaging, referred to as dynamic contrast enhancement (DCE) MRI, is being actively pursued [24]. In this approach, a series of images are acquired over time, including before, during, and after injection of a contrast agent. The image intensity will be affected by the concentration of contrast agent, and so by following

the time course of these changes, information pertaining to the tissue perfusion, microvascular vessel wall permeability, and extracellular volume fraction can be inferred with the appropriate mathematical (pharmacokinetic) analysis. Presently, the permeability-area product (K^{trans} in the MRI field, but recognized as a clearance in pharmacokinetics) can be related to tissue status. Using this information, normal tissue as well as benign and malignant tumors may be empirically differentiated [24]. This may also be applied to evaluate tumor response to treatment.

Finally, it was noted that the energy of the RF pulse will be absorbed by the protons, provided the transfer follows selection rules. The magnitude of energy that is absorbed depends on the static magnetic field. The field can be manipulated in such a way to promote or inhibit transfer of energy from one set of molecules to another. Thus, yet another method of inducing contrast is available that depends on the rate of magnetization transfer [24].

Overall, there is a rich array of MRI-based methods that provide a means to achieve contrast based on proton concentration and relaxation properties, either inherent or induced by contrast agents. The main challenge is sensitivity. In addition, since the image intensity is indirectly derived from time-dependent decay processes, quantification is virtually impossible. Also, the impressive spatial resolution can at times be deceptive, since it was achieved in two dimensions at the expense of very low resolution in the third dimension [33]. Put another way, the voxel is not cubical, but is a rectangular pyramid with two very small dimensions and one very large dimension.

Another issue arising from the complex set of interactions that determine signal intensity is correct attribution of signal changes. As a starting point, a voxel containing a high concentration of protons that relax slowly will give rise to a bright image if the time between subsequent spin excitations is long relative to T_1 . If the time between spin excitations is short, the spins will not have time to repopulate their respective energy levels, thus resulting in a low intensity pixel. The signal can be degraded by loss of protons or enhancing the spin–spin (T_2) relaxation rate. It is desirable to attribute this change to a specific anatomical or functional alteration. However, for a given experiment (pulse sequence), it may not be possible to unequivocally attribute the loss of signal to the specified change. Thus, a tumor nodule may appear bright, and after treatment, image intensity is reduced. This can be interpreted as tumor regression, but there may be other reasons for the loss of signal.

Much of the development of MRI has been in brain tumors [24], largely due to the boney encasement by the skull and the presence of the blood brain barrier, precluding the use of other imaging methods. The brain also has well-defined fluid- and lipid-rich regions, both of which have high proton concentrations but yet very distinctive

relaxation behaviors. In this respect, the lung poses a challenge due to the low proton concentration. The tumors possess a high proton concentration, and therefore, a positive image against a dark background of the lung tissue can be obtained, which is intrinsically valuable for imaging. However, it does pose a problem for application of positive (paramagnetic) contrast agents. The use of ferromagnetic-based contrast agents, i.e., negative contrast agents, results in making the target darker because T_2 is quite short for iron. Use of a ferromagnetic agent in the lung would result in a completely dark image, since the background is devoid of protons. In principle, two images may be compared, say before and after injection of a contrast agent, but it is difficult to directly compare images taken at different times. This challenge has been met by the development of techniques, principally specialized pulse sequences, such as sweep imaging with fourier transformation (SWIFT) that can provide a positive (i.e., bright image) in the presence of ferromagnetic contrast agents [34].

For MRI sensitivity in characterizing structure, the importance of concentration of nuclei is perhaps straightforward to understand. In the context of the lung, about two thirds of the tissue mass is water, which is present at a concentration of 110 M in protons. This can be contrasted to air space, which contains water at a concentration derived from the saturation vapor pressure at 37°C or 2.8×10^{-6} M. This presupposes that there exists a 1-mm³ voxel containing pure water that can be imaged. This may be true of the larger airways, but as noted above, the alveoli have a diameter of 0.03 mm, which seems to be well within the capability of MRI spatial resolution, e.g., 10 $\mu\text{m}/\text{pixel}$; however, respiratory motion does not allow one to obtain this resolution. In actuality, the periphery of the lung will give rise to little or no signal, as there are simply not enough protons for detection. However, as with X-ray, the presence of a cancerous nodule that does not contain air will meet the criteria for imaging by MRI and can be made to appear bright against the dark background arising from normal lung.

MRS can non-invasively determine the chemical composition of a sample. Application of an RF pulse yields a spectrum of frequencies if the sample consists of magnetically non-equivalent spins. A spectrum is obtained, which consists of intensity as a function of chemical shift, typical of what is usually seen in analytical or organic chemistry. For ¹H NMR spectroscopy, one frequency component exists if the sample is pure water because the protons of water are magnetically and chemically equivalent. Two frequency components, i.e., chemical shifts, exist for methanol. Methyl and hydroxyl protons of methanol have slightly different energy separations because their respective local magnetic environments differ because orbital and bonding electrons partially shield the nucleus from B_0 . Further splitting of spectral lines is a result of scalar spin–spin couplings. This

is the basis of NMR spectroscopy where chemical composition as well as 3D molecular structure is determined. Nuclei other than protons are commonly used for MRS. Fluorine labels are often used [35, 36] because of the higher sensitivity in comparison of most other nuclei and the absence of background signals, since fluorine is not naturally occurring.

MRI and lung cancer

Clinical studies underway

Examining the literature for the use of IGDD, we begin with the clinical trials that are currently listed on the FDA.Gov web site, in which MRI is being used with lung cancer. Since these are ongoing studies, only a brief description of the objectives is provided.

The aim of NCT01065415 is to “evaluate the diagnostic efficacy of side-by-side reading of whole-body MRI/PET and to compare with that of whole-body MRI alone and that of integrated PET/CT in determining the stage of NSCLC.” This is a significant study, which has the potential to raise MRI to a status of CT, in lung cancer diagnosis.

NCT00172575 will determine “whether DCE MRI analysis of tumor angiogenesis and perfusion can be used as a reliable modality to differentiate benign from malignant solitary pulmonary nodules (SPN) before surgical intervention, using kinetic model derived from DCE MRI and can be positively correlated with angiogenesis (vascular endothelial growth factor VEGF, microvessel density MVD).” Perfusion parameters from DCE MRI will be examined for the power to predict patients’ outcomes and survival. Here too, the elevation of DCE as a valid diagnostic approach is critical and will facilitate further investigations in translating the use of MRI in animal models to humans.

“MRI sensitivity for the detection of pulmonary nodule (s) greater than 3 mm in size (diameter) compared to CT” will be studied in NCT00751920. “In addition, the accuracy of MRI in distinguishing between benign and malignant pulmonary nodules will be assessed.” Should MRI be confirmed as a reliable technique for smaller nodules, its use for screening will be enhanced.

Other clinical studies are primarily focused on MRI methodology development. In NCT01016938, the problem of movement of the lung in the diagnosis/tumor progression will be investigated. Here, an assessment will be carried out to determine “whether tumor motion can be inferred using dynamic MRI and external surrogates. The feasibility of tracking the real-time tumor position using dynamic MRI and inferring tumor position using external surrogates placed on the skin of the subject and lung function during and following radiation by assessing lung perfusion maps

obtained via dynamic MRI with dose maps in order to determine image-based biomarkers for lung toxicity following radiation therapy will be determined.”

In NCT01071434, “imaging sequences and parameters of rapid real-time MRI will be investigated and optimized in order to obtain adequate guidance for accurately and precisely delivering radiation to moving abdominal and thoracic tumors.” While investigation of pulse sequences seems esoteric, it must be appreciated that the appearance of an image is critically dependent on the specifics of the acquisition. Moreover, comparison among patients and their respective lung scans is strictly valid only when image acquisition is uniform. A related study is NCT01421784, which will address the feasibility of using rapid cine MR imaging to provide both off- and online soft-tissue-based image guidance.

Finally, there are clinical studies where the primary goal is to evaluate treatment protocols. In such studies, imaging methods are necessary aspects in monitoring tumor response. For example, NCT01047059 involves assessment of erlotinib and bevacizumab administered for a 6-week period, which will be evaluated using imaging procedures performed at baseline, after 1 week of therapy and after the 6 weeks of treatment. In addition, “early identification will be attempted by the combination of molecular and functional imaging tools (FDG-PET, FLT-PET, DCE-MRI), molecular marker analyses in tissue and peripheral blood (EGFR- and KRAS mutational status and high throughput mutational profiling in tumor tissue, angiogenesis-associated biomarkers and expression profiling in peripheral blood) and pharmacokinetic analyses.”

Pre-clinical studies

In animal studies, the use of MRI is typically limited to large masses due to the magnetic inhomogeneity of the lung. Magnetic susceptibility differences between the tissue (water) and air spaces broaden the NMR signal line width by about 8 ppm and the signal decays rapidly. Nevertheless, MRI images of rodent lungs can be obtained with remarkably good resolution (0.3 mm voxel size) [37]. The recent advances have been made through improvement in hardware and imaging technique. One uses a hydrogen-free probe that has a short “ring-down” time and a modest magnetic field strength (up to 2 T). The bandwidth of the imaging technique is matched to that of lung parenchyma. FID-projection imaging has been successful [37], but the SWIFT technique [38] should also work with lungs.

Animal studies involving diagnostic evaluation of tumors include the work by Dugas et al. [39], who delivered hyperpolarized ^3He by an electronically controlled small-animal ventilator to allow acquisition of hyperpolarized images of mouse lung. An asymmetric gradient echo imaging method

was used to enhance the signal/noise ratio of the rapidly diffusing gas. Lung cancers (melanoma) were shown to cause substantial ventilation defects confined to the cancerous regions but these effects did not extend to large-scale regions of the lung distal to the tumors [39].

Bankson et al. [40] used a mouse model of human small-cell (N417) and non-small-cell (H460) lung tumors. Scans were obtained using combinations of respiratory-gated computed tomography (CT) imaging, cardiac- and respiratory-gated multishot spin-echo echo-planar imaging (EPI), and cardiac- and respiratory-gated spoiled gradient echo (SPGR). The tumors appeared intense on T₂-weighted EPI images, providing positive intrinsic contrast between tumors and surrounding tissues. The tumor boundaries were better distinguished by EPI and SPGR with T₁-reducing contrast enhancement in comparison to CT or SPGR without contrast. Tumor volumes measured from EPI images correlated well with *ex vivo* measurements of tumor mass over a wide range of tumor sizes. These significant results were obtained with sequences that required only 2 min to complete.

In a chemopreventive study, Garbow and coworkers [41] followed the development of adenocarcinomas in the lung following urethane treatment using respiratory gated MRI methods. The tumor identification and volume were validated by histopathology upon autopsy. Tumors as small as 0.4 mm were detected by MRI, and it appeared that growth rate allow differentiation between adenocarcinomas and adenomas.

In the study by Wolf et al., nude rat human tumor xenografts (H1299, FaDu) were examined with mMRI [T₂-weighted true fast imaging with steady precession (TrueFISP), T₁-weighted fast low angle shot (FLASH), T₂-weighted dual echo steady state (DESS)] and echo-planar dwMRI in a clinical scanner at 1.5 T [42]. Tumors were visible with a significantly higher signal to noise and tumor to muscle contrast to noise ratios with dwMRI. There was no significant difference in median tumor volumes as measured by dwMRI and mMRI (TrueFISP, FLASH, and DESS). However, the intra- and inter-observer variability of dwMRI was larger than for the mMRI techniques. Such current work demonstrates the relatively large number of approaches for acquiring images with MRI and with it, the need for more studies to identify optimal approaches.

In an attempt to identify tumor xenografts in mice based on the overexpression of folate receptors on tumor cells, folate-conjugated Gd-DTPA-poly-L-lysine (folate-PL-Gd-DTPA) was used as a targeting agent [43]. MRI was performed with plain scans and enhanced scans, in which the latter were determined as a function of time following injection. In a pre-contrast to post contrast comparison, the intensity in tumor increased by only 125%, while muscle tissue exhibited no change in intensity.

In addition to tumor detection, MRI has also been used in evaluating treatment. Because of the prevalence of metastasis in lung cancer, Romaneeshsen et al. [44] carried out a study in which tumor destruction and vascular perfusion before and after freezing were investigated using native and contrast-enhanced MR imaging (T₁- and T₂-weighted spin-echo). The model consisted of subcutaneous Lu1 (a NSCLC cell line) tumors implanted in immunocompromised mice. Significant tumor reduction was evident within 2 weeks, and at 6 months, there was no evidence of recurrence, which was verified histologically. Prior to treatment, the tumors were well vascularized and did not demonstrate contrast enhancement after cryotherapy. However, after treatment, a narrow contrast-enhanced zone was seen at the border of the tumor, which was suggested to be a sign of peripheral hyperemia and central vascular stasis. These vascular changes may be related with a reduced potential for metastasis.

In another study [45], MRI was used to assess the development and progression of tumors with EGFRvIII mutants driven by doxycycline as well as the response to the EGFR inhibitor erlotinib (Tarceva). Both spin- and gradient-echo sequences with and without cardiac and respiratory gating were performed to determine two-dimensional axial tumor volumes. Three-dimensional images were obtained to characterize the spatial location and distribution. With MRI, erlotinib was shown to significantly inhibit the growth of tumor *in vivo*.

A particularly significant study was carried out by Roa et al. [46]. The main thrust of the work was to evaluate the inhalation of effervescent doxorubicin nanoparticles as a means to treat tumor bearing Balb/c mice. At this time, inhalation delivery as a means to achieve location directionality is underappreciated. However, a more thorough examination of the work reveals the demand for greater expertise to develop inhalation delivery protocols when compared to the simple intravenous injection of drug. Nevertheless, with consideration of the relatively small mass the lung represents of the entire body (about 2%), a 50-fold increase in drug concentration is predicted with inhalation. Treated animals had fewer and much smaller tumors compared with control animals. The use of nanoparticles resulted in little or no cardiotoxicity when compared with inhalation of doxorubicin solutions. T₁ weighted and transverse spin echo scans were recorded, which allowed localization of intrathoracic lung cancer and any extracancerous manifestations. The tumors gave rise to intense signals relative to adjacent tissues such as normal lung, and tumor boundaries were well delineated. In control mice, large tumor masses were evident in the visceral and mediastinal pleura, chest wall, parietal pericardium, and the heart. In isolated lung sections, multiple large and often confluent tumor masses in the parenchyma with numerous metastases throughout the alveolar septa

were evident. In contrast, MRI scans of treated mice showed no signs of intra-thoracic lung cancer (Fig. 4). The results showed a good correlation between MRI and histology data. A natural extension of such a study would be the use of MRI to determine distribution of the nanoparticles following inhalation, which may allow optimization of therapeutic doses and pave the way for the use of ligand-directed therapy.

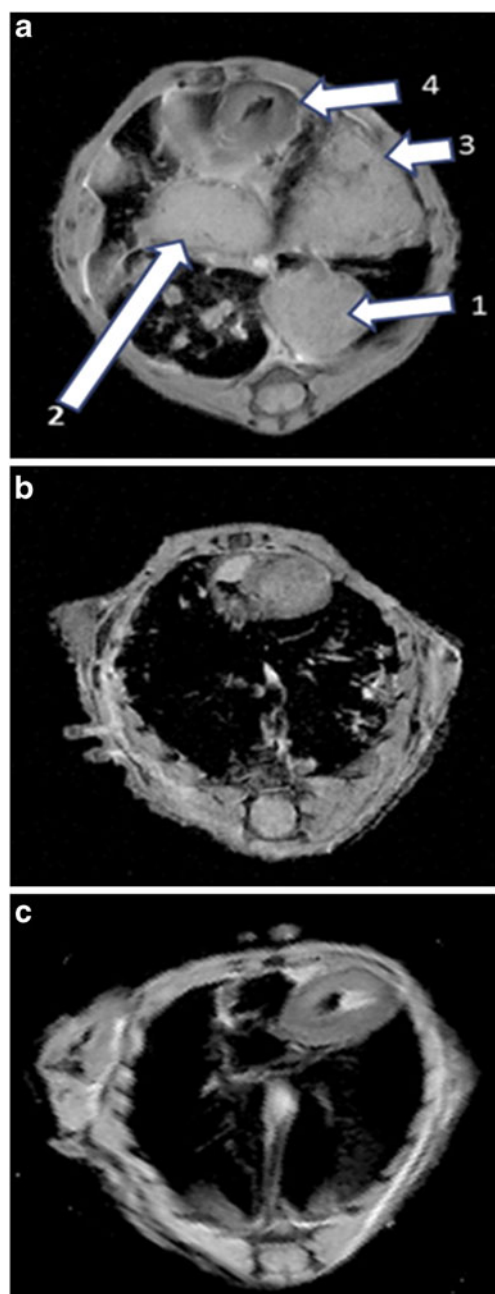


Fig. 4 T₁-weighted, transverse spin echo scans (TE/TR=13/1,500 ms, BW=50 KHz, the FOV=26×26 mm with 128×128 matrix, thickness=0.5 mm) of **a** control non-treated mouse, **b** mouse treated with effervescent doxorubicin nanoparticle powder, and **c** control mouse (not injected with cancer cells). Reproduced from [46]

MRI of drug delivery systems

There are a number of investigations involving iron oxide particles, since they are superparamagnetic and can act as contrast agents. While hundreds of papers are now being published each year, few investigations involve MRI tracking of drug delivery systems containing such particles *in vivo*. Moreover, of this smaller number of published studies, virtually none involve orthotopic models (tumor established in the lung). The surrogate model in which lung cancer cells are injected to form a subcutaneous tumor is commonly used. Iron oxide particles are strong contrast agents and are typically detected by the way they shorten the NMR signal and darken the images [47, 48]. While this approach has proven useful in tissues that are rich and relatively uniform in proton concentration, it is not a viable solution for the lung, which has inherently low intensity and thus darkened areas in all airways and alveoli [49–51].

Historically, superparamagnetic iron oxide (SPIO) nanoparticle-based contrast agents rely on either mapping T₂* values within a region or by modeling the magnetic field inhomogeneities generated by the contrast agent. An interesting development for the quantitation involves modeling of magnetic field inhomogeneities by approximating regions containing SPIOs as ensembles of magnetic dipoles [52]. This was designated as the finite perturber method. The proposed method was verified using an *in vitro* phantom and *in vivo* mouse models. Data was acquired in mice that had labeled and unlabeled C6 glioma cells subcutaneously implanted in the flanks. The proposed algorithm yielded the concentration within SPIO-labeled tumors that were reasonably close to the known concentration.

Although the particle concentration was not quantified, Gultepe et al. [53] used magnetic cationic liposomes (MCLs) with incorporated SPIO nanoparticles, to monitor cancer treatment. The theranostic system was administered to a SCID mouse with metastatic (B16-F10) melanoma grown in the flank. Pre- and post-injection magnetic resonance images were obtained, and ¹¹¹In-labeled MCLs were used to confirm the effect of targeting. Tumor signal intensities in T₂-weighted MR images decreased by 20±5%, with a decrease of 14±7 ms in T₂* 24 h after IV injection. This is compared to a 57±12% reduction in intensity and a corresponding 27±8 ms reduction in the T₂* relaxation time. This provides an important step towards the use of MRI and magnetic guidance to achieve IGDD.

Many efforts appear to approach the goal of tracking the delivery system but have not taken the critical step of demonstrating quantitation *in vivo*. For example, Guthi et al. prepared multifunctional micelles containing both doxorubicin and SPIOs [54]. *In vitro* cell culture experiments demonstrated enhanced αvβ6-dependent cell targeting in H2009 lung cancer cells relative to controls. However, no

in vivo studies were conducted, and thus the effectiveness in animal models is yet to be determined.

An analogous study by Eichhorn et al. [55] involved attachment of EndoTag-2, which is a vascular targeting agent comprising the mammalian topoisomerase I inhibitor camptothecin in its carboxylate form complexed to a cationic lipid. Targeting was evaluated in a subcutaneous model of Lewis lung (LLC-1) carcinoma and L3.6pl human pancreatic cancer model. Delivery was assessed by in vivo fluorescence. Efficacy was evaluated by histological investigation and by dynamic contrast enhanced MRI of the vasculature. Thus, while it was theoretically possible to use MRI, the authors used fluorescence to assess delivery in the mouse.

Targeted emulsions have also been used in a similar manner although not in lung cancer. Lipid coated SPIO were incorporated into a soybean oil-in-water emulsion that was stabilized with DSPC/PEG-DSPE and functionalized with $\alpha v\beta 3$ -specific RGD peptide [56]. MRI was used to image the tumor accumulation of the emulsions. Tumors of animals injected with nanoemulsions that had no SPIO appeared bright compared to surrounding muscle tissue. Tumors in mice that received SPIO-loaded nanoemulsion (either targeted or non-targeted) appeared hypointense, indicating SPIO accumulation in these tumors. T_2^* maps from the T_2^* -weighted images with different echo times were generated, which showed that the tumors of animals injected with nanoemulsions containing SPIO to be reduced by 50% compared to mice injected with nanoemulsions that did not contain SPIO.

Summary and future directions

To realize IGDD for lung cancer treatment, much work is needed. Perhaps of highest priority is developing modalities that will allow image acquisition to be connected to the current diagnosis of cancer based on microscopic evaluation of tissue sections. Following distinction between normal and cancerous tissue/cells, a strategy to differentiate among the types of cancer may be pursued by a characterization of the expression of surface receptors. While cancer diagnosis currently is determined by the morphology of the cells, identification of surface receptor expression will be a more direct path to “targeted treatments” and more amenable to detection by contrast agents that bear the appropriate ligands. However, it should be appreciated that microscopic appearance has not been correlated to any extent with surface receptor expression. Methods to image cancerous cells must be directed to those chemical features that give rise to the morphology. Here, it would seem that the better path would be through proteomics. That is, morphology may be better correlated with specific protein content, which in turn, may be exploited to give rise to unique images. This may be

approached through detection of specific proteins or more likely through functionality as in one current form of glucose utilization. The efforts by those with imaging expertise must be coupled with experts in biological characterization of normal and cancerous cells.

Because of the inherent complexity of the lung in terms of cell type, tissue geometry, and continual movement, better MRI methods are needed. These challenges are currently being addressed, while it is fully appreciated that this will not likely be achieved in the short term. The continual incremental advances in imaging pose problems, particularly for retrospective epidemiological studies as well as monitoring cancer in individual patients. As noted, the appearance of the image as generated by MRI is highly dependent on the method of acquisition. Thus, treatment evaluation within and between patients becomes difficult if improved methods are introduced during the time course of the evaluation period. While there may be benefits to the scientific and medical community to maintain existing methods, it creates an ethical dilemma to deprive patients of more improved imaging methods. This is a difficult issue and seems that only duplication of images with the distinct approaches must be used in patients, which of course also has the inherent costs of time and resources. Every effort should be made to achieve rapid dissemination of advanced techniques to those at the front lines of imaging cancer patients.

From the paucity of work reviewed in the area of imaging drug and drug delivery systems, there is evidently a great need for research. A normal and cancer cell have basically the same demands for survival, although differ in the extent. Thus, treatment of cancerous cells that are present in the midst of normal tissue will always be a critical balance between complete eradication of cancer and normal tissue safety. It is vital that evaluation of drug not only incorporate inherent pharmacological/toxicological effect but also delivery. In essence, the success of treatment is determined by the selectivity of drug delivery, which presently is poor or often unknown. Moreover, this cannot be some relative measure but should be developed to the point of quantifying drug levels in both cancer cells and the surrounding normal tissue. For this latter goal, sophisticated methodology involving PET using labeled drugs appears possible. For MRI, it may be better to track methods that rely on physical methods for cancer treatment, such as ultrasound or magnetic hyperthermia. Systematic studies, reflective of those that lead to the pharmacodynamic assessment of contrast agents for use in fMRI, can lay the groundwork for studies of individual drugs.

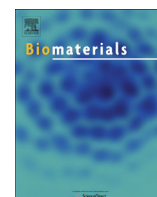
Finally, it becomes clear that the true ideal of IGDD, where drug is purposefully directed exclusively to the site of action using imaging, appears to be a distant goal. Nevertheless, the first step to paradigm-changing advances is to articulate the nature of the problem.

Acknowledgments Funding support from the Department of Defense, U.S. Army Medical Research and Materiel Command (W81XWH-10-1-0707) is acknowledged.

References

- Tandon P, Farahani K. NCI image-guided drug delivery summit. *Cancer Res.* 2011;71(2):314–7.
- American Cancer Society (cancer.org), 2009.
- Jemal A, et al. Cancer statistics, 2008. *CA Cancer J Clin.* 2008;58(2):71–96.
- Vineis P, et al. Lung cancers attributable to environmental tobacco smoke and air pollution in non-smokers in different European countries: a prospective study. *Environ Health.* 2007;6:7.
- Yang L, et al. Estimates of cancer incidence in China for 2000 and projections for 2005. *Cancer Epidemiol Biomarkers Prev.* 2005;14(1):243–50.
- Lynch TJ, et al. Early stage lung cancer—new approaches to evaluation and treatment: conference summary statement. *Clin Cancer Res.* 2005;11(13 Pt 2):4981s–3s.
- Franklin, WA. Molecular and cellular pathology of lung cancer. In: Pass HL, Carbone DE, Johnson DH, Minna JD, Turrisi AT, editors. *Lung cancer: principles and practice.* Philadelphia: Lippincott Williams & Wilkins; 2005. pp. 231–260.
- National Comprehensive Cancer Network (www.nccn.org), 2009.
- Eisenhauer EA et al. New response evaluation criteria in solid tumours: revised RECIST guideline (version 1.1). *Eur J Cancer.* 2009;45(2): 228–47.
- Manser RL et al. Screening for lung cancer. *Cochrane Database Syst Rev.* 2001;(3)CD001991.
- Humphrey LL, Teutsch S, Johnson M. Lung cancer screening with sputum cytologic examination, chest radiography, and computed tomography: an update for the U.S. Preventive Services Task Force. *Ann Intern Med.* 2004;140(9):740–53.
- Sobue T, et al. Screening for lung cancer with low-dose helical computed tomography: Anti-Lung Cancer Association Project. *J Clin Oncol.* 2002;20(4):911–20.
- Wu NY, et al. Magnetic resonance imaging for lung cancer detection: experience in a population of more than 10,000 healthy individuals. *BMC Cancer.* 2011;11:242.
- Gagnadoux F, et al. Aerosol delivery of chemotherapy in an orthotopic model of lung cancer. *Eur Respir J.* 2005;26(4):657–61.
- Molina JR, Yang P, Cassivi SD, Schild SE, Adjei AA. Non-small cell lung cancer: epidemiology, risk factors, treatment and survivorship. *Mayo Clin Proc.* 2008;83(5):584–94.
- Commission on Cancer. National cancer data base, 2006. Chicago: American College of Surgeons.
- Debrix I et al. [Anticancer chemotherapy in the elderly: a review of the literature]. *Bull Cancer.* 2008. 95 FMC Onco: p. F37–43.
- Mulshine JL, et al. Lung cancer evolution to preinvasive management. *Clin Chest Med.* 2002;23(1):37–48.
- Chhatwani L, Cabebe E, Wakelee HA. Adjuvant treatment of resected lung cancer. *Proc Am Thorac Soc.* 2009;6(2):194–200.
- Wiedmann TS, Wattenberg LW. Chemoprevention of cancer of the respiratory tract by agents delivered by aerosol: applications to glucocorticoids and 5-fluorouracil. *Cancer Chemoprevention.* 2004;1:153–67.
- Chai H, Brown RE. Field effect in cancer—an update. *Ann Clin Lab Sci.* 2009;39(4):331–7.
- Slaughter DP, Southwick HW, Smejkal W. Field cancerization in oral stratified squamous epithelium; clinical implications of multicentric origin. *Cancer.* 1953;6(5):963–8.
- Kherlopian A, et al. A review of imaging techniques for systems biology. *BMC Syst Biol.* 2008;2(1):74.
- Gore JC, et al. Magnetic resonance in the era of molecular imaging of cancer. *Magn Reson Imaging.* 2011;29(5):587–600.
- Deppen S, et al. Accuracy of FDG-PET to diagnose lung cancer in a region of endemic granulomatous disease. *Ann Thorac Surg.* 2011;92(2):428–33.
- Wahl RL, et al. Staging of mediastinal non-small cell lung cancer with FDG PET, CT, and fusion images: preliminary prospective evaluation. *Radiology.* 1994;191(2):371–7.
- Yaghoubi SS, Berger F, Gambhir SS. Studying the biodistribution of positron emission tomography reporter probes in mice. *Nat Protocols.* 2007;2(7):1752–5.
- Agool A, et al. Effect of radiotherapy and chemotherapy on bone marrow activity: a 18 F–FLT–PET study. *Nucl Med Commun.* 2011;32(1):17–22. doi:10.1097/MNM.0b013e328340798c.
- Kim SK, et al. F-18 fluorodeoxyglucose and F-18 fluorothymidine positron emission tomography/computed tomography imaging in a case of neurosarcoidosis. *Clin Nucl Med.* 2010;35(2):67–70.
- Shields AF, et al. Imaging proliferation in vivo with [F-18] FLT and positron emission tomography. *Nat Med.* 1998;4(11):1334–6.
- Yeh DW, et al. Mediastinal nodes in patients with non-small cell lung cancer: MRI findings with PET/CT and pathologic correlation. *AJR Am J Roentgenol.* 2009;193(3):813–21.
- Bloch F. Nuclear Induction. *Phys Rev.* 1946;70:460–73.
- Corot C, et al. Recent advances in iron oxide nanocrystal technology for medical imaging. *Adv Drug Deliv Rev.* 2006;58(14):1471–504.
- Zhou R, et al. SWIFT detection of SPIO-labeled stem cells grafted in the myocardium. *Magn Reson Med.* 2010;63(5):1154–61.
- Schneider E, et al. Magnetic resonance spectroscopy for measuring the biodistribution and in situ in vivo pharmacokinetics of fluorinated compounds: validation using an investigation of liver and heart disposition of tecastemizole. *J Clin Pharm Ther.* 2006;31(3):261–73.
- Tran TD, et al. Clinical applications of perfluorocarbon nanoparticles for molecular imaging and targeted therapeutics. *Int J Nanomedicine.* 2007;2(4):515–26.
- Kueth DO, Adolphi NL, Fukushima E. Short data-acquisition times improve projection images of lung tissue. *Magn Reson Med.* 2007;57(6):1058–64.
- Idiyatullin D, et al. Fast and quiet MRI using a swept radiofrequency. *J Magn Reson.* 2006;181(2):342–9.
- Dugas JP, et al. Hyperpolarized ³He MRI of mouse lung. *Magn Reson Med.* 2004;52(6):1310–7.
- Bankson JA, et al. Echo-planar imaging for MRI evaluation of intrathoracic tumors in murine models of lung cancer. *J Magn Reson Imaging.* 2008;27(1):57–62.
- Garbow JR, Zhang Z, You M. Detection of primary lung tumors in rodents by magnetic resonance imaging. *Cancer Res.* 2004;64(8):2740–2.
- Wolf G, et al. Diffusion-weighted MRI for tumour volume delineation: comparison with morphological MRI. *J Med Imaging Radiat Oncol.* 2010;54(3):194–201.
- Yuan Z, et al. Folate-poly-L-lysine-Gd-DTPA as MR contrast agent for tumor imaging via folate receptor-targeted delivery. *Zhonghua yi xue za zhi.* 2007;87(10):673–8.
- Romaneehsen B, et al. Cryotherapy of malignant tumors: studies with MRI in an animal experiment and comparison with morphological changes. *RoFo: Fortschritte auf dem Gebiete der Röntgenstrahlen und der Nuklearmedizin.* 2001;173(7):632–8.
- Zhou X, et al. Magnetic resonance imaging of the response of a mouse model of non-small cell lung cancer to tyrosine kinase inhibitor treatment. *Comp Med.* 2008;58(3):276–81.
- Roa WH, et al. Inhalable nanoparticles, a non-invasive approach to treat lung cancer in a mouse model. *J Control Release.* 2011;150(1):49–55.

47. Blanco RT, et al. Interventional and intraoperative MRI at low field scanner—a review. *Eur J Radiol.* 2005;56(2):130–42.
48. Hersman FW, et al. Large production system for hyperpolarized ^{129}Xe for human lung imaging studies. *Acad Radiol.* 2008;15(6):683–92.
49. Garbow JR, Zhang Z, You M. Detection of primary lung tumors in rodents by magnetic resonance imaging. *Cancer Res.* 2004;64(8):2740–2.
50. Hayashi N, et al. Utilization of low-field MR scanners. *Magn Reson Med Sci.* 2004;3(1):27–38.
51. Laurent F, Montaudon M, Corneloup O. CT and MRI of lung cancer. *Respiration.* 2006;73(2):133–42.
52. Langley J, et al. Quantification of SPIO nanoparticles in vivo using the finite perturber method. *Magn Reson Med.* 2011;65(5):1461–9.
53. Gultepe E, et al. Monitoring of magnetic targeting to tumor vasculature through MRI and biodistribution. *Nanomedicine.* 2010;5(8):1173–82.
54. Guthi JS, et al. MRI-visible micellar nanomedicine for targeted drug delivery to lung cancer cells. *Mol Pharm.* 2009;7(1):32–40.
55. Eichhorn ME, et al. Cationic lipid complexed camptothecin (EndoTAG®-2) improves antitumoral efficacy by tumor vascular targeting. *Cancer Biol Ther.* 2007;6(6):920–9.
56. Gianella A, et al. Multifunctional nanoemulsion platform for imaging guided therapy evaluated in experimental cancer. *ACS Nano.* 2011;5(6):4422–33.
57. Kaira K, et al. ^{18}F -FMT uptake seen within primary cancer on PET helps predict outcome of non-small cell lung cancer. *J Nucl Med.* 2009;50(11):1770–6.



Enhancing therapeutic efficacy through designed aggregation of nanoparticles



Tanmoy Sadhukha^a, Timothy S. Wiedmann^a, Jayanth Panyam^{a, b, *}

^a Department of Pharmaceutics, College of Pharmacy, University of Minnesota, Minneapolis, MN 55455, USA

^b Masonic Cancer Center, University of Minnesota, Minneapolis, MN 55455, USA

ARTICLE INFO

Article history:

Received 16 April 2014

Accepted 28 May 2014

Available online 16 June 2014

Keywords:

Superparamagnetic iron oxide

Magnetic hyperthermia

Aggregation

Necrosis

Apoptosis

Autophagy

ABSTRACT

Particle size is a key determinant of biological performance of sub-micron size delivery systems. Previous studies investigating the effect of particle size have primarily focused on well-dispersed nanoparticles. However, inorganic nanoparticles are prone to aggregation in biological environments. In our studies, we examined the consequence of aggregation on superparamagnetic iron oxide (SPIO) nanoparticle-induced magnetic hyperthermia. Here we show that the extent and mechanism of hyperthermia-induced cell kill is highly dependent on the aggregation state of SPIO nanoparticles. Well-dispersed nanoparticles induced apoptosis, similar to that observed with conventional hyperthermia. Sub-micron size aggregates, on the other hand, induced temperature-dependent autophagy through generation of oxidative stress. Micron size aggregates caused rapid membrane damage, resulting in acute cell kill. Overall, this work highlights the potential for developing highly effective anticancer therapeutics through designed aggregation of nano delivery systems.

© 2014 Elsevier Ltd. All rights reserved.

1. Introduction

Nano drug delivery systems are of considerable interest in cancer therapy because of their ability to accumulate passively in tumors [1–3]. A key area of research is the effect of size of the delivery system on therapeutic effectiveness [4–6]. Several reports suggest that the optimal size of nanoparticles for tumor therapy is around 100 nm [3]. However, the presence of proteins can lead to aggregation of nanoparticles in biological environment [7–10]. For example, depending on the surface properties, nanoparticles can form sub-micron to micron size aggregates in the presence of serum proteins [11,12]. The effect of aggregation on the therapeutic performance of nanoparticles has not been previously investigated.

In our studies, we examined the consequence of aggregation on superparamagnetic iron oxide (SPIO) nanoparticle-induced magnetic hyperthermia (MH). Superparamagnetic materials generate heat when placed in alternating magnetic field [13,14]. Depending on the size of the material, heat is generated through either Néel or Brownian relaxation or a combination of the two [15,16]. Heat generated and the associated temperature change from such

relaxation phenomena dissipate over short distances due to the high thermal conductivity of water and can therefore be used for highly focused heating [17,18]. This concept is utilized in MH, where an external magnetic field is applied to SPIO nanoparticles trapped in tumor tissue that results in local heating and tumor cell kill [18].

We hypothesized that the aggregation state of SPIO nanoparticles will affect their magnetic properties, which, in turn, will affect their tumor cell kill effectiveness. To test this hypothesis, we fabricated SPIO nanoparticle aggregates of various sizes and evaluated their ability to induce MH in cell culture models as well as in a mouse subcutaneous model of lung cancer.

2. Materials and methods

2.1. Materials

Ferrous chloride tetrahydrate, ferric chloride hexahydrate, myristic acid, Pluronic F127, ascorbic acid, potassium hydroxide, 1,10-phenanthroline and sodium acetate were purchased from Sigma (St. Louis, MO). Penicillin/streptomycin, fetal bovine serum, Dulbecco's phosphate buffered saline, F-12K (Kaighn's modification) and trypsin-EDTA solution were obtained from Invitrogen Corporation (Carlsbad, CA). Cytotox 96[®] non-radioactive cytotoxicity assay and CellTiter 96[®] Aqueous one solution cell proliferation assay kit were purchased from Promega (Madison, WI). The commercial SPIO nanoparticles (Nanomag[®]) were purchased from Micromod Partikeltechnologie GmbH (Rostock, Germany). For Western blotting, antibody against HSP70 was from Enzo Life Sciences (Farmingdale, NY), anti-GAPDH-HRP and anti-β-actin-HRP were from Sigma, anti-PARP1, anti-cleaved PARP1, anti-LC3B and HRP-linked anti-rabbit and anti-mouse IgG were from Cell Signaling Technology (Danvers, MA).

* Corresponding author. Department of Pharmaceutics, College of Pharmacy, University of Minnesota, Minneapolis, MN 55455, USA. Tel.: +1 612 624 0951; fax: +1 612 626 2125.

E-mail addresses: jpanyam@gmail.com, jpanyam@umn.edu (J. Panyam).

2.2. Methods

2.2.1. Synthesis of SPIO nano and micro aggregates

SPIO nanoparticles were synthesized by condensation of 0.82 g ferric chloride hexahydrate and 0.33 g ferrous chloride tetrahydrate dissolved in 30 ml of degassed and nitrogen-purged water with 3 ml of 5 M ammonium hydroxide. The reaction was allowed to continue for 30 min under magnetic stirring (200 G magnetic stir bar, 1600 rpm) and nitrogen gas bubbling through the reaction mixture. Iron oxide formed was washed three times with 30 ml of nitrogen-purged water, followed by magnetic separation and heating on a hot (80 °C) oil bath. About 100 mg of myristic acid was added to the heated mixture, which was stirred for another 30 min at 1600 rpm using a 200 G magnetic stir bar. Excess myristic acid was removed by two washes with acetone, followed by two washes with water to remove excess acetone. Each wash was followed by magnetic separation of nanoparticles. The myristic acid-coated particles were then suspended in 30 ml water using a water-bath sonicator and 100 mg of Pluronic F127 was added and stirred overnight. The final dispersion was fractionated by centrifugation at 800 g for 6 min. The supernatant contained nano aggregates. The pellet was dispersed in 15 ml of water and 20 mg Pluronic F127 by sonication for 1 h and was comprised of micro aggregates.

Coumarin-6 labeled SPIO nanoparticles were synthesized by incorporating coumarin-6 into the fatty acid layer of SPIO nanoparticles dispersed in water [19]. One ml of 500 µg/ml coumarin-6 in ethanol was added to 100 mg magnetite equivalent of SPIO NP in 10 ml of water and stirred overnight. The coumarin-6 labeled SPIO nanoparticles were washed three times in water followed by magnetic separation of nanoparticles. The final product was dispersed in 10 ml of water and 5 mg Pluronic F127 and inspected under a fluorescent microscope to confirm the presence of dye-label on particles.

2.2.2. Characterization of SPIO nanoparticles

2.2.2.1. Particle size. The hydrodynamic diameter of SPIO nanoparticles was determined by dynamic light scattering. About 1 mg of SPIO nanoparticles was dispersed in 2 ml of deionized water by sonication, and the dispersion was subjected to particle size analysis using a Delsa™ Nano C Particle Analyzer (Beckman, Brea, CA). Measurements were performed at 25 °C and at a 165° scattering angle. Mean hydrodynamic diameter was calculated based on size distribution by weight, assuming a lognormal distribution. For transmission electron microscopy (TEM), a drop of an aqueous dispersion of SPIO nanoparticles was placed on a Formvar®-coated copper grid (150 mesh, Ted Pella Inc. Redding, CA). Excess liquid was removed using a filter paper, and the grid was allowed to air-dry. Particles were imaged using a JEOL JEM-1210 transmission electron microscope (Peabody, MA). The diameters of at least 100 different particles were measured using ImageJ software and averaged to determine the mean Feret's diameter.

2.2.2.2. Composition. The form of iron oxide was assessed by Fourier-transformed infrared spectroscopy (FT-IR). About 5 mg of SPIO nanoparticles was analyzed using Vertex 70 FT-IR spectrophotometer (Bruker Optics Inc., Billerica, MA). Scans were performed from 4000 cm⁻¹ to 400 cm⁻¹ and each spectrum was obtained by averaging 16 interferograms at a resolution of 2 cm⁻¹. The data was collected and analyzed using OPUS software (Bruker Optics Inc., Billerica, MA). Magnetic properties were determined with an accurately weighed sample of SPIO nanoparticles, which was sprinkled on a lightly greased silicon wafer and placed in a vibrating sample magnetometer (Micromod Model 3900, Princeton, NJ) operating at room temperature. Magnetization curves were recorded in magnetic fields ranging from -1 T to 1 T, at increments of 0.002 T. The curve was normalized to the mass of magnetite to obtain the saturation magnetization per gram of magnetite. The composition of SPIO nanoparticles was estimated using 1,10 phenanthroline-based iron assay [20]. SPIO nanoparticles were dissolved in 12 N hydrochloric acid. The solution was then diluted with distilled water to obtain a final acid concentration of 0.2 N. To this acid solution, 10 mg/ml ascorbic acid, 1.2 mg/ml 1,10 phenanthroline, 22.4 mg/ml potassium hydroxide and 123 mg/ml sodium acetate were added in a volume ratio of 1:1:1:1:5. Absorbance of the resultant solution was measured at 490 nm using a microplate reader (ELx800 Absorbance Microplate Reader, Biotek, Winooski, VT). Solutions of commercial iron oxide powder and ferric chloride (hexahydrate) in 0.2 N hydrochloric acid were used as standards.

2.2.2.3. Heating rate. The heating rates for different formulations were determined by placing 0.5 ml of the formulation (2 mg/ml or 1 mg/ml magnetite equivalent) in AMF. Temperature measurement was performed every 2 s using a fluoroptic probe inserted in the middle of the sample. Sample temperature was monitored for 30 s to ensure temperature stability, after which AMF was turned on. Specific loss power (SLP) was calculated from the initial heating rate (60 s) as the product of magnetite concentration, temperature change and the specific heat capacity of water. The contribution of the polypropylene sample tube (0.6 ml volume) to heat loss was ignored in SLP calculations.

2.2.3. Cell culture studies

A549 (human lung adenocarcinoma) and A549-Luc (stable luciferase expressing) cells were used in the study. Both cells were propagated using F-12K medium supplemented with 10% fetal bovine serum (FBS) and 1% antibiotic solution and maintained at 37 °C and in 5% carbon dioxide.

2.2.3.1. Cell death after magnetic hyperthermia. About 1 million cells were suspended in 500 µl of F-12K (with 10% FBS) and mixed with 500 µl SPIO nano or micro aggregates in saline to make a final concentration of 1.75 mg/ml magnetite. The suspension was placed in AMF (6 kA/m, 386 kHz) for 5, 15 or 30 min, maintaining the temperature of the cell suspension between 43 and 46 °C. Cells not exposed to AMF, with or without SPIO nanoparticles, served as control. Additionally, cells were kept in a water bath for 30 min at 46 °C, to serve as conventional hyperthermia controls. Magnetic hyperthermia induced using a commercial formulation of dextran-coated SPIO (Nanomag®-D-SPIO) was also used for comparison of *in vitro* efficacy. Cells were pelleted 2 h following treatment, and the amount of LDH released by the cells in the supernatant was determined. LDH released by same number of freeze-thaw lysed cells was used to calculate 100% cell death. In addition, 50,000 treated cells were plated per well in a 24-well plate and assayed for cell survival after 24 h by MTS assay.

2.2.3.2. Instantaneous PI uptake during AMF exposure. About 1 million cells were suspended in 500 µl of F-12K (with 10% FBS) and incubated with 500 µl nano or micro aggregates or Nanomag® in saline (final concentration of 1.75 mg/ml magnetite) at 4 °C for 30 min. To each tube, 10 µM PI was added, and the treated cells were subjected to 30 min of AMF, while maintaining the cell suspension temperature below 5 °C with an ice bath. Cells not exposed to AMF, with or without SPIO nanoparticles, were used as controls. Following AMF exposure, cells were immediately washed with buffer, resuspended in medium and kept on ice. PI present in cells was detected in the FL-3 channel of the flow cytometer (BD, FACSCalibur™). Data from 10,000 cells in each group were analyzed using Cyflog software.

2.2.3.3. Reactive oxygen species (ROS) generation. Immediately prior to the addition of SPIO formulations, 5-(and-6)-chloromethyl-2',7'-dichlorodihydrofluorescein diacetate acetyl ester (CM-H₂DCFDA) (7.5 µM) and PI were added to the cell suspension. Cells were subjected to flow cytometric analysis after 2 h. The deacetylated and oxidized product, 2',7'-dichlorofluorescein, formed due to ROS generation in the cells, was detected in the FL-1 channel while PI fluorescence was detected in the FL-3 channel.

2.2.3.4. Western blot analysis. Cells were lysed using RIPA buffer containing protease inhibitor cocktail (Sigma) on ice. Cell lysates were centrifuged at 13,000 rpm for 10 min to pellet the insoluble cellular debris, and the supernatant was analyzed. Protein concentration in the supernatant was determined by the bicinchoninic acid assay (Thermo Scientific). Protein samples (15 µg) were loaded onto a 4–15% Tris-hydrochloride gel (Bio-Rad Laboratories) and, after electrophoresis for 40 min at 100 V, transferred onto a nitrocellulose membrane (Whatman) using a Criterion blotter (Bio-Rad Laboratories). The membrane was blocked with 5% non-fat dry milk in tris-buffered saline containing Tween 20 (TBST) for 1 h. The membrane was then incubated overnight at 4 °C with primary antibodies against PARP1, cleaved PARP1, HSP70, LC3B, GAPDH-HRP or β-actin-HRP, diluted in either 5% non-fat dry milk in TBST or 5% BSA in TBST. After three 8-min washes with TBST, the membrane was incubated with horseradish peroxidase-conjugated anti-rabbit (for PARP1, cleaved PARP1 and LC3B) or anti-mouse (for HSP70) IgG in 5% non-fat dry milk in TBST for 1 h and then washed three times with TBST. Protein bands were then visualized using SuperSignal West Pico Chemiluminescent Substrate (Thermo Scientific). For densitometric quantification, immunoblots were digitized on a flatbed scanner and the signal intensities of the visualized bands were quantified using ImageJ (NIH) and OriginPro 8 software (OriginLab Corporation, Northampton, MA).

2.2.3.5. Confocal microscopy. Following incubation with coumarin-6 labeled SPIO nanoparticles and AMF exposure, cells were stained with LysoTracker® red DND-99 (Invitrogen) for 30 min at 37 °C or Texas red®-X conjugated wheat germ agglutinin (Invitrogen) for 10 min at 37 °C and washed with phosphate buffered saline. Ten µl of the cell suspension was added to a glass slide, mounted by a cover glass and sealed with clear nail polish. The slides were imaged using a 40×/1.30 numerical aperture oil-immersion objective in an Olympus Fluoview FV1000 BX2 upright confocal microscope (Olympus Corporation). The images were analyzed using FV1000 Viewer software (Olympus Corporation) and ImageJ (NIH).

2.2.3.6. Effect of aggregate size on cell kill by magnetic hyperthermia. To further investigate the effect of aggregate size on cell kill by magnetic hyperthermia, we performed additional fractionation of SPIO aggregates. The final dispersion containing myristic acid-coated and Pluronic-stabilized SPIO nanoparticles was fractionated by centrifugation at 400 g for 6 min. The residue from this step was termed Fraction A. The supernatant was further centrifuged at 600 g for 6 min, 800 g for 6 min and 1200 g for 6 min, and the residue was separated from the supernatant following each fractionation. The residues from each of the centrifugation runs were labeled Fractions B-D, and the final supernatant was labeled Fraction E. The hydrodynamic size of the fractions A, B, C, D and E was 1000 nm (1003 ± 90 nm), 750 nm (748 ± 44 nm), 405 nm (406 ± 17 nm), 345 nm (344 ± 8 nm) and 220 nm (221 ± 2 nm), respectively.

About 1 million cells were suspended in 500 µl of F-12K medium (with 10% FBS) and mixed with 500 µl of SPIO Fraction A, B, C, D or E in saline, resulting in a final concentration of 1.75 mg/ml magnetite. The suspension was placed in AMF (6 kA/m, 386 kHz) for 15 min, maintaining the temperature of the cell suspension between 43 and 46 °C. Cells not exposed to AMF, with or without SPIO nanoparticles, served as controls. Cells were pelleted 2 h following treatment, and the amount of LDH

released by the cells in the supernatant was determined. LDH released by same number of freeze-thaw lysed cells was used to normalize for 100% cell death.

2.2.4. In vivo tumor growth studies

The study was carried out in compliance with protocol approved by the Institutional Animal Care and Use Committee at the University of Minnesota. Female BALB/c-nude mice (C.Cg/AnNTac-Foxn1^{nu} NE9; Taconic Farms), four to six weeks of age, were used for the studies. One million A549-Luc cells were injected subcutaneously in the abdominal region of the mice, and the tumor dimensions were measured every other day using digital calipers. The tumor volume (V) was calculated using the formula $V = 0.5(L \times W^2)$, where L and W are the longest and shortest diameters, respectively. When the tumor volume reached 150 mm³, 40 μ l of saline or 225 μ g magnetite equivalent of nano or micro aggregate suspension was injected intratumorally and allowed to distribute inside the tumor for 24 h [21]. After 24 h, animals in the MH groups were anesthetized, and their abdominal region (tumor region) was exposed to AMF (6 kA/m, 386 kHz) for 30 min. The tumor temperature was measured using an infrared camera (Infrared solutions), where snapshots of the AMF exposed tumor region of the mice were acquired every 2 min. The temperature elevation in the tumor during MH was added to the normal body temperature (assumed to be 37 °C) to obtain the calculated tumor temperatures. Tumor volumes were measured every other day after treatment by calipers, and bioluminescence imaging (IVIS Spectrum, PerkinElmer) of the tumors was performed every week. Development of 1000 mm³ tumors or 30 days after cell injection (whichever came first) marked the end of the study for each animal. At the end of the study, the tumors were excised, formalin fixed, paraffin embedded, sectioned and stained with Prussian blue (for iron) or hematoxylin and eosin (for cellular structure). In a separate set of animals, the tumors were excised immediately after MH treatment and processed for Prussian blue and hematoxylin-eosin staining.

2.2.5. Statistical analysis

Statistical analyses were performed using one-way ANOVA, followed by Bonferroni–Holm testing for comparison between individual groups. A probability level of $P < 0.05$ was considered significant.

3. Results and discussion

3.1. Effect of aggregate size on in vitro cytotoxicity

To study the effect of aggregation on therapeutic performance, we used a synthetic technique that facilitated the aggregation of SPIO nanoparticles. The final product was fractionated into micro and nano size aggregates. Nano aggregates had an average hydrodynamic diameter of 207 ± 3 nm. Micro aggregates had an average size of 1052 ± 65 nm. The aggregates were composed of 12 ± 3 nm iron oxide cores (Fig. 1a–d), which were confirmed to be magnetite (Fig. 1e). Both nano and micro aggregates had high saturation magnetization of 72.9 and 67.7 emu/g of magnetite, respectively, with negligible remanence (1.64 and 1.44 emu/g of magnetite, respectively) and coercivity (2.73 and 2.36 Oe), verifying their superparamagnetic nature (Fig. 1f). The heating profiles for the two fractions were virtually identical (Fig. 1g). The specific loss powers for the aggregates were also similar (89.6 ± 2.8 W/g and 93 ± 5.6 W/g for nano and micro aggregates, respectively). As a control, we used a commercial well-dispersed 100-nm SPIO nanoparticle formulation (Nanomag[®]; specific loss power of 68.9 ± 4.3 W/g) in our studies.

Nano aggregate-mediated hyperthermia resulted in a time-dependent decrease in cell survival. Lactate dehydrogenase (LDH) release was not significantly increased at two hours following MH treatment (Fig. 2a); however, less than 10% of the treated cells survived at 24 h (Fig. 2b). Similar inefficient early LDH release and

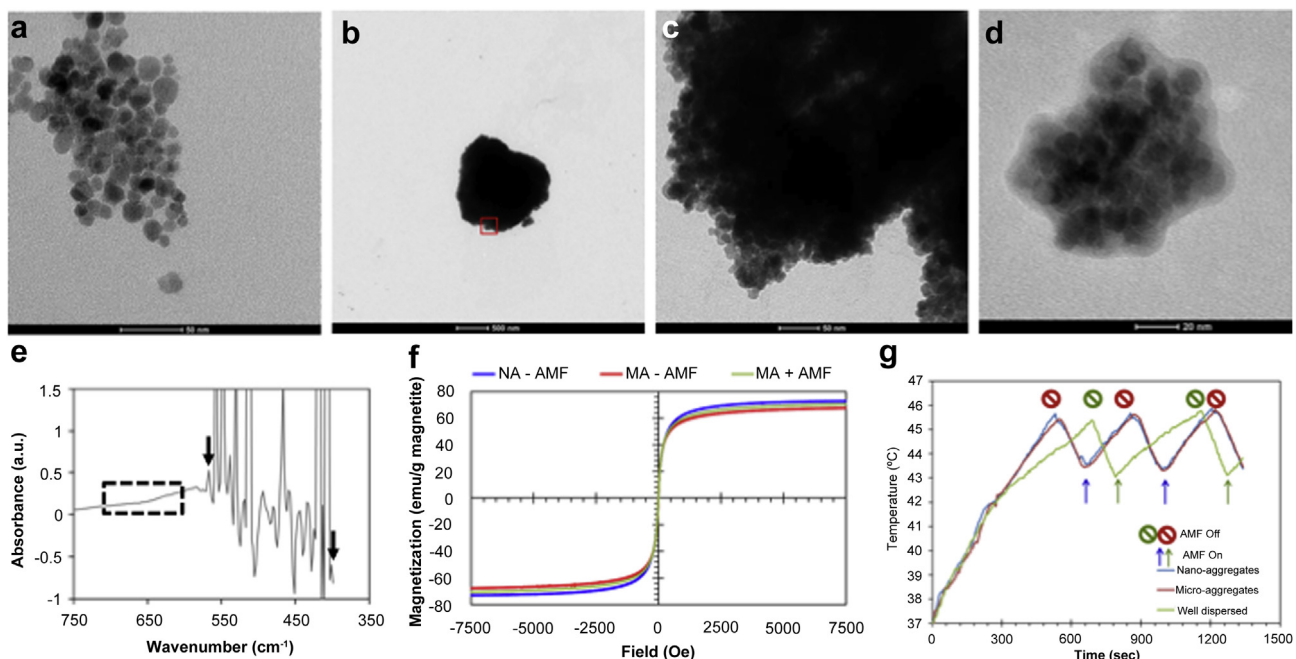


Fig. 1. Characterization of SPIO aggregates. (a) Representative TEM image of SPIO nano aggregate showing a 100–200 nm aggregate composed of 12 ± 3 nm SPIO core (average Feret's diameter of 100 different SPIO cores measured using ImageJ software). Scale bar, 50 nm. (b) TEM image of micro aggregates showing a large electron dense particle (about 1.5 μ m in size). Scale bar, 500 nm. (c) Higher magnification image of the boxed area of (B) demonstrating that the micro aggregates are also composed of the smaller SPIO cores tightly packed together to form the larger structure. Scale bar, 50 nm. (d) TEM image of uranyl acetate counterstained SPIO nano aggregates showing that the SPIO cores are enveloped by myristic acid/pluronic F127 coating to form stable aggregates. The size of micro aggregates interfered with the visualization of coating on them. (e) FT-IR spectrum of SPIO nanoparticles. Presence of characteristic magnetite bands at 570 cm^{-1} and 400 cm^{-1} (arrow) and absence of maghemite bands at 700 cm^{-1} and $630\text{--}660\text{ cm}^{-1}$ (box) indicate that the primary form of iron oxide is magnetite. (f) Magnetization curves of nano aggregates (NA) and micro aggregates (MA) recorded on a vibrating sample magnetometer. The curve was normalized to the weight of magnetite added to obtain saturation magnetization per gram of magnetite. The sigmoidal curve is characteristic of superparamagnetic substances. The data shows that the saturation magnetization of nano and micro aggregates was similar (~ 70 emu/g magnetite). Additionally, exposure of micro aggregates to AMF did not alter their saturation magnetization or superparamagnetic properties. (g) Heating rates of the different SPIO formulations (1.75 mg/ml magnetite equivalent) placed in an alternating magnetic field of 6 kA/m and operating at a frequency of 386 kHz. The initial temperature was equilibrated to 37 °C, and temperature of the SPIO NP dispersion was sampled at 5 s intervals using a fluoroptic probe following the application of magnetic field. The magnetic field was stopped when the temperature reached about 45.5 °C and restarted at 43.5 °C. The graph shows the similarity in the heating profiles of nano and micro aggregates during the three AMF on/off cycles. In spite of the slower heating rate of the well-dispersed particles, the temperature was still maintained between 43 °C and 46 °C in this group.

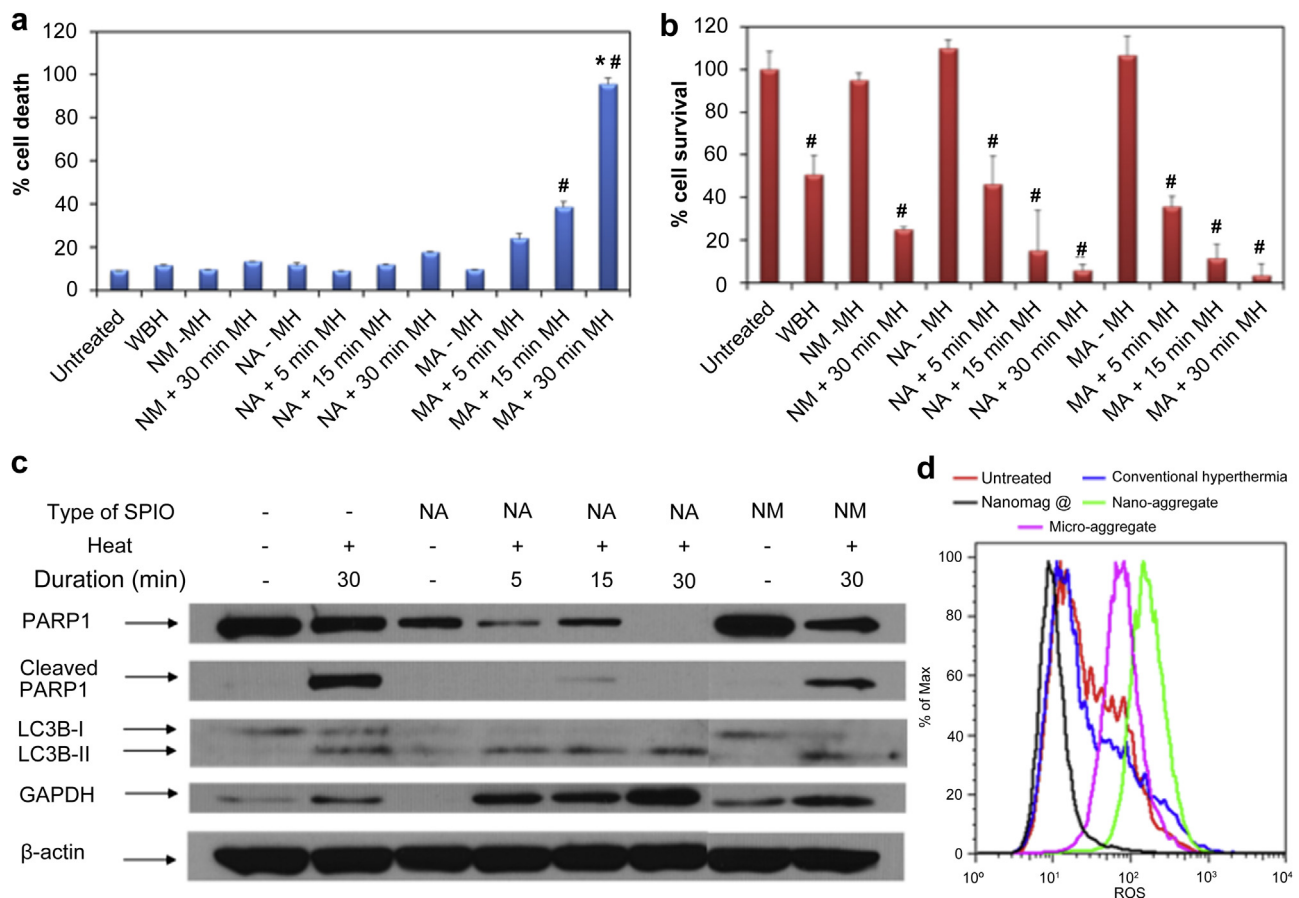


Fig. 2. Effect of SPIO nanoparticle aggregate size on the mechanism of cell kill by MH. Effect of nano aggregate (NA), micro aggregate (MA) and commercial nanoparticle (Nanomag®; NM)-mediated MH and conventional hyperthermia (WBH) on (a) cell death quantified by LDH release from the cells 2 h after treatment and (b) cell survival 24 h after treatment measured by MTS assay. A549 cell suspension containing different SPIO formulations (1.75 mg/ml magnetite equivalent) were subjected to 5 min, 15 min or 30 min of AMF after the suspension temperature reached 43 °C. Untreated cells or cells incubated with SPIO formulations without AMF exposure (-MH) were used as controls. Conventional hyperthermia involved maintaining cells at 46 °C for 30 min on a water bath. Data shown is mean ± S.D., $n = 3$. * $P < 0.00001$ vs. cells exposed to 30 min heating with different treatment; # $P < 0.001$ vs. corresponding unheated control. (c) Western blotting analysis of expression of PARP1 (116 kDa), cleaved PARP1 (89 kDa), LC3B-I (16 kDa), LC3B-II (14 kDa), GAPDH (37 kDa) and beta actin (44 kDa) 24 h after MH treatment as in (A) and (B). (d) ROS generation after different treatments. CM-H2DCFDA was added to A549 cells immediately before exposure to alternating magnetic field and after 2 h, the cells were analyzed by flow cytometry to determine ROS levels. The graph shows a representative ROS profile of cells after treatment. Neither conventional hyperthermia nor Nanomag® mediated MH resulted in the elevation of ROS production relative to that in untreated cells. However, both nano and micro aggregate mediated MH led to an elevation of ROS levels in the cells. The concentration of different SPIO aggregates used was 1.75 mg/ml magnetite equivalent.

higher cell death at 24 h was also observed in cells subjected to conventional hyperthermia or MH using a commercial well-dispersed 100-nm SPIO nanoparticle formulation (Nanomag®). This was not surprising, given that hyperthermia has been shown to induce apoptotic cell death, a slow process that takes several hours [22–24]. Both Nanomag®-mediated MH and conventional hyperthermia resulted in PARP1 cleavage (Fig. 2c), confirming the induction of apoptosis with these treatments. However, nano aggregate-induced MH resulted in a decrease in the levels of intact 116 kDa PARP1 protein (Fig. 2c, Supporting Information Figure S1a), without a concomitant increase in levels of the cleaved PARP1 fragment (89 kDa) (Fig. 2c, Supporting Information Figure S1b), a marker for caspase-dependent apoptosis [25]. The lysosomal enzyme cathepsin, which is released after lysosomal rupture such as during autophagy [26], can cleave PARP1 into fragments of different sizes (44, 55, 62 and 74 kDa) [27], and thereby decrease PARP1 levels without a detectable increase in the 89 kDa fragment. Expression of LC3B-II (Fig. 2c), an autophagy marker [28], further points to autophagy as the primary cell kill mechanism with nano aggregate-mediated MH.

Autophagy is a form of programmed cell death mediated by the lysosomal machinery and intracellular membrane rearrangement,

which leads to massive degradation of cellular components [29]. Autophagy involves sequestration of cytoplasmic components in a membrane vesicle called autophagosome, which then fuses with the lysosome to form an autolysosome. Proteases within the autolysosome degrade the sequestered cytoplasmic components. Oxidative stress has been shown to play an important role in inducing autophagy [30,31]. We determined the level of reactive oxygen species (ROS) produced by cells subjected to different treatments. The ROS levels remained unchanged after conventional hyperthermia and Nanomag®-induced MH. However, nano aggregates resulted in elevated cellular ROS levels (Fig. 2d). One of the effectors of oxidative stress is GAPDH [32], which causes an elevation of cellular glycolysis and drives autophagy [33]. MH using SPIO nanoparticle formulations resulted in elevated GAPDH protein levels, and this increase was greatest in cells subjected to nano aggregate-mediated MH (Fig. 1c, Supporting Information Figure S1c).

With micro aggregates, we observed significant LDH release from treated cells at 2 h following MH treatment (~90% cell kill with 30 min of MH, Fig. 2a). Acute LDH release with micro aggregates indicated that the cell membrane was compromised rather quickly, pointing to a necrotic cell death mechanism [34]. To further

determine the mechanism of necrosis and to confirm membrane damage, cells incubated with SPIO aggregates were subjected to alternating magnetic frequency (AMF) at a low temperature ($<5^{\circ}\text{C}$). Acute membrane damage induced by this treatment was determined by monitoring the 'instantaneous' propidium iodide (PI) uptake by treated cells [35]. Only the cells treated with micro aggregates demonstrated instantaneous PI uptake in the absence of temperature elevation (Fig. 3a). Neither nano aggregates (Fig. 3b) nor Nanomag[®] (Fig. 3c) was effective in inducing instantaneous PI uptake. We further investigated the effect of size of aggregates on cytotoxicity. Interestingly, these studies suggest that the cytotoxic

effect evolves into necrotic mechanism around 400 nm (Fig. 3d). In addition, we evaluated the behavior of the different formulations under varying magnetic field frequencies. Our results showed that only micro aggregates induced significant instantaneous PI uptake in the presence or absence of bulk temperature elevation at all the frequencies tested (Fig. 3e–g). Interestingly, the field frequency had a larger effect on micro aggregate-induced acute cell kill in the absence of bulk temperature elevation.

Additionally, while conventional hyperthermia and Nanomag[®] or nano aggregate-induced MH caused an elevation of heat shock protein 70 (Hsp70), micro aggregate-mediated MH showed no such

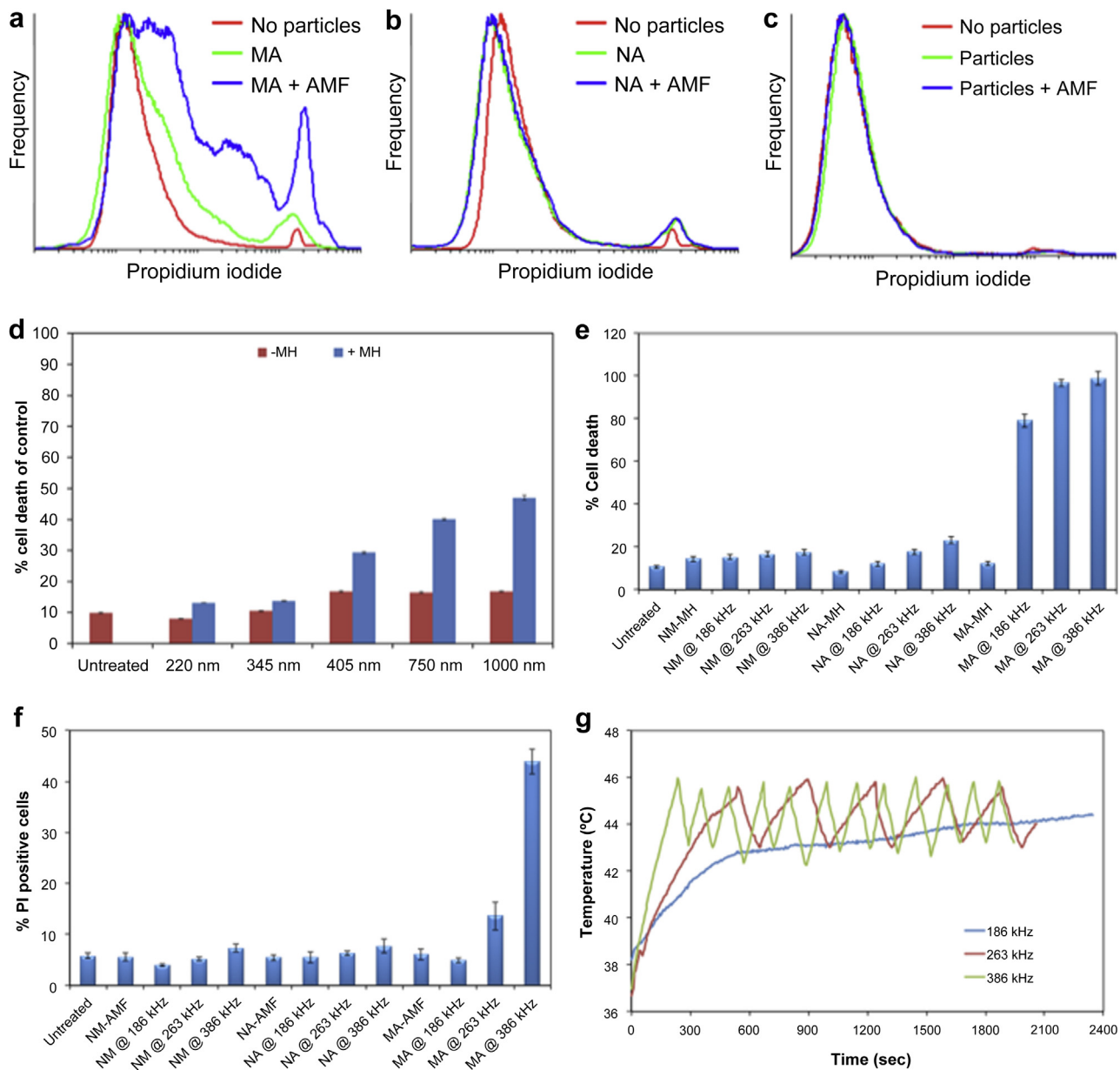


Fig. 3. Effect of SPIO nanoparticle aggregate size on acute cell kill. Flow cytometric analysis of instantaneous PI uptake by cells incubated with (a) micro aggregates, (b) nano aggregates and (c) Nanomag[®] and subjected to AMF under low temperature ($<5^{\circ}\text{C}$). PI was added to the cell suspension immediately prior to AMF exposure (30 min), washed after treatment to eliminate the excess PI and analyzed by flow cytometry. Data shown is representative PI profile of the different treatments ($n = 3$). Micro aggregates showed an increase in PI positive population after AMF exposure. (d) The effect of SPIO nanoparticle aggregate size on cell kill by MH was studied. A549 cell suspension containing different SPIO formulations (1.75 mg/ml magnetite equivalent) was subjected to 15 min of AMF after the suspension temperature reached 43°C . Untreated cells or cells incubated with SPIO formulations without AMF exposure (-MH) were used as controls. Cell death was quantified by LDH release from the cells 2 h after treatment. Data shown is mean \pm S.D., $n = 3$. * $P < 0.05$ Vs Untreated. To study the effect of magnetic field frequency on cell kill by SPIO nanoparticle aggregates, A549 cell suspension containing different SPIO formulations (1.75 mg/ml magnetite equivalent) was subjected to 30 min of AMF, (e) with temperature elevation (43 – 46°C) or (f) at low temperature ($<5^{\circ}\text{C}$). Cell death was quantified by LDH release from the cells 2 h after treatment (e) or by instantaneous PI uptake (f). (g) Heating rates at different frequencies for (e). The operating frequency of AMF was varied from 186 to 386 kHz. Data shown is mean \pm S.D., $n = 3$. NA = nano aggregates, MA = micro aggregates, NM = Nanomag[®]. # $P < 0.01$ vs. all other treatments.

increase (Supporting Information Figure S1d,e). This further verified the role of temperature elevation as the primary mechanism of cell death with sub-micron aggregates and a temperature-independent cell death mechanism with micro aggregates. Induction of Hsp70 expression also suggests the possibility of triggering Hsp70-mediated resistance to radiotherapy [36,37].

3.2. Mechanism of micro aggregate-mediated membrane damage

The mechanism of membrane damage induced by micro aggregates was also assessed by an examination of the cellular distribution of the aggregates. Coumarin-6 (a lipophilic green fluorescent dye) was incorporated in SPIO nanoparticles to aid in the visualization of particles [38]. Confocal microscopic images showed the presence of aggregates on cell surfaces and in the lysosomes (Fig. 4a). In the absence of AMF, incubation with micro aggregates did not affect the cell membrane integrity (Fig. 4b). Exposure to AMF caused blebbing of the membrane at points where

the micro aggregates contacted the cell membrane (Fig. 4b). The membrane blebs were large and characteristic of necrotic blebs [39]. Additionally, the blebbed cells also stained positive for PI, indicating the loss of membrane integrity in these cells (Fig. 4c). Thus, these observations support the hypothesis that the cell membrane damage is a consequence of the direct contact of SPIO nanoparticles with the membrane. Others have suggested that SPIO nanoparticles induce membrane damage as a result of intense local heat generation [40,41]. However, additional studies are needed to investigate the specific mechanism of membrane damage caused by micro aggregates.

3.3. In vivo efficacy of micro aggregate-induced magnetic hyperthermia

To determine whether differences in aggregate size affects in vivo therapeutic efficacy as well, we evaluated the anticancer efficacy of micro and nano aggregates in mice bearing

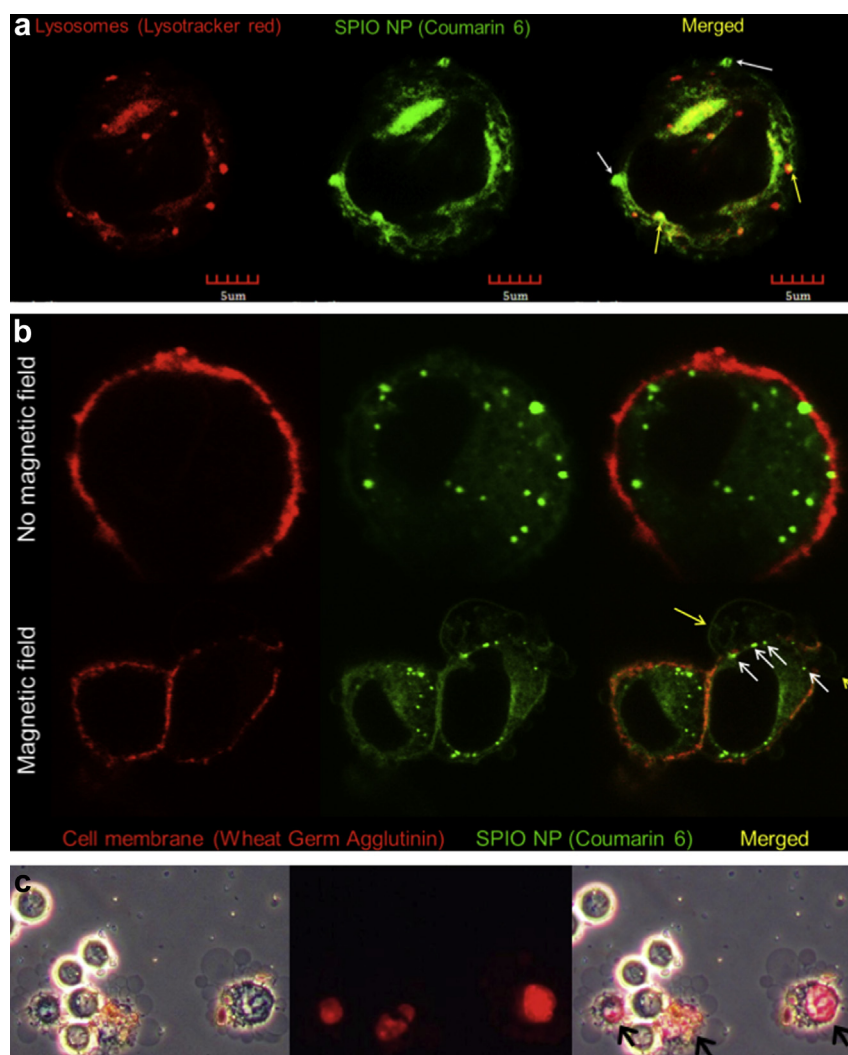


Fig. 4. Micro aggregate mediated membrane damage through direct contact. (a) Confocal microscopic images of cells incubated with coumarin-6 labeled SPIO micro aggregates (green). Lysosomes were stained with LysoTracker red[®]. Representative images showing the location of lysosomes (left), micro aggregates (center) and their colocalization (right) are shown. The merged image shows aggregates on the surface of cells (white arrows) and in lysosomes (yellow arrows). Scale bar, 5 μ m. (b) Confocal microscopy of cells incubated with coumarin-6 labeled SPIO micro aggregates before (top) and after (bottom) AMF exposure at low temperature (<5 $^{\circ}$ C). The cell membrane was labeled with Texas red[®] labeled wheat germ agglutinin (left). The coumarin-6 labeled SPIO micro aggregates (center) were present both on the cell membrane and inside the cells. The cell membrane was intact in cells incubated with particles in the absence of AMF (top right), indicated by the smooth cell membrane staining. Exposure to AMF resulted in cell membrane blebbing (bottom right, yellow arrows) at the sites where the aggregates contacted the cell membrane (white arrows). (c) Phase contrast (left) and fluorescence microscopic image (middle) of cells incubated with SPIO micro aggregates and PI and exposed to low temperature AMF. The merged image (right) shows PI positive, extensively blebbed cells (black arrows) and the healthy cells devoid of blebbing or PI staining. (For interpretation of the references to color in this figure legend, the reader is referred to the web version of this article.)

subcutaneous A549 tumor xenografts. Mice received either saline or 225 μg magnetite equivalent of nano or micro aggregate suspension by intra-tumoral injection. Animals receiving the aggregates without exposure to AMF served as control groups. Tumor temperatures were monitored using infrared thermometry, and the magnetic field conditions were optimized to ensure that the tumor temperature did not increase beyond 46 $^{\circ}\text{C}$. The average tumor temperature was 43.5 $^{\circ}\text{C}$ in both the micro and nano aggregate groups, and highest temperature did not exceed 45.7 $^{\circ}\text{C}$ (Fig. 5a). Nano aggregate-mediated MH resulted in a moderate decrease in tumor growth rate ($p = 0.085$) relative to that in animals that received nano aggregates but were not exposed to AMF. Micro aggregate-mediated MH showed near complete inhibition of tumor growth (Fig. 5b), which was statistically significant ($p < 0.001$). The results from the bioluminescence imaging reinforced this finding, with micro aggregate-mediated MH being highly effective in decreasing the tumor-associated luminescence (Fig. 5c). Histological analysis of the tumor sections revealed that micro aggregate-mediated MH resulted in the formation of “hollow” tumors, with a large central acellular core and a small outer rim of cells (Fig. 6a,

Supporting Information Figure S2). Immediately after exposure to AMF, cells surrounding the SPIO aggregates (confirmed by Prussian blue staining) were characterized by altered morphology, decreased cell volume, and increased nuclear density (Fig. 6c,e). Tumor tissue sections from the control group (injected with micro aggregates but not exposed to AMF) showed no such changes in the cellular morphology around the SPIO aggregates (Fig. 6b,d). Because all the experimental parameters (dose of SPIO, duration of AMF exposure and the temperature elevation) were similar for both nano and micro aggregates, the enhanced effectiveness of micro aggregates is likely due to local membrane damage.

It is noteworthy that despite their inhomogeneous distribution within the tumor, a complete inhibition of tumor growth was observed for micro aggregate treatment. A number of studies show that treatments that induce acute necrosis in the tumors are able to stimulate anti-tumor immune response, which reinforces the anticancer effectiveness of the treatment [42,43]. Thus, the acute cell damage and necrosis induced by micro aggregates could stimulate a bystander anti-tumor immune response, which would affect the growth of the entire tumor. The animal model used here

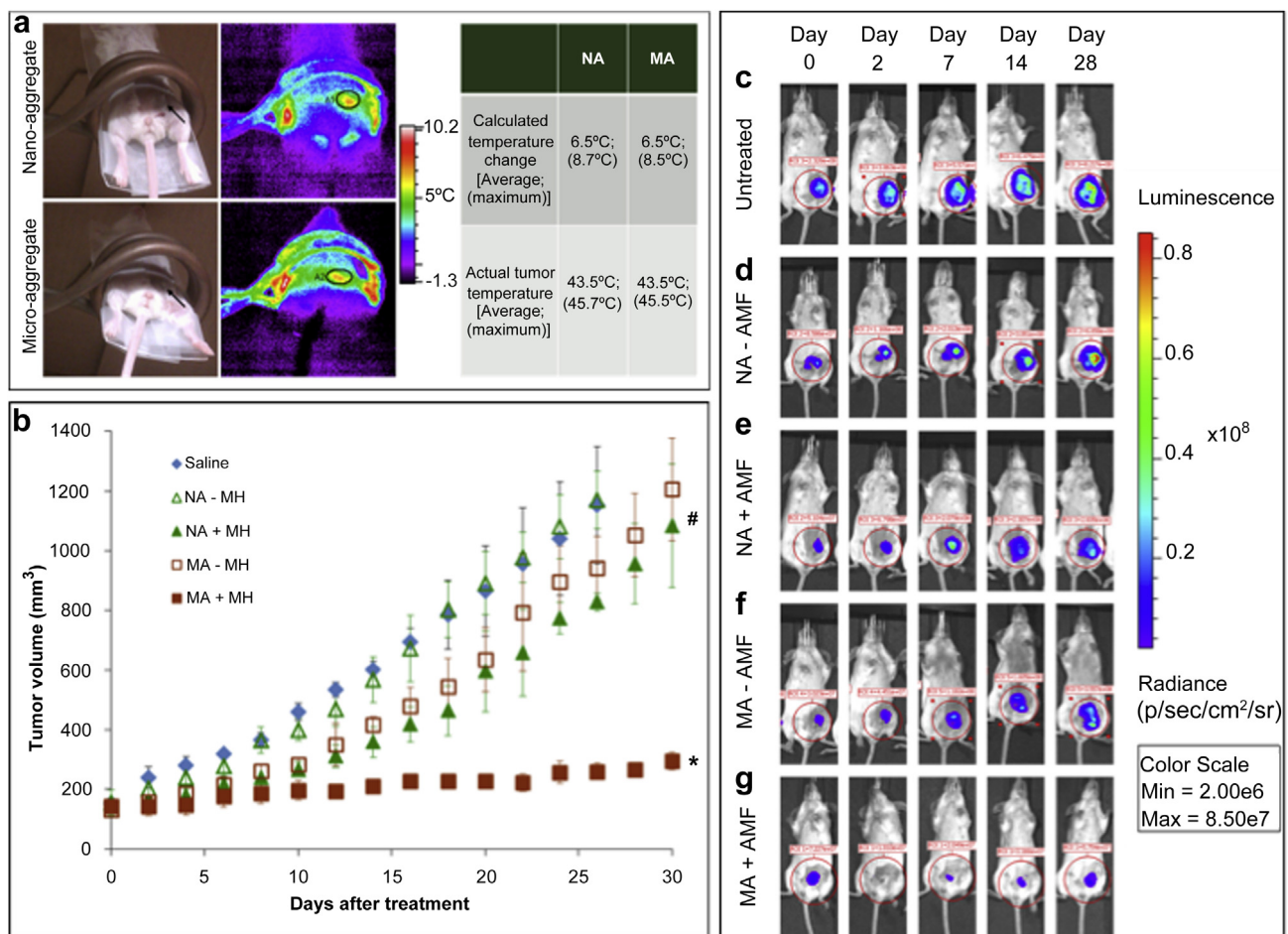


Fig. 5. Effect of SPIO aggregate mediated MH on *in vivo* tumor growth. (a) Representative photograph of a mouse placed in the radiofrequency coil (left) during nano aggregate (NA) (top) or micro aggregate (MA) (bottom) mediated MH. The black arrow indicates the location of the subcutaneous tumor xenograft. The temperature elevation during MH was measured using infrared thermometry. Infrared thermometric images of the temperature difference before and at the end of MH treatment is shown (right). The tumor temperature (black oval) was calculated for both nano and micro aggregate mediated MH (table). Note that the elevated temperature at the edges of the coil is due to the heating of the coil during AMF exposure. (b) The tumor growth was monitored every alternate day after MH treatment. The graph shows tumor growth with different treatments (225 μg magnetite equivalent for nano and micro aggregates) injected intratumorally as a function of time after treatment. Data shown is mean \pm S.D., $n = 6$. * $P < 0.001$ and # $P < 0.1$ vs. control. Representative bioluminescence images of mice bearing luciferase transfected A549 subcutaneous xenografts after different treatments are shown. Mice were injected with 40 μl (c) saline, (d, e) 225 μg magnetite equivalent of SPIO nano aggregates and (f, g) 225 μg magnetite equivalent of SPIO micro aggregates intratumorally when the tumor volumes reached 150 mm^3 . After 24 h, the (e) nano aggregate and (g) micro aggregate treated animals were subjected to magnetic hyperthermia for 30 min. Tumor bioluminescence was measured before MH treatment (Day 0) and on days 2, 7, 14, 21 and 28. The images are from an animal in each group monitored over 4 weeks after treatment. The bioluminescence intensity of all images was scaled as shown in the right.

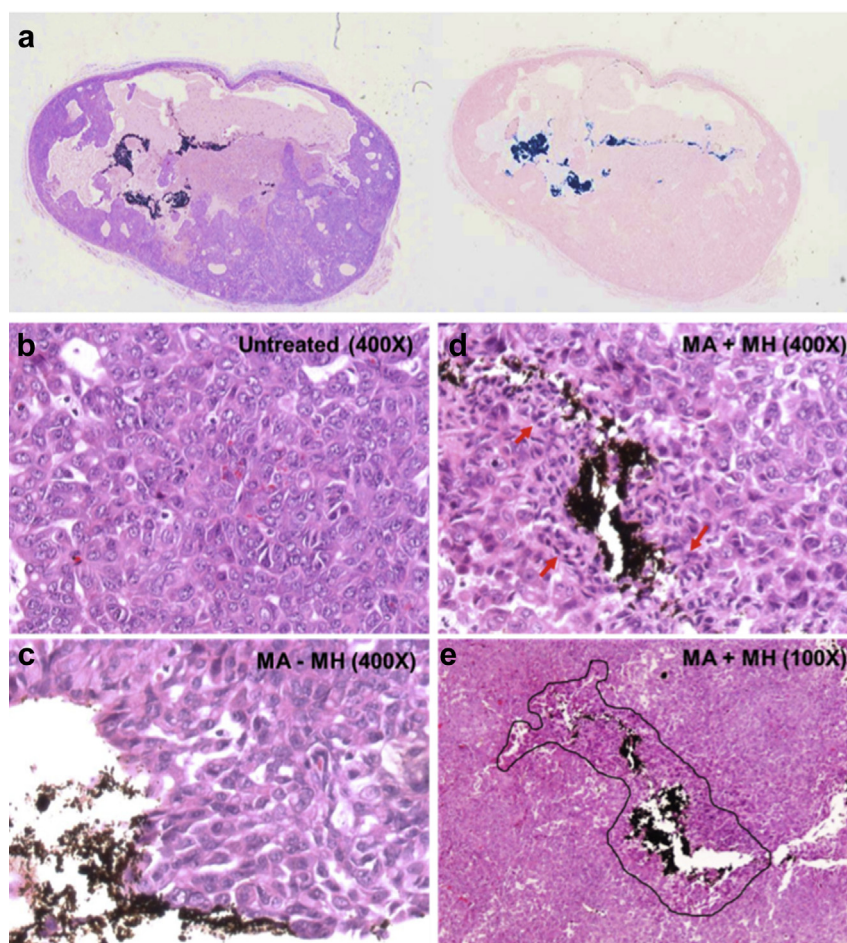


Fig. 6. Histology of tumors exposed to MH treatment. (a) Hematoxylin and eosin (H&E) staining (left) of a tumor after 30 days of micro aggregate mediated MH. The tumor is partially acellular due to the MH treatment. Prussian blue staining (right) performed on a subsequent section (5 μm apart) shows the presence of SPIO particles at the necrotic margins of the tumor. (b) H&E staining of a tumor section (400 \times magnification) from animals receiving no treatment. The tumor cells have a 'swollen' appearance with large lightly stained nucleus. (c) H&E staining (400 \times magnification) of a micro aggregate injected tumor that was not exposed to an AMF. The micro aggregates can be identified by their brown color. Cells adjacent to the particles have similar morphology as the untreated tumor (B). (d) H&E staining (400 \times magnification) of a tumor collected immediately after micro aggregate mediated MH. Cells around the particles have altered morphology characterized by cell shrinkage and denser nuclear stain. (e) Lower magnification (100 \times) of (D) showing a distinct region around the micro aggregates (black bordered area) where the cells have a different morphology compared to the rest of the tumor. (For interpretation of the references to color in this figure legend, the reader is referred to the web version of this article.)

(SCID mice) precludes the generation of humoral and T-cell mediated immune responses. However, these mice have functional natural killer (NK) cells that can mount an effective anticancer immune response [44]. In addition, an increase in local tumor temperature (hyperthermia) would likely reinforce the anticancer benefits of acute necrosis induced by micro aggregates. Induction of necrosis rather than apoptosis by micro aggregates may have additional benefits as well. Tumor cells can develop resistance to apoptotic pathways through upregulation of heat shock proteins [36,37]. Because necrotic cell death is often rapid (few minutes), necrosis is less prone to these resistance mechanisms. While an extensive investigation into induction of necrosis and generation of anticancer immune response by micro aggregates was beyond the scope of this report, these *in vivo* results confirm that larger aggregates are more effective in killing tumor cells than smaller sub-micron size aggregates.

Intravenous delivery of micro aggregates is likely not practical due to concerns of embolism [45,46] and because the particle size is too large to take advantage of the enhanced permeation and retention effect [3]. However, the particle size range of micro aggregates is particularly suitable for inhalation delivery [47,48] to treat lung tumors [48–50]. Also, several types of solid tumors

(liver, kidney, prostate, and lung) are treated clinically by local interventions using physical ablation techniques (microwave, radio-frequency) [51–53]. Such cancers will benefit from treatment with the micro aggregates. Alternately, an *in situ* aggregation approach can also be envisioned, where sub-micron size particles injected intravenously aggregate into micron size aggregates in the tumor microenvironment.

4. Conclusions

Inorganic nanoparticles have the propensity to aggregate when introduced into a biological milieu. Our studies showed that the particle size of aggregates affects the therapeutic performance of SPIO nanoparticles. Well-dispersed SPIO nanoparticles induce apoptosis, similar to that observed with conventional hyperthermia. Nanometer size aggregates, on the other hand, induce temperature-dependent autophagy through generation of ROS. Micron size aggregates caused rapid membrane damage and acute cell kill *in vitro*, which translated into effective *in vivo* tumor growth inhibition. Overall this work highlights the potential for developing highly effective anticancer therapeutics through simple yet often overlooked modifications of delivery systems such as their state of aggregation.

Acknowledgment

We thank the Flow Cytometry Core Facility of the Masonic Cancer Center, a comprehensive cancer center designated by the National Cancer Institute, supported in part by P30 CA77598. Parts of this work were carried out in the Characterization Facility, University of Minnesota, which receives partial support from NSF through the MRSEC program. We also thank the Comparative Pathology core facility for the preparation of H & E and Prussian blue stained slides.

We thank Dr. Robert S. Hafner (Characterization Facility, University of Minnesota) for help with TEM studies, Ying Jing (Electrical and Computer Engineering, University of Minnesota) for help with magnetization studies, Paula Overn (Comparative Pathology, University of Minnesota) for the preparation of histopathology slides and Brenda Koniar (Research Animal Resources, University of Minnesota) for assistance with animal studies.

Funding support from the Department of Defense (CA093453).

Appendix A. Supplementary data

Supplementary data related to this article can be found at <http://dx.doi.org/10.1016/j.biomaterials.2014.05.085>.

References

- [1] Matsumura Y, Maeda H. A new concept for macromolecular therapeutics in cancer chemotherapy: mechanism of tumorotropic accumulation of proteins and the antitumor agent smancs. *Cancer Res* 1986;46(12 Pt 1):6387–92.
- [2] Desai N, Trieu V, Yao Z, Louie L, Ci S, Yang A, et al. Increased antitumor activity, intratumor paclitaxel concentrations, and endothelial cell transport of cremophor-free, albumin-bound paclitaxel, ABI-007, compared with cremophor-based paclitaxel. *Clin Cancer Res* 2006;12(4):1317–24.
- [3] Singh S, Sharma A, Robertson GP. Realizing the clinical potential of cancer nanotechnology by minimizing toxicologic and targeted delivery concerns. *Cancer Res* 2012;72(22):5663–8.
- [4] Perrault SD, Walkey C, Jennings T, Fischer HC, Chan WC. Mediating tumor targeting efficiency of nanoparticles through design. *Nano Lett* 2009;9(5):1909–15.
- [5] Kong G, Braun RD, Dewhirst MW. Hyperthermia enables tumor-specific nanoparticle delivery: effect of particle size. *Cancer Res* 2000;60(16):4440–5.
- [6] Qian X, Peng XH, Ansari DO, Yin-Goen Q, Chen GZ, Shin DM, et al. In vivo tumor targeting and spectroscopic detection with surface-enhanced Raman nanoparticle tags. *Nat Biotechnol* 2008;26(1):83–90.
- [7] Lee H, Lee E, Kim do K, Jang NK, Jeong YY, Jon S. Antibiofouling polymer-coated superparamagnetic iron oxide nanoparticles as potential magnetic resonance contrast agents for in vivo cancer imaging. *J Am Chem Soc* 2006;128(22):7383–9.
- [8] Peng XH, Qian X, Mao H, Wang AY, Chen ZG, Nie S, et al. Targeted magnetic iron oxide nanoparticles for tumor imaging and therapy. *Int J Nanomed* 2008;3(3):311–21.
- [9] Diaz B, Sanchez-Espinel C, Arruebo M, Faro J, de Miguel E, Magadan S, et al. Assessing methods for blood cell cytotoxic responses to inorganic nanoparticles and nanoparticle aggregates. *Small* 2008;4(11):2025–34.
- [10] van Landeghem FK, Maier-Hauff K, Jordan A, Hoffmann KT, Gneveckow U, Scholz R, et al. Post-mortem studies in glioblastoma patients treated with thermotherapy using magnetic nanoparticles. *Biomaterials* 2009;30(1):52–7.
- [11] Safi M, Sarrouj H, Sandre O, Mignet N, Berret JF. Interactions between sub-10-nm iron and cerium oxide nanoparticles and 3T3 fibroblasts: the role of the coating and aggregation state. *Nanotechnology* 2010;21(14):145103.
- [12] Lundqvist M, Stigler J, Elia G, Lynch I, Cedervall T, Dawson KA. Nanoparticle size and surface properties determine the protein corona with possible implications for biological impacts. *Proc Natl Acad Sci U S A* 2008;105(38):14265–70.
- [13] Hiergeist R, Andrä W, Buske N, Hergt R, Hilger I, Richter U, et al. Application of magnetite ferrofluids for hyperthermia. *J Magn Magn Mater* 1999;201(1–3):420–2.
- [14] Jordan A, Scholz R, Wust P, Fähling H, Roland F. Magnetic fluid hyperthermia (MFH): cancer treatment with AC magnetic field induced excitation of biocompatible superparamagnetic nanoparticles. *J Magn Magn Mater* 1999;201(1–3):413–9.
- [15] Hergt R, Andrä W, d'Ambly CG, Hilger I, Kaiser WA, Richter U, et al. Physical limits of hyperthermia using magnetite fine particles. *IEEE Trans Magn* 1998;34(5):3745–54.
- [16] Rosensweig RE. Heating magnetic fluid with alternating magnetic field. *J Magn Magn Mater* 2002;252(0):370–4.
- [17] Tasci TO, Vargel I, Arat A, Guzel E, Korkusuz P, Atalar E. Focused RF hyperthermia using magnetic fluids. *Med Phys* 2009;36(5):1906–12.
- [18] Tseng HY, Lee GB, Lee CY, Shih YH, Lin XZ. Localised heating of tumours utilising injectable magnetic nanoparticles for hyperthermia cancer therapy. *IET Nanobiotechnol* 2009;3(2):46–54.
- [19] Foy SP, Manthe RL, Foy ST, Dimitrijevic S, Krishnamurthy N, Labhasetwar V. Optical imaging and magnetic field targeting of magnetic nanoparticles in tumors. *ACS Nano* 2010;4(9):5217–24.
- [20] Krishna Murti GSR, Moharir AV, Sarma VAK. Spectrophotometric determination of iron with orthophenanthroline. *Microchem J* 1970;15(4):585–9.
- [21] Giustini AJ, Ivkov R, Hoopes PJ. Magnetic nanoparticle biodistribution following intratumoral administration. *Nanotechnology* 2011;22(34):345101.
- [22] Luchetti F, Canonico B, Della Felice M, Burattini S, Battistelli M, Papa S, et al. Hyperthermia triggers apoptosis and affects cell adhesiveness in human neuroblastoma cells. *Histol Histopathol* 2003;18(4):1041–52.
- [23] Rodriguez-Luccioni HL, Latorre-Esteves M, Mendez-Vega J, Soto O, Rodriguez AR, Rinaldi C, et al. Enhanced reduction in cell viability by hyperthermia induced by magnetic nanoparticles. *Int J Nanomed* 2011;6:373–80.
- [24] Takasu T, Lyons JC, Park HJ, Song CW. Apoptosis and perturbation of cell cycle progression in an acidic environment after hyperthermia. *Cancer Res* 1998;58(12):2504–8.
- [25] Lazebnik YA, Kaufmann SH, Desnoyers S, Poirier GG, Earnshaw WC. Cleavage of poly(ADP-ribose) polymerase by a proteinase with properties like ICE. *Nature* 1994;371(6495):346–7.
- [26] Uchiyama Y. Autophagic cell death and its execution by lysosomal cathepsins. *Arch Histol Cytol* 2001;64(3):233–46.
- [27] Chaitanya GV, Steven AJ, Babu PP. PARP-1 cleavage fragments: signatures of cell-death proteases in neurodegeneration. *Cell Commun Signal* 2010;8:31.
- [28] Kabeya Y, Mizushima N, Ueno T, Yamamoto A, Kirisako T, Noda T, et al. LC3, a mammalian homologue of yeast Apg8p, is localized in autophagosome membranes after processing. *EMBO J* 2000;19(21):5720–8.
- [29] Tsujimoto Y, Shimizu S. Another way to die: autophagic programmed cell death. *Cell Death Differ* 2005;12(Suppl. 2):1528–34.
- [30] Zhang H, Kong X, Kang J, Su J, Li Y, Zhong J, et al. Oxidative stress induces parallel autophagy and mitochondria dysfunction in human glioma U251 cells. *Toxicol Sci* 2009;110(2):376–88.
- [31] Chen Y, McMillan-Ward E, Kong J, Israels SJ, Gibson SB. Oxidative stress induces autophagic cell death independent of apoptosis in transformed and cancer cells. *Cell Death Differ* 2008;15(1):171–82.
- [32] Cerella C, D'Alessio M, Cristofanon S, De Nicola M, Radogna F, Dicato M, et al. Subapoptogenic oxidative stress strongly increases the activity of the glycolytic key enzyme glyceraldehyde 3-phosphate dehydrogenase. *Ann N Y Acad Sci* 2009;1171:583–90.
- [33] Colell A, Ricci JE, Tait S, Milasta S, Maurer U, Bouchier-Hayes L, et al. GAPDH and autophagy preserve survival after apoptotic cytochrome c release in the absence of caspase activation. *Cell* 2007;129(5):983–97.
- [34] Proskuryakov SY, Konoplyannikov AG, Gabai VL. Necrosis: a specific form of programmed cell death? *Exp Cell Res* 2003;283(1):1–16.
- [35] Liu D, Wang L, Wang Z, Cuschieri A. Magnetoporation and magnetolysis of cancer cells via carbon nanotubes induced by rotating magnetic fields. *Nano Lett* 2012;12(10):5117–21.
- [36] Frossard JL. Heat shock protein 70 (HSP70) prolongs survival in rats exposed to hyperthermia. *Eur J Clin Invest* 1999;29(6):561–2.
- [37] Ito A, Shinkai M, Honda H, Yoshikawa K, Saga S, Wakabayashi T, et al. Heat shock protein 70 expression induces antitumor immunity during intracellular hyperthermia using magnetite nanoparticles. *Cancer Immunol Immunother* 2003;52(2):80–8.
- [38] Patil Y, Sadhukha T, Ma L, Panyam J. Nanoparticle-mediated simultaneous and targeted delivery of paclitaxel and tariquidar overcomes tumor drug resistance. *J Control Release* 2009;136(1):21–9.
- [39] Barros LF, Kanaseki T, Sabirov R, Morishima S, Castro J, Bittner CX, et al. Apoptotic and necrotic blebs in epithelial cells display similar neck diameters but different kinase dependency. *Cell Death Differ* 2003;10(6):687–97.
- [40] Huang H, Delikanli S, Zeng H, Ferkey DM, Pralle A. Remote control of ion channels and neurons through magnetic-field heating of nanoparticles. *Nat Nanotechnol* 2010;5(8):602–6.
- [41] Polo-Corralles L, Rinaldi C. Monitoring iron oxide nanoparticle surface temperature in an alternating magnetic field using thermoresponsive fluorescent polymers. *J Appl Phys* 2012;111(7):07B334. 3.
- [42] Gravante G, Sconocchia C, Ong SL, Dennison AR, Lloyd DM. Immunoregulatory effects of liver ablation therapies for the treatment of primary and metastatic liver malignancies. *Liver Int* 2009;29(1):18–24.
- [43] Mroz P, Hashmi JT, Huang Y-Y, Lange N, Hamblin MR. Stimulation of anti-tumor immunity by photodynamic therapy. *Exp Rev Clin Immunol* 2010;7(1):75–91.
- [44] Takehara T, Uemura A, Tatsumi T, Suzuki T, Kimura R, Shiotani A, et al. Natural killer cell-mediated ablation of metastatic liver tumors by hydrodynamic injection of IFN γ gene to mice. *Int J Cancer* 2007;120(6):1252–60.
- [45] Carrstensen H, Muller RH, Muller BW. Particle size, surface hydrophobicity and interaction with serum of parenteral fat emulsions and model drug carriers as parameters related to RES uptake. *Clin Nutr* 1992;11(5):289–97.
- [46] Mansour HM, Rhee YS, Wu X. Nanomedicine in pulmonary delivery. *Int J Nanomed* 2009;4:299–319.
- [47] Patton JS, Byron PR. Inhaling medicines: delivering drugs to the body through the lungs. *Nat Rev Drug Discov* 2007;6(1):67–74.
- [48] Lennon FE, Mirzapourzadeh T, Mambetsariev B, Sargia R, Moss J, Singleton PA. Overexpression of the mu-opioid receptor in human non-small cell lung

- cancer promotes Akt and mTOR activation, tumor growth, and metastasis. *Anesthesiology* 2012;116(4):857–67.
- [49] Zarogoulidis P, Chatzaki E, Porpodis K, Domvri K, Hohenforst-Schmidt W, Goldberg EP, et al. Inhaled chemotherapy in lung cancer: future concept of nanomedicine. *Int J Nanomed* 2012;7:1551–72.
- [50] Yi D, Wiedmann TS. Inhalation adjuvant therapy for lung cancer. *J Aerosol Med Pulm Drug Deliv* 2010;23(4):181–7.
- [51] Bomers JGR, Sedelaar JPM, Barentsz JO, Fütterer JJ. MRI-guided interventions for the treatment of prostate cancer. *Am J Roentgenol* 2012;199(4):714–20.
- [52] Cornelis F, Balageas P, Le Bras Y, Rigou G, Boutault JR, Bouzgarrou M, et al. Radiologically-guided thermal ablation of renal tumours. *Diagn Interv Radiol* 2012;93(4):246–61.
- [53] Sharma A, Abtin F, Shepard J-AO. Image-guided ablative therapies for lung cancer. *Radiol Clin North Am* 2012;50(5):975–99.